TL.2.1993-279
C.2

RESERVOIR CHARACTERIZATION CASE STUDY: THE PROVOST UPPER MANNVILLE B POOL

J.W. KRAMERS
S. BACHU
D.L. CUTHIELL
L-P. YUAN

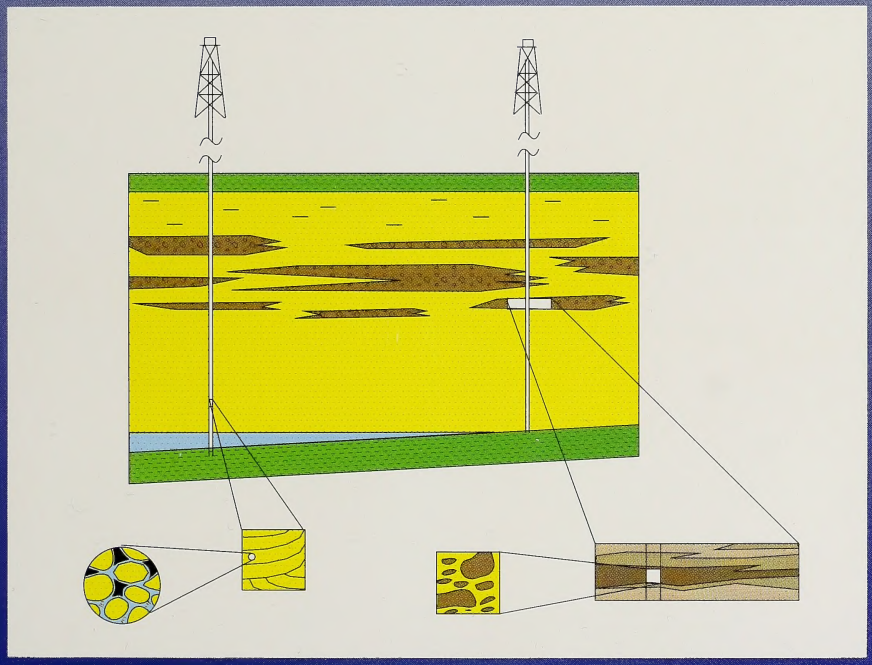

ALBERTA RESEARCH COUNCIL
Alberta Geological Survey
Alberta ENERGY
Alberta OIL SANDS TECHNOLOGY AND RESEARCH AUTHORITY

CANADIANA
JUL 27 1993

RESERVOIR CHARACTERIZATION CASE STUDY: THE PROVOST UPPER MANNVILLE B POOL

J.W. Kramers
S. Bachu
D.L. Cuthiell
L-P. Yuan

Alberta Geological Survey
Alberta Research Council
P.O. Box 8330
Edmonton, Alberta, Canada
T6H 5X2

June 1993

RESERVOIR CHARACTERIZATION CASE STUDY: THE PROVOST UPPER MANNVILLE B POOL

Copyright 1993 by AOSTRA. All rights reserved. Printed in Canada. No part of this publication may be reproduced, stored in a retrieval system, or transmitted, in any form or by any means, electronic, mechanical, photocopying, recording, or otherwise, without the prior permission of the publisher.

ISBN 0-7732-1236-1

PUBLISHED BY

ALBERTA OIL SANDS TECHNOLOGY AND RESEARCH AUTHORITY
500 HIGHFIELD PLACE
10010 – 106 STREET
EDMONTON, ALBERTA, CANADA
T5J 3L8

PUBLISHER'S NOTE

AOSTRA encourages and supports geology research programs and is pleased to publish this case study entitled *Reservoir Characterization Case Study: The Provost Upper Mannville B Pool.* This publication is designed to make available, research results, analytical procedures, and engineering data on the properties and behaviour of Alberta petroleum resources that may otherwise not be available to the public.

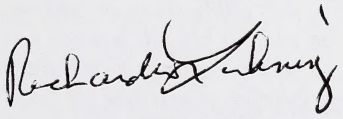

R.W. Luhning
Vice Chairman and Executive Director
Alberta Oil Sands Technology and Research Authority
Edmonton, Alberta, Canada

June 1993

The Alberta Oil Sands Technology and Research Authority (AOSTRA) makes no warranty, express or implied, nor assumes any legal liability or responsibility for the accuracy, completeness, or usefulness of any information, apparatus, product, or process disclosed in this publication, or represents that its use would not infringe on privately owned rights. Reference herein to any specific commercial product, process, or service by trade name, trademark, manufacturer, or otherwise, does not necessarily constitute or imply its endorsement, recommendation, or favoring by AOSTRA. The views and opinions of authors expressed herein do not necessarily reflect those of AOSTRA.

EXECUTIVE SUMMARY

A comprehensive approach to reservoir characterization was developed using an integrated, interdisciplinary study involving geology, pore system analysis, and parameter modelling. The Provost Upper Mannville B Pool in east-central Alberta was used as a case study. The approach is a sequential one, starting with a detailed understanding of the reservoir geology and pore systems, and scaling up conventional core analysis permeability and porosity data to the flow unit or reservoir grid block scale. Different methodologies were adopted for each flow unit, depending on its internal characteristics.

For the "relatively uniform" sandy portions of the reservoir, conventional statistical scaling up techniques were adopted. The geometric average was used to scale up horizontal permeability values to the flow unit scale for those flow units where there is no trend in reservoir properties. The arithmetic average of core plug values was used to characterize horizontal permeability for interbedded sands and shales. Where flow units have a variation of permeability values with depth, the average of the trend is used to define the characteristic value. Vertical permeability values were assessed using a k_v/k_h anisotropy relation for each flow unit. Porosity was scaled up using a weighted average of individual measurements for each sandy flow unit.

For the heterogeneous shale clast flow unit, the scaling up of permeability values was carried out by means of numerical flow simulations. General curves were developed that relate shale clast content and aspect ratio of the clasts to effective permeability. These curves, together with empirical results from larger scale modelling, can be used to derive characteristic values for shale clast layers or zones, based on an estimate of the shale clast content and aspect ratio from core. These results can be extended to other sand shale systems, such as shale lenses or beds in a sandstone reservoir.

The combination of these approaches has provided a comprehensive methodology for a quantitative characterization of siliciclastic reservoir flow units at every well in the reservoir. The resulting values can be used as input for numerical simulation of recovery processes. For multiwell simulations, interwell variability prediction techniques should also be used to assign values to the non-well simulator grid blocks.

This project was sponsored by the Alberta Oil Sands Technology and Research Authority (AOSTRA), the Alberta Research Council, and the Alberta Department of Energy.

Digitized by the Internet Archive
in 2015

https://archive.org/details/reservoircharact00kram

TABLE OF CONTENTS

PUBLISHER'S NOTE v
EXECUTIVE SUMMARY vii
TABLE OF CONTENTS ix
LIST OF FIGURES xi
LIST OF TABLES xvii
INTRODUCTION 1
APPROACH TO RESERVOIR CHARACTERIZATION 3
RESERVOIR GEOLOGY 5
Lithofacies 5
Blocky channel lithofacies 5
Transition zone lithofacies 9
Shale clast lithofacies 9
Channel margin lithofacies 11
Overbank lithofacies 13
Abandonment lithofacies 13
Depositional Environments 13
Mineralogy 14
THE RESERVOIR 17
RESERVOIR SUBDIVISION 23
PORE SCALE CHARACTERIZATION 25
Image Analysis Methods 25
Previous methods 25
Generalized size analysis method 25
Connectivity indicator 26
Reservoir Pore Systems 27
Sampling and sample preparation 27
Permeability and pore geometry 30
Pore type and lithofacies 30
Capillarity and pore type 34
Pore Scale Characterization Discussion 35

SANDY FACIES CHARACTERIZATION 37
Scaling up from Core to Flow Unit 37
Scaling up to the Reservoir Scale 40
Permeability Anisotropy 45
HETEROGENEOUS FACIES CHARACTERIZATION 47
Geometry and Architecture of Shale Clast Zones 48
Core scale characteristics 49
Large scale characteristics 54
Generating Synthetic Core Scale Distributions of Clasts 55
Estimating Core Scale Permeability 58
Core scale numerical flow simulations 59
Physical analogue measurements of effective permeability 61
Results and discussions 62
Scaling Permeability Values up to the Reservoir Grid Block Scale 70
Simulating large scale spatial characteristics of shale clast zones 71
Numerical flow simulation methodology 71
Permeability of a small reservoir grid block 73
Permeability of a large reservoir grid block 74
Sample grid block calculations 75
Generalizations to Other Types of Heterogeneity 76
Effect of aspect ratio 77
Effect of shale permeability 79
Effect of clast shape 79
Effect of clast size distribution 79
Core Scale Effective Parameters in Transient Fluid Flow 80
QUANTITATIVE CHARACTERIZATION OF THE RESERVOIR 85
SUMMARY AND CONCLUSIONS 87
ACKNOWLEDGEMENTS 89
REFERENCES 91
APPENDIX A — Generalized Size Analysis Algorithm for Pore System Analysis 95
APPENDIX B — Stereology and Clast Generation Software 109
APPENDIX C — Finite Difference Flow Simulation Method 123

LIST OF FIGURES

Figure 1. Location map of the Provost Upper Mannville B Pool. 1

Figure 2. Lower Cretaceous stratigraphy in east-central and northeastern Alberta. 2

Figure 3. Flow chart of the reservoir characterization process used in this study. 4

Figure 4. Isopach, McLaren Formation valley fill sequence. 6

Figure 5. West-to-east stratigraphic cross section through the Provost Upper Mannville B Pool showing the valley-shaped geometry for the valley fill sediments. 7

Figure 6. Typical well log from the Provost Upper Mannville B Pool showing four of the five lithofacies of the McLaren valley fill sequence. 8

Figure 7. Core photograph of the blocky channel lithofacies (14-29-37-1W4, 742.5-752.2 m depth KB). 9

Figure 8. Core photographs of the transition zone, channel margin and overbank lithofacies (14B-17-37-1W4, 724.8-736.7 m depth KB). 10

Figure 9. Core photograph of the shale clast lithofacies (5A-20-37-1W4, 731.3-737.0 m depth KB). 11

Figure 10. Isopach, shale clast zones net thickness. 12

Figure 11. Core photograph of the abandonment lithofacies (10D-17-37-1W4, 727.5-739.2 m depth KB). 14

Figure 12. Regional extent of the McLaren valley system in east central Alberta. 15

Figure 13. Grain mineralogy of McLaren Formation valley fill sands in comparison with Colony and Waseca Formation sands. 16

Figure 14. Isopach, gross reservoir sand thickness. 18

Figure 15. Isopach, net oil pay. 19

Figure 16. North-to-south structural cross section through the Provost Upper Mannville B Pool. 20

Figure 17. Isopach, water leg underlying the oil column. 21

Figure 18. Scales of characterization for the Provost Upper Mannville B Pool. 23

Figure 19. Example of an opening operation with a disk of radius *r*. 26

Figure 20. Example of three opening operations with increasing structuring elements to differentiate pore areas with different size. 26

Figure 21. Diagram of opening processes to remove the rough (pore wall roughness) and smooth components of a porel (modified from Ehrlich et al., 1984). 27

Figure 22. Graphical representation of the connectivity indicator. 27

Figure 23. Petrographic image analysis of representative end member pore images with their rough and smooth size distributions. 28

Figure 24. Regression surfaces between permeability, pore size and connectivity indicator. .. 31

Figure 25. Quaternary plot of sample compositions and their lithofacies origin. 32

Figure 26. Reservoir lithofacies and their characteristic pore end members. 33

Figure 27. Capillary pressure and residual saturation analysis results for three selected samples representing three pore types in the reservoir. 34

Figure 28. Permeability trends for wells from the steam pilot in the Provost Upper Mannville B Pool. 38

Figure 29. Sandy facies flow units and their characteristic horizontal permeability and porosity values for a composite example well. 39

Figure 30. Areal distribution (a) and cumulative probability plot (b) for transmissivity in the oil saturated blocky channel sand flow unit. 44

Figure 31. Areal distribution (a) and cumulative probability plot (b) for porosity in the oil saturated blocky channel sand flow unit. 44

Figure 32. Histogram for k_v/k_h anisotropy values (a) and scatter plot of k_v versus k_h (b) for samples from the oil saturated blocky channel sand flow unit. 46

Figure 33. Scatter plots of k_v versus k_h for the transition zone sand flow unit (a) and the channel margin sand flow unit (b). 46

Figure 34. Digitized version of a typical shale clast layer. 49

Figure 35. Stratigraphic cross section through four closely spaced wells with core control showing the geometry of a shale clast zone. 50

Figure 36. Geometric parameters characterizing a shale clast. 51

Figure 37. Frequency distributions for clast parameters in wells A, B, C. 52

Figure 38. Semi-variograms for vertical and horizontal lags for a sample of digitized clast data set. 53

Figure 39. Distribution of shale clast fraction with depth for well B. 54

Figure 40. Shale fraction distribution within layers in well B based on observed fractions from all layers. 55

Figure 41. Shale clast intervals from well B used as the basis of stereological calculations. 56

Figure 42. Frequency distributions for length (a) and aspect ratio (b) based on all clasts from the intervals shown in Figure 41. 57

Figure 43. Comparison of length distribution of clasts from 2D sections of a 3D simulated clast interval with the distribution for real shale clasts shown in Figure 42a. 57

Figure 44. Comparison of aspect ratio distribution of clasts from 2D sections of a 3D simulated clast interval with the distribution for real shale clasts shown in Figure 42b. 58

Figure 45. Semi-variograms for vertical and horizontal lags for a 2D section of a simulated 3D clast interval. 58

Figure 46. Flow chart for numerical permeability calculations. 59

Figure 47. The concept of a numerical permeameter: (a) heterogeneous sample; (b) equivalent homogeneous sample. 60

Figure 48. Permeameter used in physical flow experiments. 63

Figure 49. Slabs from one of the physical analogue blocks. 64

Figure 50. Vertical section near the middle of each of eight simulated 3D clast intervals. 65

Figure 51. Horizontal and vertical permeability computed for 3D simulated clast intervals. 66

Figure 52. Comparison of 3D simulation results for clasts with standard arithmetic, geometric, and harmonic mean predictions. 66

Figure 53. Comparison of results from 3D numerical simulations with results from physical analogue experiments. 66

Figure 54. Core scale intervals for which flow simulations were performed. 68

Figure 55. Effective permeability of 2D clasts computed for the intervals shown in Figure 54. 69

Figure 56. Comparison of simulation results for real 2D clast sections with results for cross sections of simulated 3D clast sections. 69

Figure 57. Comparison of simulation results for real 2D clast sections with results for cross sections of physical analogue pebble blocks. 70

Figure 58. Comparison of effective permeability computed for 3D simulated clast cases with permeability for 2D sections of the 3D cases. 70

Figure 59. Examples of cross sections from simulated clast layer distributions containing Type 1 and Type 2 layers. 72

Figure 60. Comparison of effective permeability for clasts having a realistic aspect ratio distribution (baseline) with effective permeability for clasts all having the same aspect ratio. 77

Figure 61. Effective permeability for clast distributions having different aspect ratios. 78

Figure 62. Comparison of results for aspect ratio 0.1 with those of Deutsch (1989). 79

Figure 63. Dependence of effective permeability on ratio of shale to sand permeability for a simulated 3D interval. 79

Figure 64. Comparison of effective permeability for ellipsoidal clasts and parallelopipedal shales having the same distributions of size and aspect ratio as real shale clasts 80

Figure 65. Effective permeability of simulated clast intervals having a realistic distribution of clast sizes and having a single size. 80

Figure 66. Comparison of effective permeability for clasts having realistic distributions of size and aspect ratio with clasts that all have the same size and aspect ratio. 80

Figure 67. Variation in time of the input and output flows through the core region with $f = 0.351$ shale clasts, for homogeneous porosity and compressibility. 82

Figure 68. Variation in time of the input and output flows through the core region with $f = 0.351$ shale clasts, for homogeneous permeability. 83

Figure 69. Variation in time of the input and output flows through the core region with $f = 0.351$ shale clasts, for homogeneous permeability and heterogeneous porosity and compressibility. 83

Figure 70. Comparison of the input and output flows through the core region with $f = 0.351$ shale clasts. 84

Figure 71. Relative error in computed flow rates during transient flow. 84

Figure 72. Effective values for permeability and porosity for all reservoir flow units in the composite example well. 85

Figure A1. Erosion-dilation image processing algorithm. 96

Figure A2. Disks of radius three for (a) four-neighbor and (b) eight-neighbor distance functions. 96

Figure A3. Disks of radius six for (a) one (four-neighbor) to one (eight-neighbor) mixing distance function and (b) two (four-neighbor) to one (eight-neighbor) mixing distance functions. 97

Figure A4. Example of a binary pore image (a), its gray level distance map image (b), binary skeleton map image (c), gray level size map image (d), and the intensity histogram (e) of the size map, i.e., the pore size distribution. 98

Figure A5. Examples of pore images with different pore sizes and grain sizes. 99

Figure B1. Plan view of an ellipsoid with major axis length D intersected by two sectioning planes AA' and BB'. 109

Figure C1. Portion of a 2D finite difference grid and the control volume (dashed box) used to derive the equation for pressure at node (i, j). 123

LIST OF TABLES

Table 1. Pore system analysis results. 29

Table 2. Well by well characteristic values for horizontal permeability (k_h), porosity (ϕ), hydraulic conductivity (K), and transmissivity (T) for the sandy flow units in the northern portion of the Provost Upper Mannville B Pool. 41

Table 3. Reservoir scale characteristic values of porosity and transmissivity for the sandy flow units in the northern portion of the Provost Upper Mannville B Pool. 45

Table 4. Means and standard deviations of the clast characteristic distributions shown in Figure 37. 51

Table 5. FD simulation performance for different grid sizes having shale clast fraction 0.351, illustrated in Figure 54. 61

Table 6. Effective permeabilities calculated using the FD method for simulated 3D clast intervals. 64

Table 7. Effective permeabilities calculated using the FD method for the clast intervals shown in Figure 54. 69

Table 8. Estimates of vertical permeability of a synthetic layer. 73

Table 9. Estimates of horizontal permeability of a synthetic layer. 74

Table 10. Computed vertical permeability of simulated large grid blocks and averages estimated from vertical "wells" through the blocks. 75

Table 11. Computed horizontal permeability of simulated large grid blocks and averages estimated from vertical "wells" through the blocks. 76

Table 12. Generalized weighted mean exponents for different aspect ratios computed using a 3D numerical model. 78

INTRODUCTION

The successful exploitation of a hydrocarbon reservoir depends on its accurate characterization and the implementation of a recovery strategy suitable to the reservoir and its contained fluids. The majority of the oil sands and heavy oil reservoirs of Western Canada, with resources of 471.6×10^9 m^3 bitumen (Outtrim and Evans, 1978; MacCallum and McCrossan, 1979; Wilson and Bennet, 1985), have to be recovered by in-situ methods. A multidisciplinary team is needed to characterize these complex and heterogeneous reservoirs and to develop processes for the successful recovery of these resources. With this in mind, the Alberta Geological Survey initiated a project, through its Joint Oil Sands Geology Program with the Alberta Oil Sands Technology and Research Authority (AOSTRA) and the Alberta Department of Energy, with the objective to develop and evaluate techniques for the characterization of oil sands and heavy oil reservoirs, for use in numerical reservoir simulations.

This report presents the results of studies carried out using the Provost Upper Mannville B heavy oil pool as a case study. The relatively uniform sandy portions of this reservoir have been characterized from the pore scale to the reservoir flow unit scale using a variety of techniques. Characterization of the heterogeneous portions of the reservoir was carried out using numerical modelling of fluid flow through domains based on actual core-sized regions, and scaling up these results to the flow unit scale. The combination of these approaches in one multidisciplinary project has provided a comprehensive quantitative characterization of the reservoir flow units, suitable for reservoir simulation studies. This approach is applicable to a wide variety of clastic reservoirs.

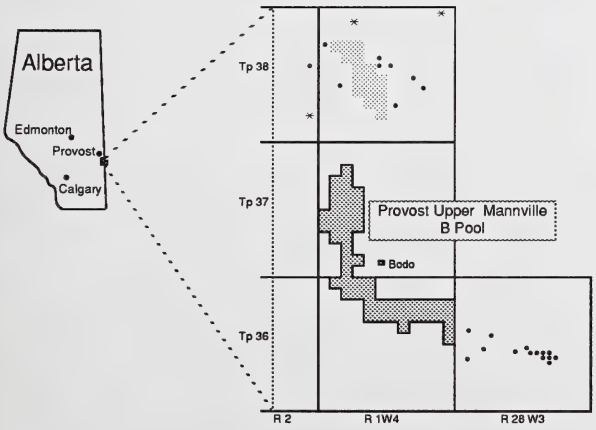

Figure 1. *Location map of the Provost Upper Mannville B Pool (dots represent well locations).*

The Provost Upper Mannville B Pool was chosen as a case study reservoir because of the pool's limited stratigraphic and areal extent, good data control (logs and core), and a variety of reservoir conditions (e.g., bottom water, gas cap, and permeability barriers). In addition, data on its reservoir properties are available in the public domain through a series of Petroleum Recovery Institute reports (Collins, 1977; Collins and Pilles, 1981; Hayashitani and Davis, 1981), and papers by Nazarko (1983), and Salahub and Mudie (1990).

The Provost Upper Mannville B Pool reservoir is located in east-central Alberta near the Alberta–Saskatchewan border (Figure 1). It is located in the northern half of Twp. 36 and in the western half of Twp. 37, Rge. 1W4. The reservoir is found in McLaren Formation sands of Upper Mannville (Lower Cretaceous, Lower Albian) age (Figure 2), at a depth of approximately 725 m KB. It occurs in channel sands and contains heterogeneities, such as shale clast zones, which are found in many other Alberta channel deposits. The reservoir has a long and narrow trend, approximately 1.5-km wide by 15-km long (Figure 1), with a thickness up to 35 m and an average net pay of 10–12 m. The reservoir is underlain by shales and silts of the Waseca Formation and capped by McLaren Formation shales and the overlying Colony Formation.

The Alberta Energy Resources Conservation Board has estimated the original oil in place at 34,200,000 m^3 of 13°API oil. Primary production is in the 5% range, with initial production up to 10 m^3/day with a low water cut (Nazarko, 1983). Several EOR

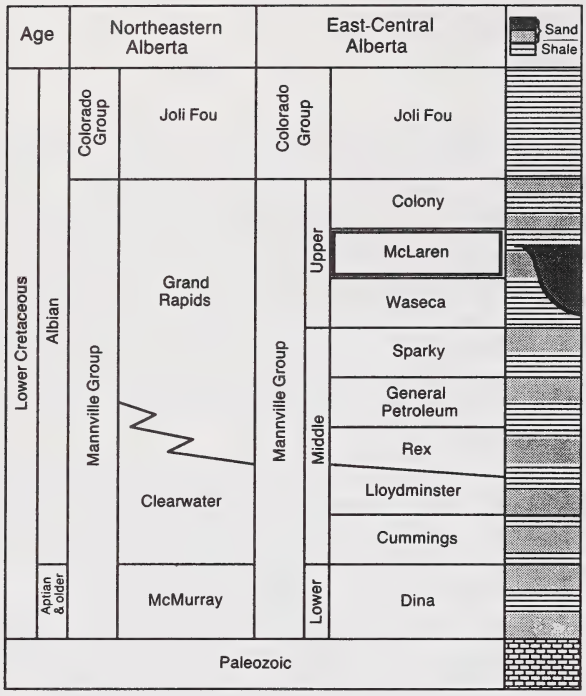

Figure 2. *Lower Cretaceous stratigraphy in east-central and northeastern Alberta.*

projects are or have been active in the pool. Nazarko (1983) mentions two single well steam projects and describes a combustion pilot composed of seven six-hectare seven-spots in Sec. 17, Twp. 37, Rge 1W4. Currently, a steam pilot is being operated by Norcen Energy Resources Ltd. in Sec. 20, Twp. 37, Rge. 1W4 (Salahub and Mudie, 1990).

APPROACH TO RESERVOIR CHARACTERIZATION

Reservoir characterization can be defined as the accurate spatial description of reservoir properties at the scale necessary for optimal resource development. It is an activity that requires a detailed understanding of the geology (i.e., the reservoir matrix), the spatial distribution of petrophysical properties, the fluids and their distribution, and the possible interaction between the reservoir and the recovery processes. Reservoir characterization leads to more realistic numerical models and thus better performance predictions. It leads also to improved well locations, enhanced sweep efficiency, an extended productive life, and increased oil recovery (Burchfield and Honarpour, 1989). Taking all this together means optimized production.

The approach taken in this study has been a sequential one (Figure 3). Initially, a detailed geological model was developed through an understanding of lithofacies and depositional environments, fluid distributions, and pore systems. The reservoir was subdivided into two parts: a "relatively uniform" sandy component with property variations in a relatively narrow range, and a heterogeneous component characterized by extreme property variations. Different characterization techniques were developed for these two parts to scale up core-scale permeability and porosity values to the scale required by the exploitation team for the construction of realistic numerical reservoir models. These techniques will be discussed in detail in later chapters of this report.

The sandy component of the reservoir was subdivided into four flow units, based on lithology, fluid saturations, pore systems, and porosity and permeability variations. These were defined such that any point within a flow unit has characteristics similar to all other points in the same unit, and different from those in other units. For the four sandy flow units, porosity and permeability data were scaled up from the core scale to the flow unit scale on a well-by-well basis using appropriate statistical averaging techniques. For the heterogeneous flow unit, the scaling up of permeability was carried out by means of numerical simulations. This approach provides the reservoir engineer with data at the flow unit scale, suitable for developing single well reservoir simulation models (Figure 3). The development of single or multiwell simulation models needs to be done in cooperation with the reservoir engineer. Because this study did not have access to a reservoir engineer who was actively working on the Provost Upper Mannville B Pool, development of these models was not included in the study. In addition to characterizing the reservoir flow units on a well-by-well basis, characteristic values for all the units on a pool or reservoir basis were also calculated for use in regional or basin modelling.

The question of interwell variability of reservoir properties was not addressed in this study. There are a variety of methods available for interwell prediction in the engineering and scientific literature, ranging from conventional geologic interpolation between wells to numerical simulation methods. Haldorsen and Damsleth (1990) present a review and summary of various models used by the petroleum industry to predict interwell variability of rock properties. The reader is referred to the literature for further information on methodologies for the interwell prediction of reservoir properties.

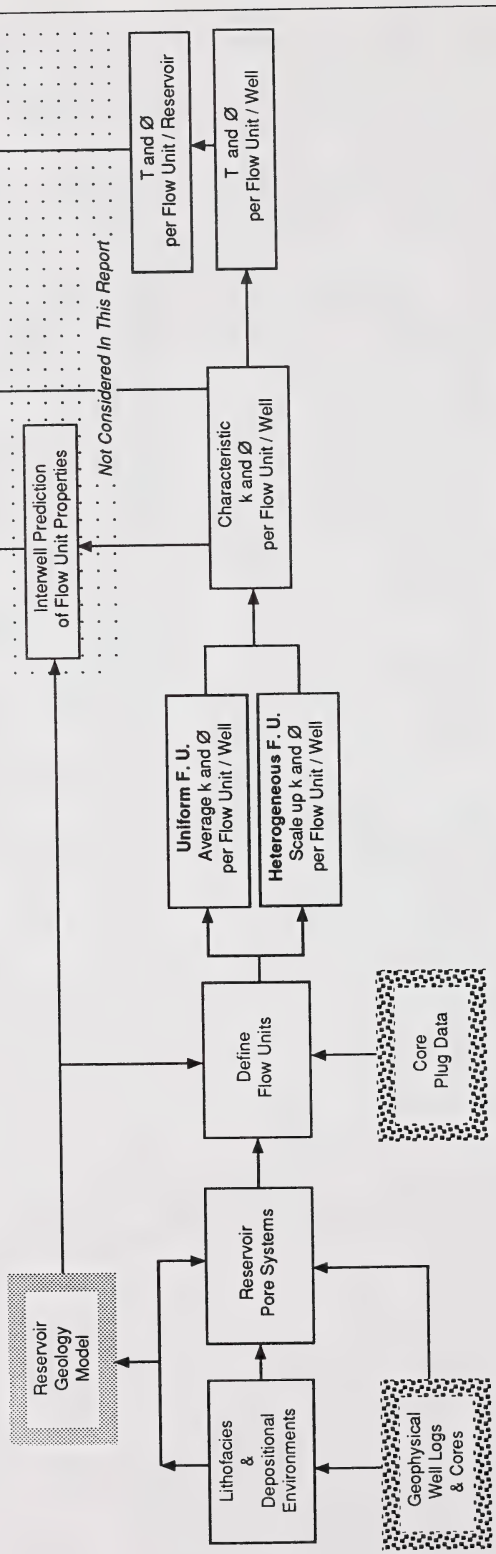
Geophysical Well Logs & Cores
Lithofacies & Depositional Environments
Reservoir Pore Systems
Reservoir Geology Model
Core Plug Data
Define Flow Units
Uniform F. U. Average k and Ø per Flow Unit / Well
Heterogeneous F. U. Scale up k and Ø per Flow Unit / Well
Characteristic k and Ø per Flow Unit / Well
Interwell Prediction of Flow Unit Properties
Not Considered In This Report
Multi-well Reservoir Simulation Model
Single Well Reservoir Simulation Model
Basin Analysis Model
T and Ø per Flow Unit / Reservoir
T and Ø per Flow Unit / Well

Figure 3. *Flow chart of the reservoir characterization process used in this study.*

RESERVOIR GEOLOGY

The Provost Upper Mannville B Pool reservoir is contained in McLaren Formation sands of Upper Mannville (Lower Cretaceous–Lower Albian) age (Figure 2). The mixed marine and continental sand/shale sequence of the Mannville Group unconformably overlies Paleozoic carbonate rocks and in turn is unconformably overlain by the marine Joli Fou shales of the Colorado Group. The McLaren Formation along with the overlying Colony and underlying Waseca Formations form the Upper Mannville Group.

The regional setting of Mannville sediments has been discussed by numerous authors. The most recent detailed treatment is provided by Jackson (1984) in a series of paleogeographic maps covering selected time intervals through the Mannville Group. Other authors who have considered the regional geology of Mannville sediments in the heavy oil region include Orr et al. (1977) and Vigrass (1977). Geological studies which focus on the McLaren Formation include papers by Gross (1980, 1981a and b) on the Provost Upper Mannville B Pool reservoir, and Richardson and Vigrass (1984) and Vigrass et al. (1987) on the Neilburg McLaren pool in Saskatchewan.

A number of depositional cycles are recognized within the Mannville Group in central Alberta and western Saskatchewan. Sheet sands in these cycles can be correlated over large areas using a combination of geophysical well logs and cores. The cycles are composed of shale to sand couplets which may have an associated coal, such as commonly found in the Sparky Formation. A number of thick, linear trending, sand bodies are found cutting through some of these cycles. These are considered to be of channel origin by most authors. On a regional basis, the McLaren Formation is one such cycle and usually consists of one or two small coarsening upward shale to sand sequences. In the Provost area of east central Alberta, the regional McLaren is cut by a thick sand sequence of fluvial origin that forms the reservoir for the Provost Upper Mannville B Pool (Figure 1).

Lithofacies

The McLaren Formation in the Provost area can be subdivided into a regional McLaren and a McLaren valley fill sequence. The regional McLaren consists of two thin, regionally extensive, coarsening upward shale to sand/silt cycles. Each of these probably represents a nearshore or shallow marine sequence deposited in the seaway that occupied the area in late Mannville time. Because the Provost Upper Mannville B Pool reservoir is contained within the sediments of the valley fill sequence, the regional McLaren will not be considered further.

Figure 4 presents an isopach of the valley fill sequence and shows the thickness and location of the valley which was cut into the regional McLaren and underlying Waseca Formations as a result of a drop in the base level. As the base level rose again, the valley filled with sediments, which now form the valley fill sequence. Figure 5, a west-to-east stratigraphic cross section, shows the geometry of the valley fill. These sediments can be subdivided into a number of lithofacies which are lithologically distinct and also represent different depositional environments. These lithofacies are recognizable on geophysical well logs and in cores. Figure 6 presents a well log with lithology, showing five of the six lithofacies for the Provost Upper Mannville B Pool reservoir.

Blocky channel lithofacies. The blocky channel lithofacies (Figures 6 and 7) is found at the base of the valley fill sequence and forms the main portion of the Provost Upper Mannville B Pool reservoir. It consists of trough and planar cross bedded, well sorted, quartz rich sands. Grain size varies from medium grained at the base to fine to medium grained near the top. The whole lithofacies is composed of sand, with no interbedded shale beds or laminae. Occasionally, carbonaceous laminae are found. Where seen in core, the base is sharp, with blocky channel sands cutting into regional McLaren shales and silts or into the underlying Waseca Formation silts and shales. Fragments from the Waseca are found only occasionally at the base of the sands. Oil saturation is typically in the 10 to 12 wt% range. This lithofacies has a low gamma ray signature and negative SP curve on geophysical well logs. The overall log shape is blocky, with a sharp base. The top is transitional with the overlying transition zone lithofacies (Figure 6).

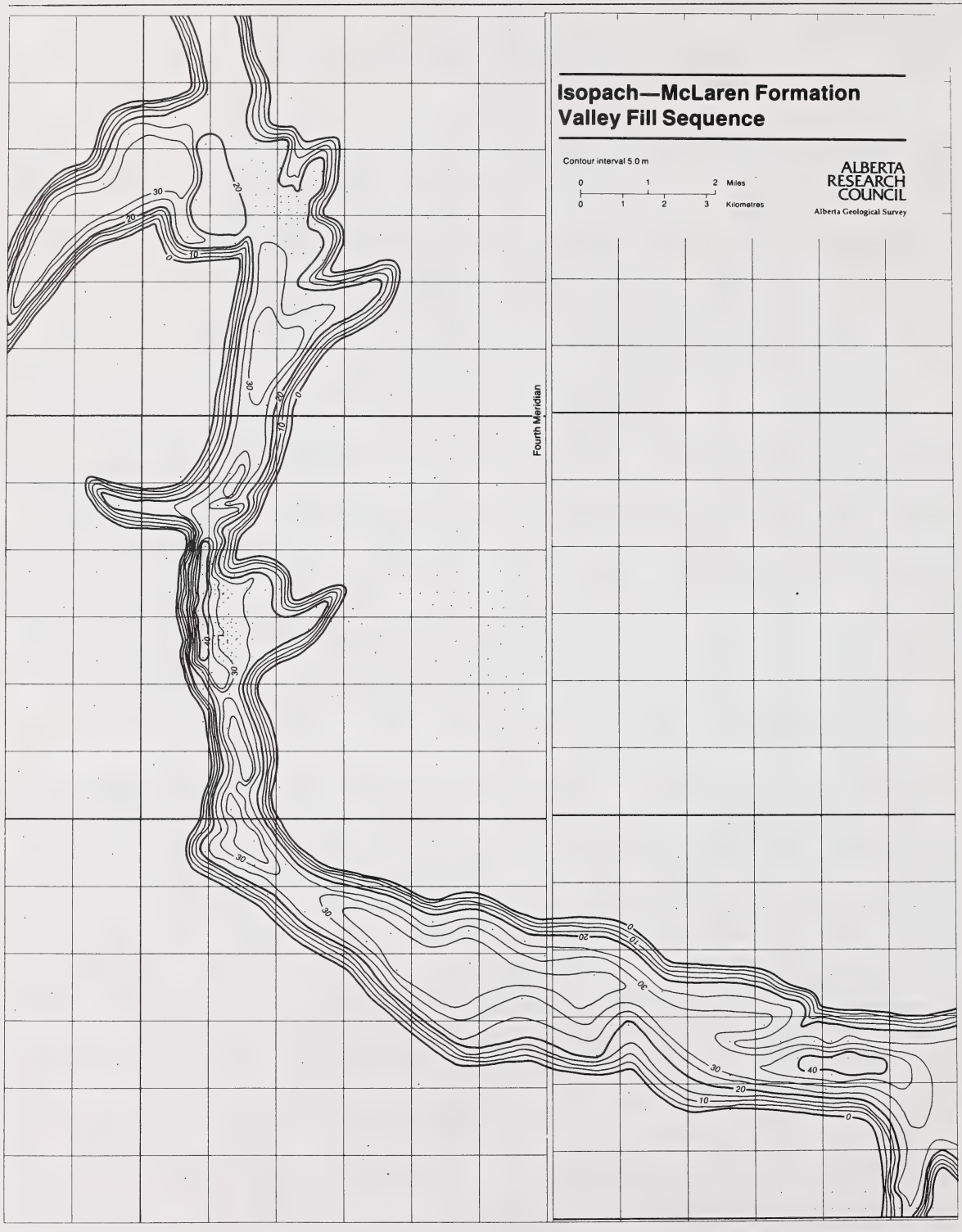

Figure 4. *Isopach, McLaren Formation valley fill sequence.*

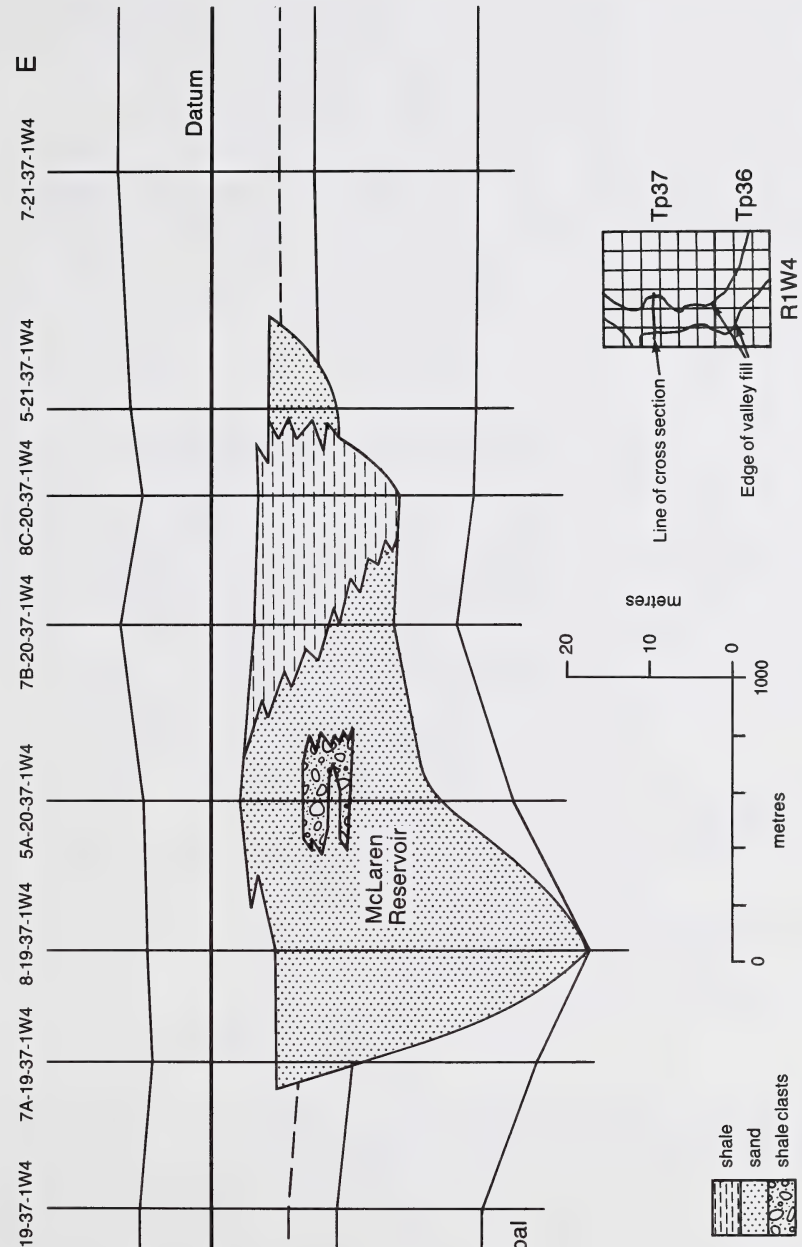

Figure 5. *West-to-east stratigraphic cross section through the Provost Upper Mannville B Pool showing the valley-shaped geometry for the valley fill sediments.*

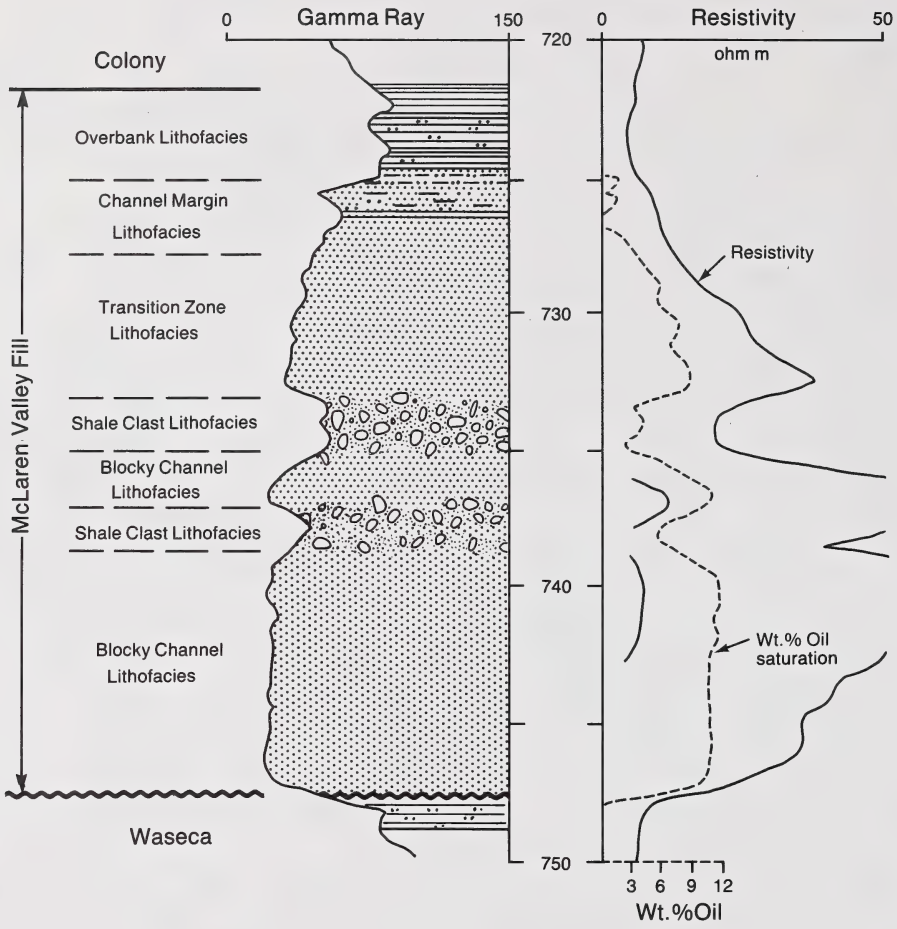

Figure 6. *Typical well log from the Provost Upper Mannville B Pool showing four of the five lithofacies of the McLaren valley fill sequence.*

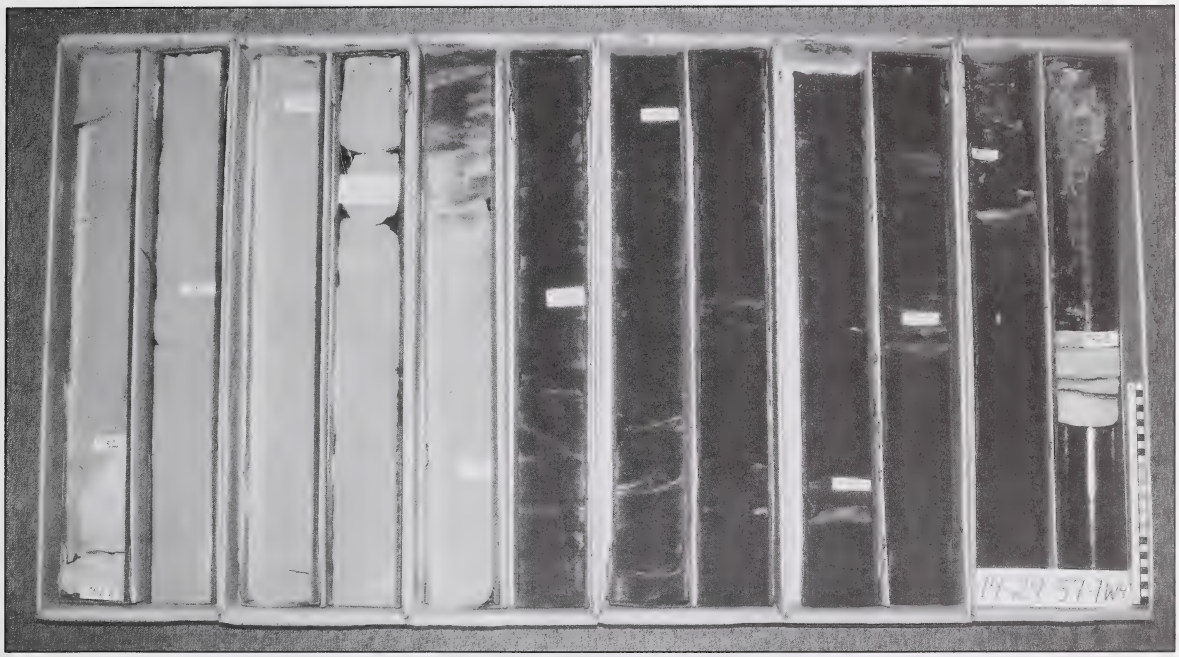

Figure 7. *Core photograph of the blocky channel lithofacies. The dark portion of the core is oil saturated and the basal light colored portion is water saturated. Top of the core is in the upper right hand corner and the bottom of the core is on the lower left of the photograph. Each core length is approximately 75 cm. The scale bar is in cm. (14-29-37-1W4, 742.5–752.2 m depth KB)*

The blocky channel facies is the thickest of all lithofacies, up to 20–25 m, and is interpreted as having been deposited in the main part of the channel complex that occupied the McLaren valley.

Transition zone lithofacies. The transition zone lithofacies (Figures 6 and 8) overlies and is transitional with the underlying blocky channel lithofacies and grades upwards into the overlying channel margin lithofacies. Grain size decreases upwards from fine to medium grained at the transition with the blocky channel lithofacies, to very fine grained at the top. Sedimentary structures vary from cross bedding at the base, to laminations, ripple laminations, and current ripples near the top. Carbonaceous laminae occur occasionally. Oil saturation decreases upwards to the 4 wt% range, as a result of the fining upward nature of the lithofacies. This is shown in core by a gradual lightening from the dark brown or black color (high oil saturation) in the underlying blocky channel sands (Figure 8, ~732 to 735.5 m). The thickness of this lithofacies is highly variable, but can be up to 5 m.

The log signature of this lithofacies (Figure 6) is transitional from the blocky channel sands to the channel margin sand, silts, and shales. The gamma ray curve gradually increases, while the resistivity decreases.

Shale clast lithofacies. The shale clast lithofacies (Figures 6 and 9) is found within the blocky channel and transition zone lithofacies and could be considered a subfacies. Occasionally, shale clasts are found in the channel margin lithofacies. This lithofacies consists of shale, silty shale, or carbonaceous siltstone breccia clasts in a matrix of fine to medium grained sands. The clasts vary in length from less than a centimetre to decimetres. Their shape varies from equant to flat and from well rounded to very angular. Some of the clasts are structureless, whereas others show laminations, and still others show soft sediment

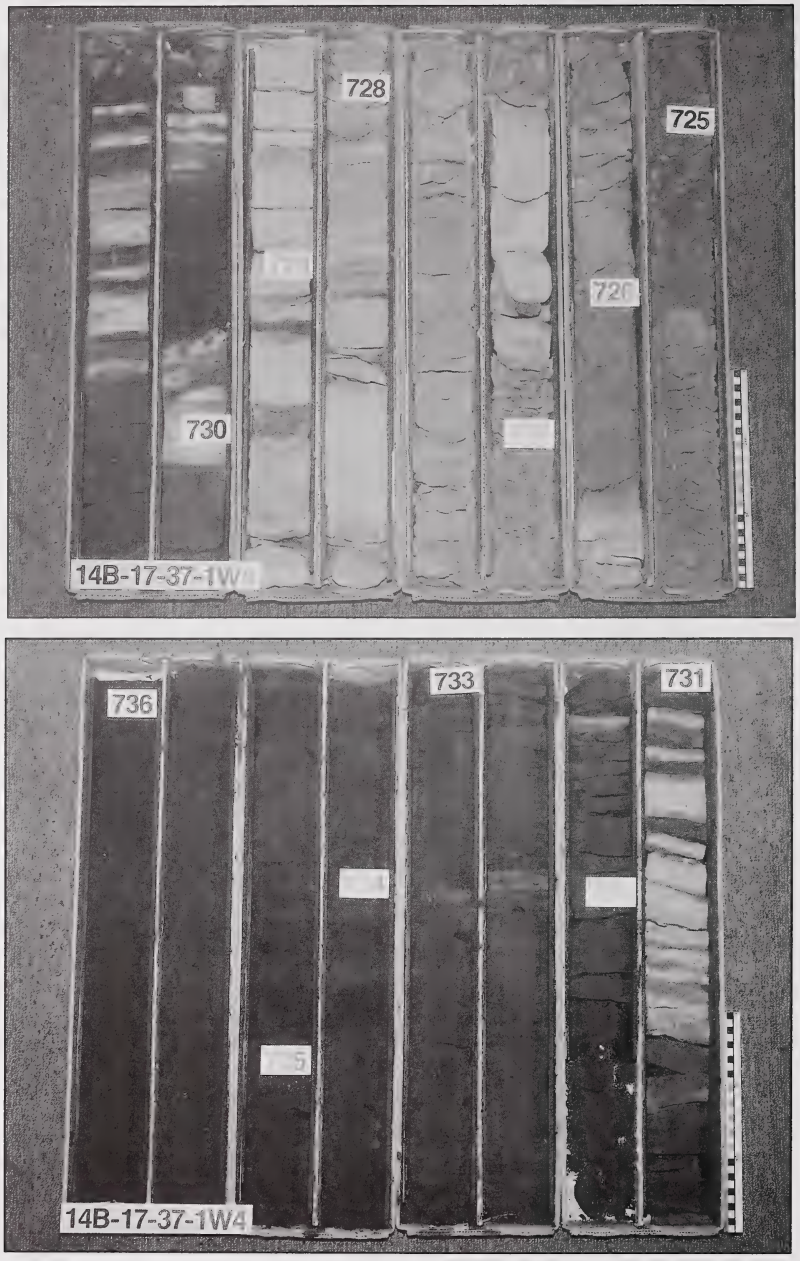

Figure 8. *Core photographs of the transition zone, channel margin and overbank lithofacies (14B-17-37-1W4, 724.8–736.7 m depth KB). The transition from the blocky channel sands to the transition zone sands occurs between 735 and 736 m; from the transition zone sands to the interbedded sand and shale beds of the channel margin lithofacies occurs at about 731.8 m; and from the channel margin to the overbank lithofacies occurs at about 729.4 m.*

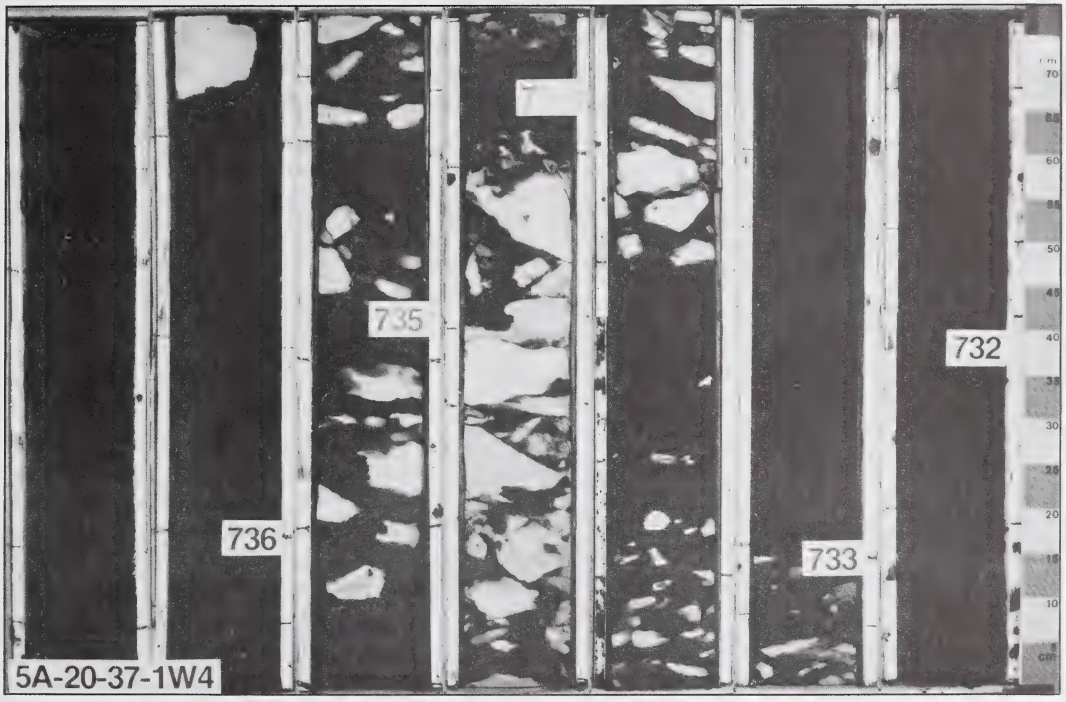

Figure 9. *Core photograph of the shale clast lithofacies (5A-20-37-1W4, 731.3 – 737.0 m depth KB).*

deformation structures. The density of clasts varies from an occasional clast to as high as 70% in core cross section. Large clasts can be distinguished from shale beds by their contacts with the sand matrix or by the orientation of the contained sedimentary structures.

The gross thickness of the shale clast lithofacies is up to 14 m, with the thickest continuous layers being 3 m. Lateral continuity of intervals with shale clasts (shale clast zones) is expected to be on the order of tens to hundreds of metres. In the area of the steam pilot in Sec. 20, Twp. 37, Rge. 1W4, shale clast zone intervals can be correlated across the pilot in an east to west direction, a distance of 400+ m. In the north to south direction, the same interval can only be correlated between two wells 25 m apart, and not between the wells which are 400+ m apart. Figure 10 shows the areas within the Provost Upper Mannville B Pool reservoir where shale clast zones have been identified from cores and geophysical well logs .

The shale clast lithofacies is recognized on geophysical well logs by an increase in the SP and gamma ray curves compared to the blocky channel and transition zone lithofacies (Figure 6). The deflection is not as large as one would expect from a shale bed of equivalent thickness. The resistivity curve decreases to a lower value, indicating the lower overall oil content than that of the enclosing sands.

The shale clast lithofacies is interpreted to have been deposited in the main part of the channel complex, with the clasts coming from erosion of the channel cutbank. Shale clasts are not unique to the Provost Upper Mannville B Pool. They have been observed elsewhere in the McLaren Formation (Figure 12), as well as in other reservoirs of channel origin, such as the McMurray Formation in the Athabasca Oil Sands.

Channel margin lithofacies. This lithofacies is the uppermost of the sandy lithofacies and is found overlying the transition zone lithofacies (Figures 6 and 8). It consists of argillaceous and silty sands with interbedded silty shale and shale beds (Figure 8, ~729.4 to ~731.8 m). In the sands, grain size varies from fine to very fine grained at the base, to silty at the top. Sedi-

Figure 10. *Isopach, shale clast zones net thickness.*

mentary structures are usually restricted to fine laminations and wavy to cross laminations or ripples. Occasionally, soft sediment deformation can be seen. Burrows, predominantly vertical in orientation, are found in this lithofacies.

The thickness of the channel margin lithofacies varies from one to five metres. Deposition is interpreted as having occurred on the edge and on top of the channel complex point bar. Palynological samples indicate mainly continental and occasionally slightly brackish depositional conditions.

Overbank lithofacies. Overlying the channel margin lithofacies, and transitional with it, are a series of green to greenish gray shales and silty shales of the overbank lithofacies (Figures 6 and 8). Some interspersed silty laminae or thin beds can be found near the base of this lithofacies. Carbonaceous debris is found scattered throughout the shale and occasionally concentrated in laminae. Contorted bedding or soft sediment deformation structures are also present in this lithofacies. Burrows are scarce and, where they occur, usually vertical to nearly vertical in nature. Rootlets and/or waxy mudstones with slickensides are present near the top of this lithofacies; these may represent a soil horizon (Figure 8, 725 m).

On geophysical well logs, this lithofacies can be recognized as a shale overlying the sandy lithofacies.

The overbank facies, which varies in thickness from 3.0 to 23.7 m, is interpreted to have been deposited in the overbank areas of the channel complex. Palynological evidence indicates occasional slightly brackish conditions.

Abandonment lithofacies. This lithofacies is recognized in both cores (Figure 11) and logs. In most cases it is a thick structureless shale to silty shale sequence with thin interbedded silt or sand laminations. Rootlets and polycheate worm burrows are commonly present. Usually, this lithofacies overlies a thin interval of cross bedded sands from the blocky channel lithofacies.

The abandonment lithofacies is identified on geophysical well logs as a thick shale sequence that is laterally equivalent to either the blocky channel, transition zone, and/or channel margin lithofacies. In those cases where there is a thick underlying blocky channel sequence, it is difficult to distinguish the abandonment lithofacies from the overbank lithofacies.

Depositional Environments

Because this study is concerned with the Provost Upper Mannville B Pool reservoir and because cores are not available through the regional McLaren in this area, only the origin of the valley fill related sediments will be discussed. The development of the sequence stratigraphy concept by Vail and his coworkers (Haq et al., 1987; Wilgus et al., 1988; van Wagoner et al., 1990) has shown that sea level fluctuations have been the norm rather than the exception through geologic time. This relative lowering and rising of sea level also helps to explain the events that led to the deposition of the Provost Upper Mannville B Pool reservoir sediments.

After deposition of the regional McLaren Formation sediments in shallow marine and nearshore conditions, there was a lowering of base level, or relative sea level. As a result, a valley system was cut into the existing regional McLaren sediments and in some cases through the McLaren and into the underlying Waseca Formation. The large extent of this regional McLaren valley system in east central Alberta is shown in Figure 12. This map shows those segments that could be mapped with certainty, and also projected connections between the mapped segments. As base level rose, due to a rise in relative sea level, the erosional valley system was subsequently filled with fluvial sediments. This valley filling was accompanied by minor incursions of marine waters, resulting in slightly brackish conditions in parts of the valley system, as evidenced by polycheate burrows in some of the silts and shales and the rare presence of acritarchs and ceratioid dinoflagellates amongst the pollen and spores (C. Singh, pers. comm.).

The sequence of sedimentary structures (cross bedding → laminations → cross laminations → ripples) and sediment types (medium grained sand → very fine grained sand → silt and shale) found in most cores indicate a fluvial origin for the valley fill sediments. The lack of shale beds and fines in the sands also indicates a clean sandy system with enough energy to transport any fines further down-

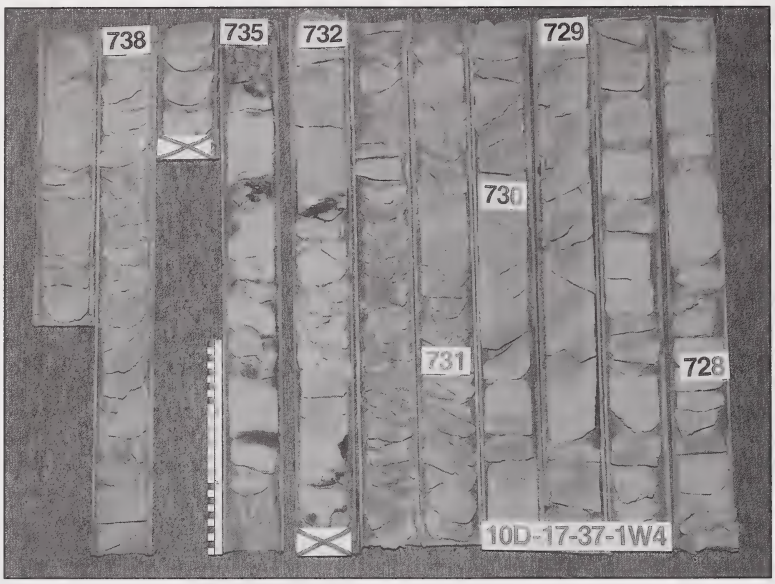

Figure 11. *Core photograph of the abandonment lithofacies (10D-17-37-1W4, 727.5–739.2 m depth KB). The whole cored interval in this well is interpreted as abandonment lithofacies. The large ✕ on the core indicates intervals of lost core. Well logs show these missing core intervals to be sandy.*

stream. Cores and logs indicate that the McLaren valley fill sequence north of the study area represents amalgamated sets of channel deposits. Wightman et al. (1987) have also interpreted some of these thick sand sequences in east central Alberta as stacked fluvial deposits. Thus, the interpretation of the depositional environment for the McLaren Formation valley fill sediments in the Provost Upper Mannville B Pool is that of a sandy fluvial system filling a pre-existing valley. A modern example of similar depositional conditions is found in the sandy, braided river deposits of the South Saskatchewan River in central Saskatchewan (Cant and Walker, 1978). Here, sandy fluvial sediments are also filling a pre-existing erosional valley.

Mineralogy

The mineralogy and diagenesis of the McLaren Formation valley fill sediments was studied using 57 samples from nine cores through the formation (Prentice and Kramers, 1987). In addition to point counting the sands of the blocky channel and channel margin facies for framework grain mineralogy, the clay mineralogy from the sands and some of the shaly lithologies were obtained by means of x-ray diffraction. Scanning electron microscopy and thin sections were utilized to study the diagenesis of the sands.

The sands of the Provost Upper Mannville B Pool reservoir are dominantly sublitharenites with a lesser subarkose component (Figure 13). Framework grain mineralogy is dominated by quartz (av. 85%), with minor potassium feldspar (av. 5%), chert (av. 4%), and volcanic rock fragments (av. 3%). Accessory minerals include muscovite, rutile, and tourmaline. The McLaren Formation sands differ significantly from the overlying Colony and underlying Waseca Formation sands, which have a much lower quartz content (av. 46–48%), a higher feldspar (av. 20%) and rock fragment (av. 17–20%) content (Figure 13).

Diagenesis in the reservoir sands was mainly restricted to clay mineral diagenesis and differs

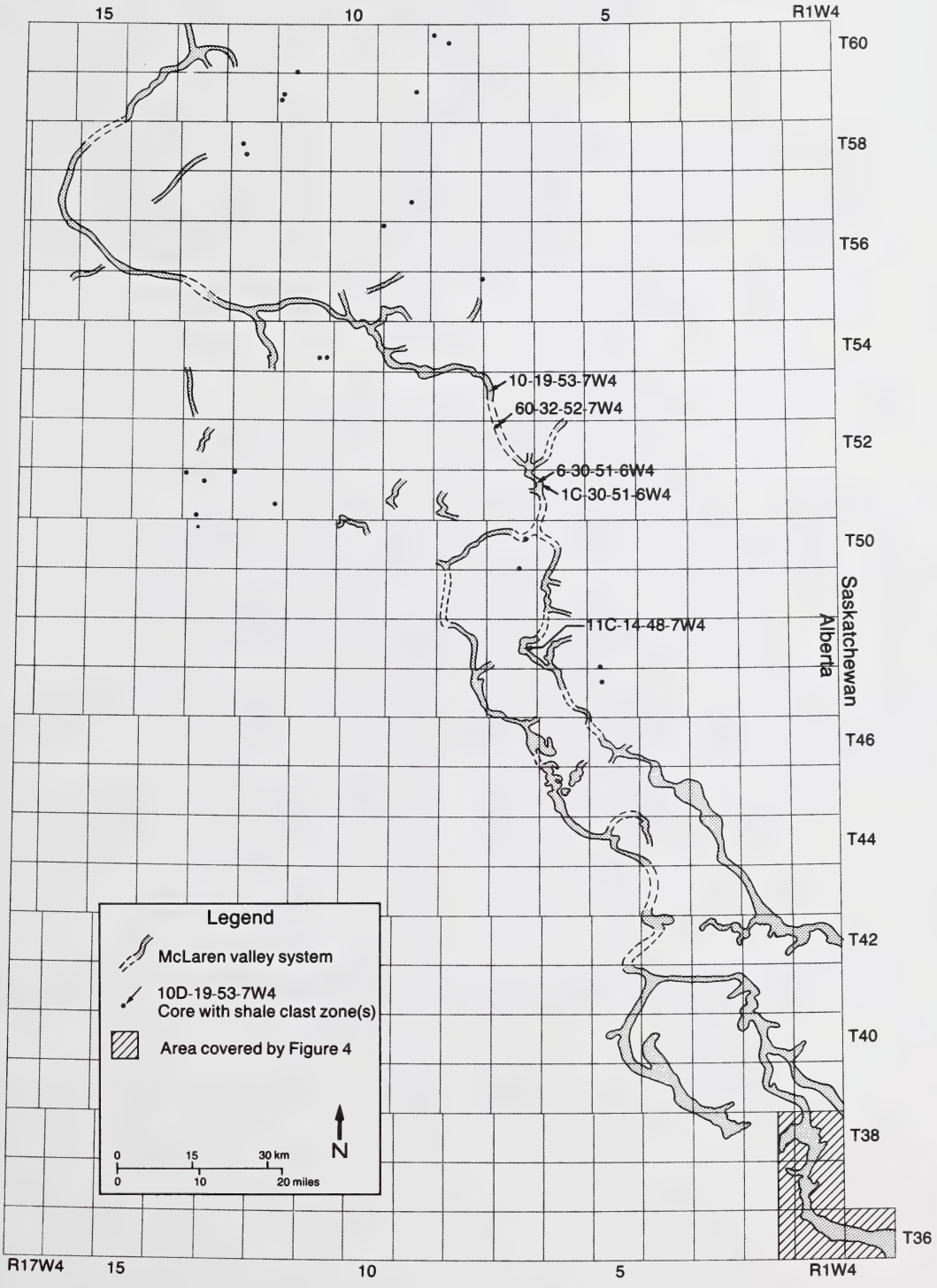

Figure 12. *Regional extent of the McLaren valley system in east-central Alberta. Mapped segments of the valley are indicated with a pattern and projected connections with dashed lines.*

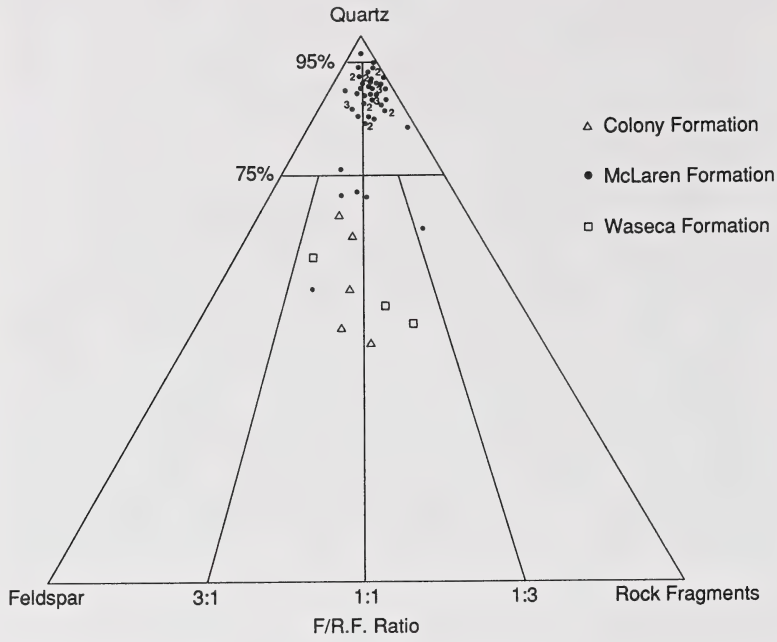

Figure 13. *Grain mineralogy of McLaren Formation valley fill sands in comparison with Colony and Waseca Formation sands.*

between the oil and water saturated sands. The dominant clay mineral is kaolinite, with lesser amounts of illite and traces of smectite and chlorite. In the oil saturated sands, kaolinite (85%) occurs in two habits: well formed booklets of 20–40 μm size in a pore filling habit; and poorly formed booklets of 2–6 μm size in a pore coating habit. Illite makes up approximately 10% of the oil saturated sands' clay fraction. The clay fraction in the water sands is slightly higher, kaolinite is less dominant (av. 60%), and sinuous pore bridging illite makes up about 35% of the clay minerals. Minor siderite is found in some of the water saturated sands.

Overall, the reservoir should have low reactivity with the high temperature injection fluids used in enhanced recovery (EOR) operations. Silica dissolution is likely to occur, but the low concentration of possible deleterious minerals, such as smectites and carbonates, makes the reservoir well suited for EOR operations. Because of the unconsolidated nature of the reservoir, a possible formation related problem that could be encountered is the production of sand.

THE RESERVOIR

The Provost Upper Mannville B Pool reservoir is contained entirely within the blocky channel, transition zone, shale clast, and channel margin lithofacies of the McLaren valley fill sequence. Figure 14 is an isopach of the combined thickness of the blocky channel, transition zone, shale clast, and channel margin lithofacies, and represents the gross reservoir thickness. The maximum reservoir thickness of approximately 35 m occurs in sections 17 to 20 in Twp. 37, Rge. 1W4. The reservoir has a long and narrow trend (approximately 15 by 1.5 km) as a consequence of the channel origin of the reservoir sands. Along the western margin, the reservoir edge is sharp and steep and the blocky channel lithofacies sands are in direct contact with the valley walls (Figures 5 and 14). In contrast, the eastern margin of the reservoir has an irregular edge because of the dominance of the finer grained sediments of channel margin and abandonment facies (Figures 5 and 14).

Figure 15, the net oil pay for the Provost Upper Mannville B Pool reservoir, and Figure 16, a north-to-south structural cross section, show that the reservoir can be divided into two oil pools with a common oil/water contact. These pools are stratigraphically controlled by a shale plug (overbank and abandonment lithofacies in well 11-28-36-1W4) separating them. The maximum net pay varies from 13.0 m in the southern portion to 26.5 m in the northern portion of the reservoir, where most of the pilot activity has taken place.

Figure 17 shows the thickness of the water column that underlies the oil saturated sands of the Provost Upper Mannville B Pool reservoir. The two pools in the reservoir are in fluid communication through the water leg (Figure 16). At the base of the oil column there is usually a transition zone, varying in thickness from 1.5 to 4.0 m, where the water saturation is above Sw_{irr}. This transition zone can be identified on well logs based on the gradual change in resistivity from the water leg to the oil saturated portions of the reservoir. The original reservoir pressure, when the pool was discovered in 1972, was approximately 5450 kPa, at a reservoir temperature of 27°C. The oil density is 979 kg/m^3 and the in-situ viscosity of the oil is 2300 mPa·s (Nazarko, 1983).

Because the sand matrix in the shale clast zone is the same as in the surrounding blocky channel sands, it is assumed that the matrix sands have the same petrophysical properties. The presence of impermeable shale clasts therefore lowers the value of the effective permeability in the shale clast zones, compared with the surrounding blocky channel sands, thus constituting a barrier to fluid flow in the reservoir. Methodologies to determine effective values of permeability in the shale clast zones are presented in a later section of this report.

Porosity values in the blocky channel lithofacies average close to 33%, with maximum oil saturation near 80%. Both porosity and oil saturation decrease through the transition zone into the channel margin sands lithofacies as a result of an increase in the fines content and a decrease in the grain size. Horizontal air permeability values of 5 darcies have been measured in fresh core samples from the blocky channel lithofacies. They decrease to the hundreds of millidarcies range near the top of the channel margin lithofacies. Directional permeabilities, although not measured, should be highest approximately along the channel trend. This is not necessarily parallel to the valley trend, because of meandering and sinuosity of the flow within the channel system and flow around bars within the channel system. In general, however, directional permeability should be greatest in a direction subparallel with the valley system.

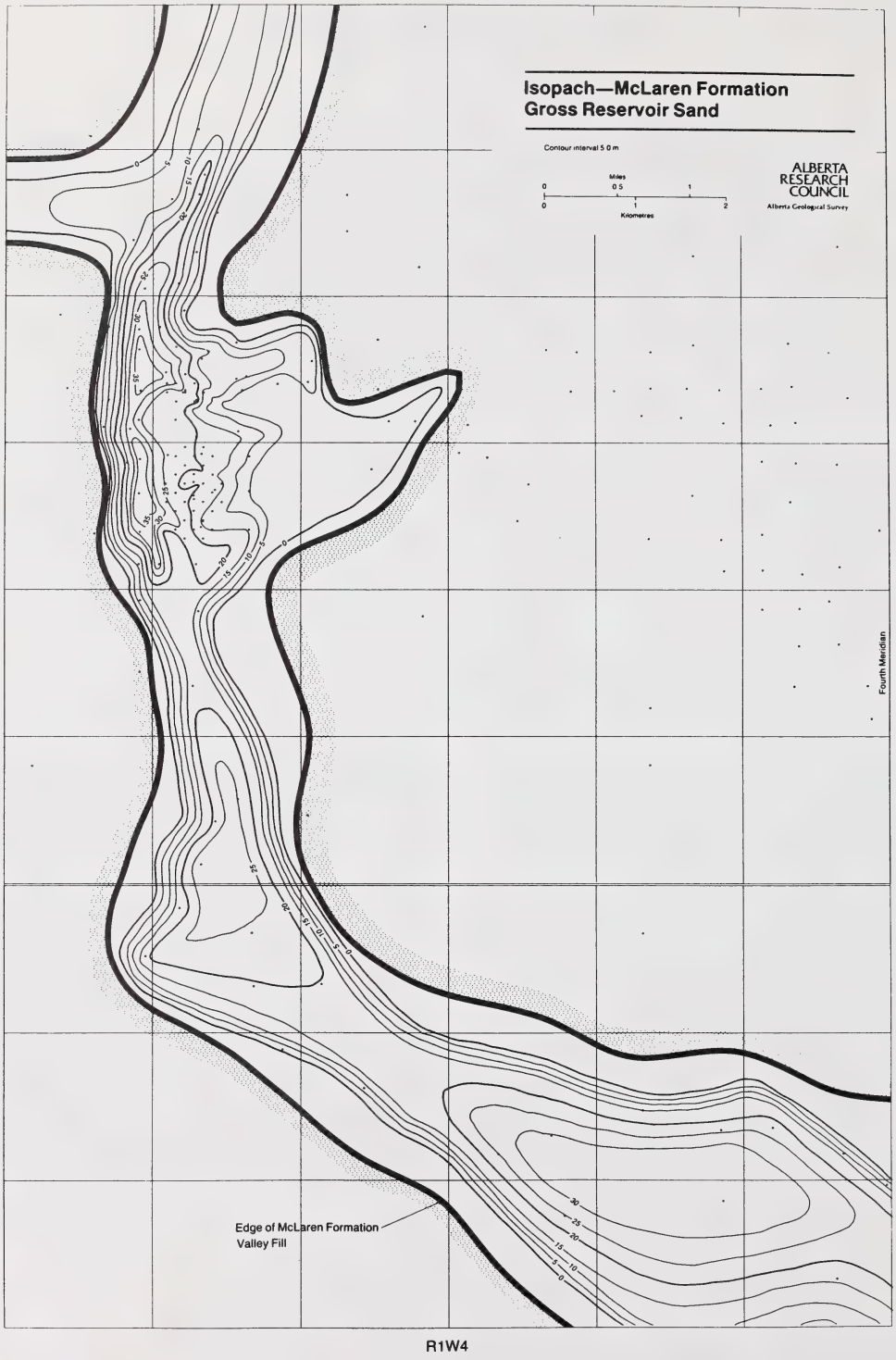

Figure 14. *Isopach, gross reservoir sand thickness.*

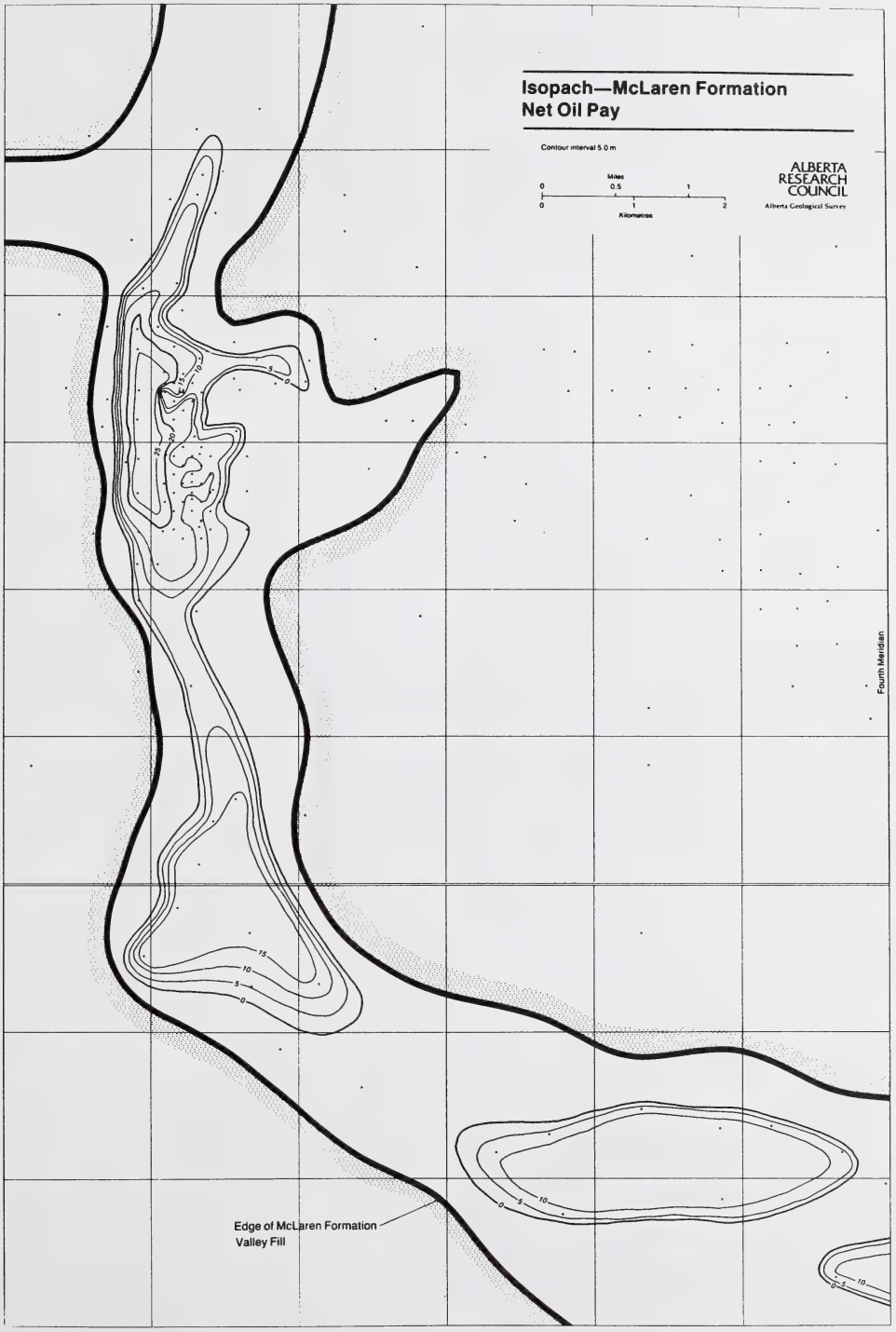

Figure 15. *Isopach, net oil pay.*

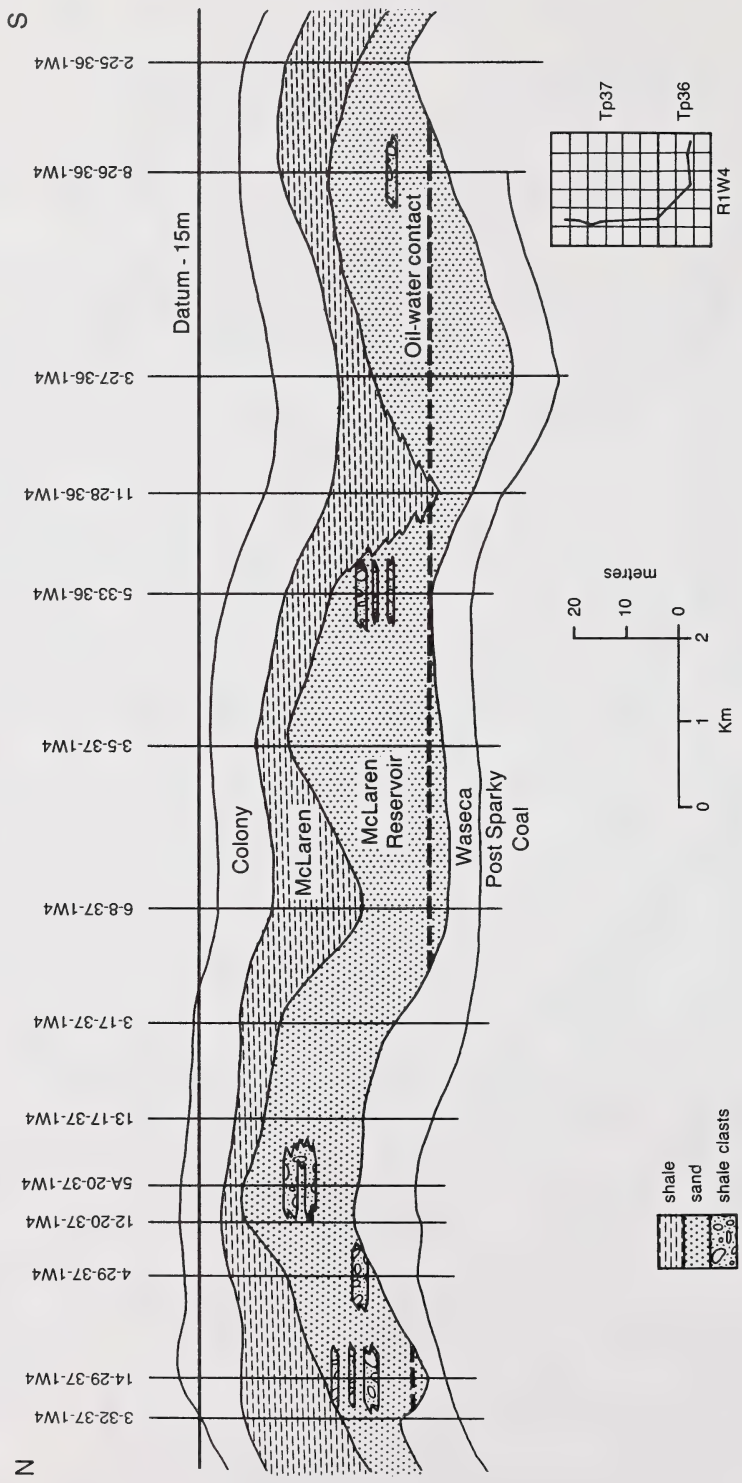

Figure 16. *North-to-south structural cross section through the Provost Upper Mannville B Pool. The two oil pools are separated by a shale plug in well 11-28-36-1W4, but have a common water leg.*

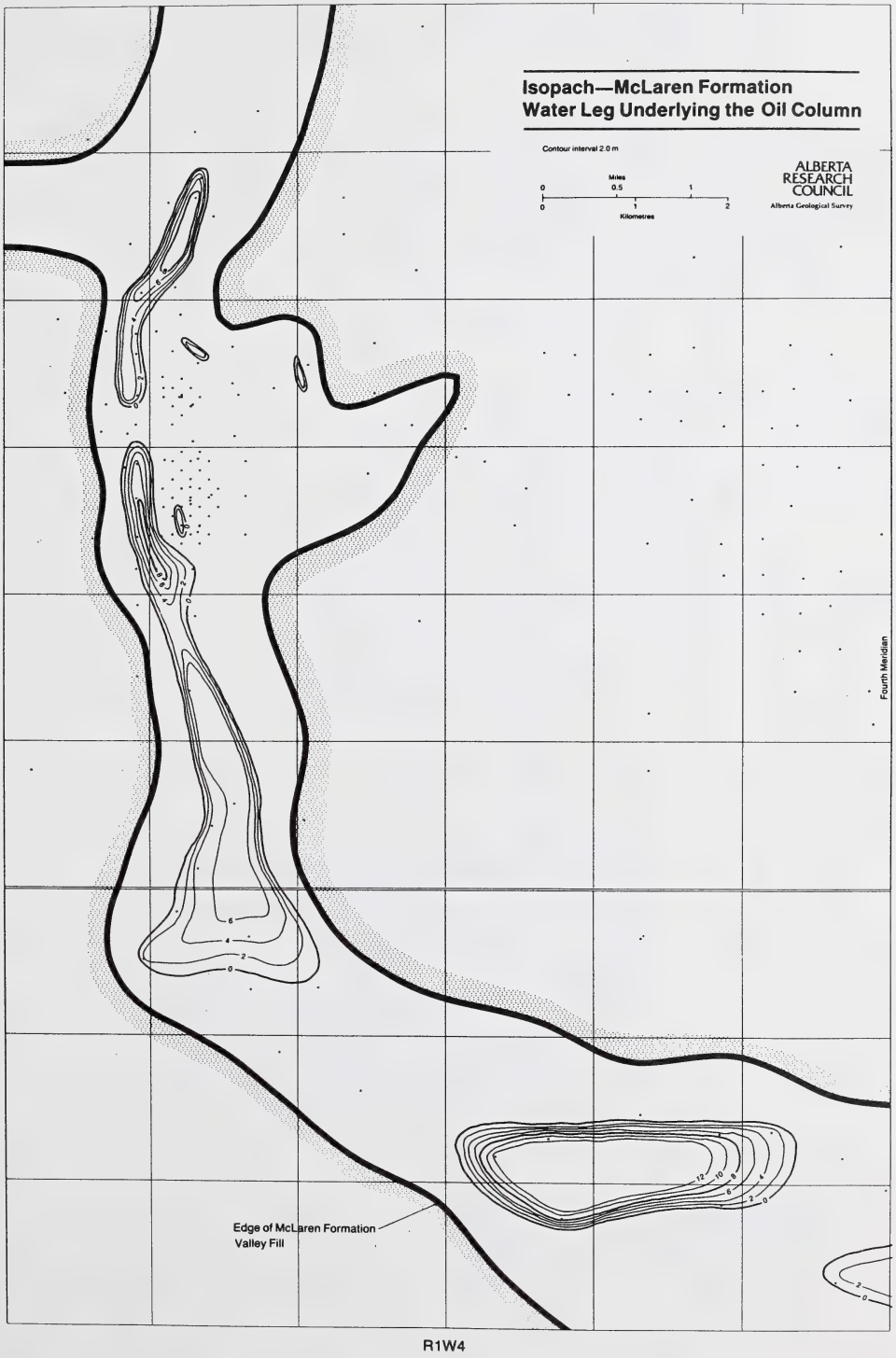

Figure 17. *Isopach, water leg underlying the oil column.*

RESERVOIR SUBDIVISION

The overall characterization of the Provost Upper Mannville B Pool has to include not only a geological description, such as reservoir lithofacies, geometry, and fluid content, but also a delineation of the reservoir flow units. Flow units are subdivisions of a reservoir which have distinct hydrodynamic properties. They are characterized by similar petrophysical properties (such as permeability and porosity), lithology, pore systems, and fluid characteristics and saturations. Data on these properties can be acquired at a large range of scales (Figure 18), from the microscopic or pore scale to the reservoir scale. At the pore scale, thin section and image analysis studies can provide data on pore and pore throat sizes, pore connectedness, and pore system properties. Physical measurements of porosity and permeability can be obtained at the core scale. At the bed or flow unit scale and extending a short distance from the well bore, information on petrophysical properties is captured by drillstem tests and geophysical well logs, as well as from scaling up of data from the smaller core scale. Obtaining data on properties at the reservoir scale is usually limited to a variety of well tests (e.g., injection and production tests, pressure tests), and the scaling up from the core and bed or flow unit scale.

A scaling up approach (Lasseter et al., 1986) from core to reservoir scale was adopted in order to characterize the petrophysical properties of the flow units in the Provost Upper Mannville B Pool. In addition, a characterization of the pore scale reservoir properties was undertaken in order to obtain a better understanding of the reservoir.

On the basis of lithology and internal heterogeneity, the Provost Upper Mannville B Pool can be

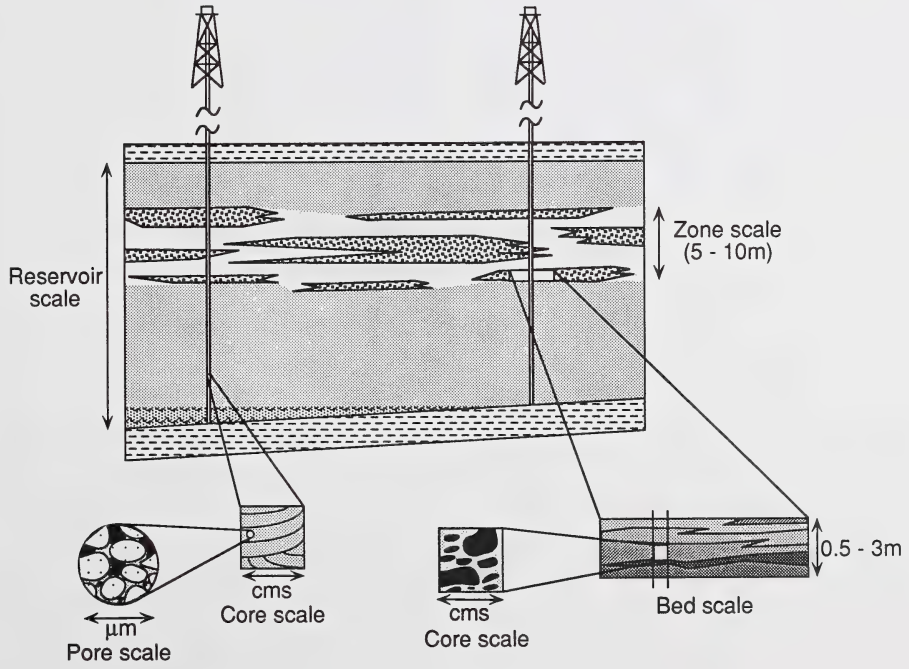

Figure 18. *Scales of characterization for the Provost Upper Mannville B Pool.*

divided into two major parts: the "relatively uniform" sandy portions, and the heterogeneous shale clast zones. The shale clast layers and zones show a high variability of petrophysical properties at the core and larger scales, and can be considered as a single flow unit. The sandy portions of the reservoir, comprising the blocky channel, transition zone, and channel margin lithofacies, have a much lower variability in their petrophysical properties. These lithofacies represent a natural gradational sequence from the main channel complex, to the margins of the channel, and to the point bar. Both porosity and permeability values decrease upwards through these lithofacies, as a result of the fining upward trend in reservoir lithology. Because of this gradational nature, the sandy portion of the reservoir cannot be characterized as a single flow unit. Rather, it has to be divided into a number of subunits, based on their flow characteristics. Each of these flow units is then characterized separately. This is done in the chapter on sandy facies characterization. The pore systems of the Provost Upper Mannville B Pool reservoir are characterized first, in order to aid in the definition of the reservoir flow units.

PORE SCALE CHARACTERIZATION

In order to understand and predict the fluid-flow properties of porous media, petrographic image analysis (PIA) has been used in studies of two-dimensional (2D) pore geometry (Matheron, 1967, 1975; Rink and Schopper, 1978; Ehrlich et al., 1984; Ruzyla, 1986; Berryman and Blair, 1986; Doyen, 1988; Ehrlich and Davies, 1989). This analysis has the potential to estimate flow properties quickly and cheaply, and it can be performed on small samples such as drilling cuttings of consolidated rocks.

For the unconsolidated oil sands and heavy oil reservoirs, which do not produce cuttings during drilling, PIA has the potential to provide flow property information on a less expensive and faster basis than some of the special core analyses (e.g., capillary pressure, irreducible and residual saturation, relative permeability, and foaming capability). If the relationship between these special core analyses and pore geometry can be quantified and understood, flow properties can be estimated economically and quickly by PIA for a detailed reservoir characterization.

In addition to potentially predicting flow properties, PIA can also help to define flow units and to understand the relation between geological processes and fluid flow in the reservoir. Such an understanding can assist in a better use of geological information in developing a quantitative reservoir model. In this study, relations between flow properties (permeability and capillary pressure) and pore geometry are established; pore types are identified and linked to the lithofacies, and a new image analysis algorithm is developed to improve the PIA technique.

Image Analysis Method

Previous methods. Different approaches have been used to analyze binary pore images, which are composed of either pore or non-pore pixels (picture elements). The porosity and specific surface area of a sample can be obtained by directly measuring the pore area and the perimeter, or by indirectly measuring a two-point correlation function on the image (Berryman and Blair, 1986). These two parameters can theoretically be used to predict permeability by using a Kozeny–Carman type of equation (see Walsh and Brace, 1984, for a review). However, the surface area measured from pore images is usually a function of resolution (i.e., magnification). Therefore, choosing the proper magnification becomes crucial to permeability prediction.

Other measurements such as size, shape, and connectivity are more difficult to obtain or even to define, because of the interconnection of pores in a pore network. In the three-dimensional (3D) space, all the effective porosity is interconnected. Three-dimensionally isolated pores are less important, due to their irrelevance to fluid flow. The three-dimensionally connected effective porosity is not necessarily interconnected on a 2D image. Two-dimensional connectivity varies from highly connected pore images of unconsolidated materials to the highly disconnected 2D porosity of most consolidated materials. Because of the difficulty in defining a single pore object in a 2D image, some conventional size measurements such as Feret's diameter (Feret, 1931) and Wadell's diameter (Wadell, 1932) become questionable. A "cutting" algorithm (Rink, 1976) has been used to disconnect the pore network and analyze the isolated pieces of porosity. However, because narrow restrictions in a pore network are very important to flow processes, some valuable information is probably altered or lost during the "cutting" process.

Generalized size analysis method. Delfiner (1972) defined a generalized concept of size which does not require a predefined single object and is especially suitable for irregularly shaped and/or interconnected objects such as pore images. He used a series of "opening" image processing operations to perform the analysis. An opening with a circular structuring element of radius r removes a strip of porosity with the width r along the pore boundary (erosion) and then adds a strip of porosity with the same width back on the pore (dilation) (Figure 19). Small features are lost and cannot be recovered, whereas large features shrink and then expand back to their original size. With different sizes of structuring elements, features with various sizes can be identified by performing a series of opening operations (Figure 20).

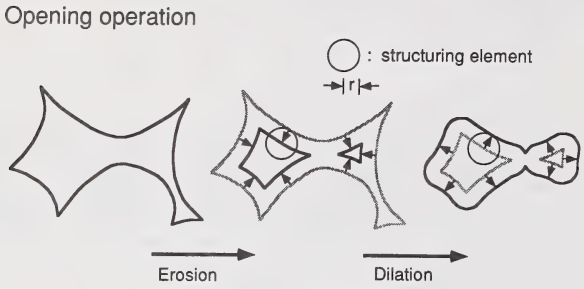

Figure 19. *Example of an opening operation with a disk of radius r.*

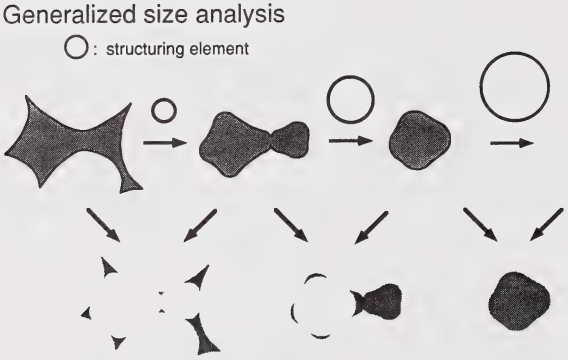

Figure 20. *Example of three opening operations with increasing structuring elements to differentiate pore areas with different size.*

Mathematically, the size measurement of each point of pore area is equal to the radius of the largest inscribed circle that contains the point and lies entirely within the pore area. This size definition was suggested by Scheidegger (1960) to characterize the pore size; however, a practical measuring technique was not available until the development of computerized image analysis. One of the results of the present study is a new and improved algorithm to perform this generalized size analysis. This new algorithm is presented in Appendix A.

The generalized size analysis algorithm is closely related to mercury porosimetry analysis, which measures the saturation versus the radius of the interface curvature at a given pressure. This is similar to measuring the remaining porosity versus the radius of the structuring element for a given opening operation in the generalized size analysis (Figure 20).

Connectivity indicator. A two-dimensionally connected area of porosity can be defined as a "porel" (pore element) or a "blob." Thus, for a completely connected 2D pore image, only one porel is identified. Having many porels in an image means that the 2D porosity is distributed into many disconnected areas. Therefore, the number of porels in an image could be used as a measure of pore connectivity. A similar definition was used by Serra (1982) to define a "connectivity number." However, these numbers do not consider the "weight" of porosity. A highly connected 2D pore image may have many small (e.g., one pixel) disconnected porels associated with it. These small porels are not very important in terms of fluid flow, due to the small amount of porosity, but they result in a large porel count which indicates a disconnected pore image.

Ehrlich et al. (1984) classified porosity into smooth and rough components. The original attempt was to separate the major portion of the pore (pore body) from the pore wall roughness (Figure 21). The smooth component is that portion remaining before the last opening process which totally removes (erodes) the porel. In other words, the smooth component is represented by all the pixels which have the largest pore size measurement of a porel. The smooth porosity is usually, but not always, the area of the largest inscribed circle of a porel. The rough component is then classified as the remaining portion of the porosity of a porel.

The concept of smooth and rough porosity works well for a porel with only one significant major pore body such as the one shown in Figure 21. However, it loses its original meaning of distinguishing pore body and pore wall roughness when several pore bodies are interconnected. In a porel that has several significant pore bodies, only the largest one can be the smooth component. Thus, as a result of a smaller number of porels, the smooth component of a highly connected pore image is much smaller than the smooth component of a disconnected pore image. In this study, the ratio of the rough porosity to the total porosity is chosen as a connectivity indicator (Figure 22). This ratio is based on porosity measurements which are

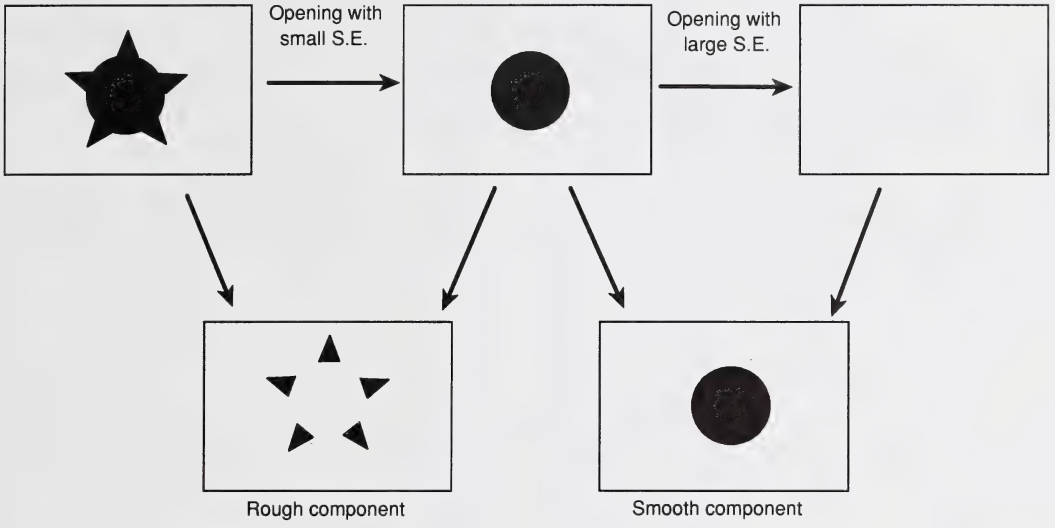

Figure 21. *Diagram of opening processes to remove the rough (pore wall roughness) and smooth components of a porel (modified from Ehrlich et al., 1984).*

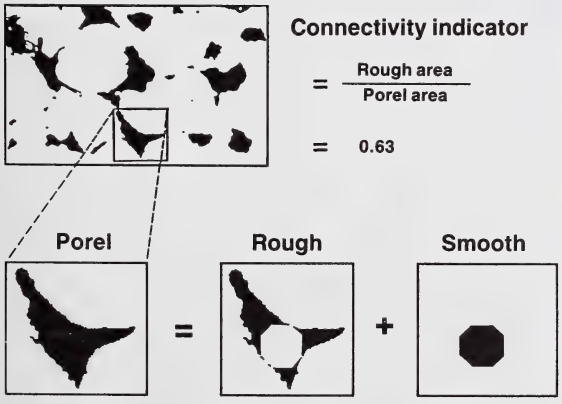

Figure 22. *Graphical representation of the connectivity indicator as the ratio of the rough component to the porel area. A porel (pore element) is a discrete unconnected patch of porosity. The smooth component is the portion with the largest size which resembles an inscribed circle of the porel. The remainder of the porel is the rough component*

less sensitive to certain noises, such as one pixel porels. The connectivity indicator varies between zero and one, providing an easy interpretation of its value.

Reservoir Pore Systems

Sampling and sample preparation. Twenty-two horizontal core plugs were taken from the blocky channel, transition zone and channel margin lithofacies, from six cored wells in the reservoir. The shale clast lithofacies is not suitable for plug sampling and is studied in a later section using different techniques. All samples were confined by either lead sleeves or teflon tubes prior to toluene vapour extraction of the heavy oil. Horizontal permeability under overburden pressure was measured on 19 samples. The samples were later impregnated with epoxy prior to thin sectioning. A fluorescent dye was mixed with the epoxy to facilitate the identification of pore/grain areas with a fluorescent microscope (Gies, 1987). Two petrographic thin sections, one vertical and one horizontal, were made from each plug.

In the PIA workstation, a video camera mounted on top of the microscope acquired and transmitted thin section images to a computer. An intensity threshold value was chosen in order to distinguish the bright pore areas from the dark mineral grains and to produce binary images. The generalized size analysis (Appendix A) was applied to each image to produce a size distribution, which was further divided into smooth and rough size distributions. Figure 23 shows four images and their corresponding smooth and rough size distributions. Sixteen images were digitized per thin section and all measurements were averaged for each thin section. The mean of the generalized size distribution was used as a single value for pore size, and the ratio of rough pore component to the total pore area was used as a connectivity indicator. The smooth and rough size distributions were then analyzed by an unmixing procedure (Full et al., 1984; Full et al., 1981) to represent each sample as being composed of a number of end members. This procedure identifies characteristic pore types in the pore systems. The main results of the unmixing procedure, including lithofacies from which the samples were collected, are listed in Table 1.

Three additional samples were later taken from locations adjacent to the samples number 17, 19, and 22, identified as typical samples for three different pore types. These three samples were sent to a service laboratory to measure their capillary pressure drainage curves and residual non-wetting phase saturations by an air-brine centrifuge method. These data were used to verify and improve the understanding of the relations between pore geometry and two-phase flow properties, and to help further the characterization of two-phase flow properties for each pore type.

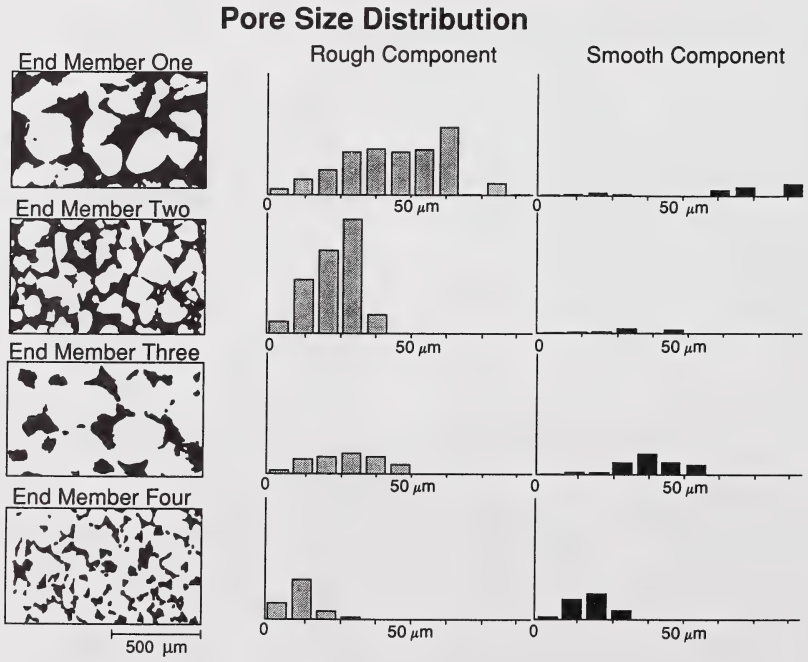

Figure 23. *Petrographic image analysis of representative end member pore images with their rough and smooth size distributions. The mean pore sizes (radius) of the four images are 45, 22, 31, and 13.5 microns; and the connectivity indicators are 0.90, 0.96, 0.59, and 0.53, respectively.*

Table 1. *Pore system analysis results. TRANS. indicates the transition zone between the blocky channel (BLOCKY) and channel margin (MARGIN) lithofacies sands; (W) represents water saturated sands; and EM1 to EM4 are the pore volume fractions of end members in each sample.*

Sample no.	Orient.	Facies	EM1	EM2	EM3	EM4	k_h (darcies)	Conn. ind.	Pore size (μm)
1	H	BLOCKY	0.19	0.57	0.17	0.06	12.1	0.83	30.4
	V		0.19	0.54	0.16	0.12		0.82	29.7
2	H	TRANS.	0.06	0.63	0.16	0.15	3.9	0.85	24.3
	V		0.05	0.44	0.14	0.37		0.78	21.2
3	H	MARGIN	0.02	0.55	0.12	0.31	2.9	0.84	20.3
	V		0.02	0.34	0.15	0.49		0.72	19.2
4	H	TRANS.	0.11	0.63	0.19	0.07	6.5	0.83	27.2
	V		0.05	0.54	0.20	0.21		0.77	24.3
5	H	BLOCKY	0.40	0.40	0.13	0.07	11.1	0.82	38.3
	V		0.31	0.41	0.22	0.06		0.74	36.5
6	H	BLOCKY(*W*)	0.20	0.45	0.26	0.09	5.8	0.71	33.1
	V		0.15	0.43	0.30	0.12		0.65	30.9
7	H	BLOCKY(*W*)	0.24	0.50	0.17	0.08	–	0.80	32.2
	V		0.05	0.43	0.32	0.20		0.63	26.3
8	H	BLOCKY	0.52	0.39	0.02	0.07	–	0.94	41.0
	V		0.34	0.43	0.18	0.06		0.79	36.7
9	H	MARGIN	0.16	0.59	0.14	0.11	–	0.85	28.1
	V		0.05	0.09	0.18	0.67		0.59	18.9
11	H	BLOCKY	0.29	0.57	0.14	0.00	11.9	0.88	33.4
	V		0.29	0.56	0.13	0.02		0.87	33.3
12	H	BLOCKY	0.18	0.57	0.18	0.07	9.2	0.81	30.4
	V		0.11	0.63	0.20	0.06		0.82	27.3
13	H	TRANS.	0.07	0.64	0.18	0.11	7.8	0.84	25.0
	V		0.03	0.62	0.20	0.16		0.81	23.5
14	H	BLOCKY	0.30	0.54	0.14	0.02	11.6	0.86	34.1
	V		0.27	0.54	0.14	0.04		0.85	32.5
15	H	TRANS.	0.11	0.51	0.20	0.19	7.9	0.76	26.2
	V		0.06	0.66	0.18	0.09		0.84	25.0
16	H	MARGIN	0.04	0.16	0.09	0.72	2.0	0.70	15.9
	V		0.03	0.31	0.11	0.55		0.74	17.6
17	H	TRANS.	0.02	0.27	0.13	0.57	3.5	0.71	18.0
	V		0.01	0.49	0.13	0.37		0.80	19.6
18	H	BLOCKY	0.08	0.57	0.21	0.14	8.8	0.79	25.7
	V		0.12	0.67	0.19	0.03		0.85	28.1
19	H	BLOCKY	0.09	0.61	0.22	0.09	7.9	0.79	26.8
	V		0.10	0.62	0.18	0.11		0.83	25.9
20	H	BLOCKY	0.14	0.50	0.17	0.19	8.0	0.80	27.1
	V		0.23	0.43	0.17	0.17		0.77	31.0
21	H	BLOCKY	0.32	0.53	0.14	0.01	11.6	0.86	35.1
	V		0.45	0.40	0.10	0.05		0.84	39.2
22	H	BLOCKY(*W*)	0.18	0.41	0.33	0.08	2.1	0.62	34.0
	V		0.14	0.44	0.37	0.05		0.61	32.3
23	H	BLOCKY(*W*)	0.15	0.42	0.34	0.10	4.1	0.62	31.8
	V		0.14	0.47	0.30	0.09		0.67	31.1

Permeability and pore geometry. A quantitative relationship between measured permeability values and image data can be established by regression analysis. If the relationship is statistically significant, it can be used to predict the permeability for samples from the reservoir for which no permeability measurements are available. Based on dimensional analysis, with permeability having a dimension of length squared and the connectivity indicator being dimensionless, the regression relation is chosen such that the permeability is a quadratic function of the pore size and a linear function of the connectivity indicator. Multivariable regression is used to consider both factors simultaneously. In this study, horizontal permeability values were correlated separately for horizontal thin section measurements and vertical thin section measurements. The resulting equations are:

$$(1)\quad k_h = 0.00647\, p^2 + 32.2\, c - 23.0$$

with a correlation coefficient of $R^2 = 0.86$ for vertical thin section data, and

$$(2)\quad k_h = 0.00566\, p^2 + 27.1\, c - 18.7$$

with a correlation coefficient of $R^2 = 0.72$ for horizontal thin section data.

In both equations, k_h is horizontal permeability in darcies, p is pore size in micrometres, and c is the connectivity indicator. Both pore size and connectivity indicator are highly significant at a 1% level of confidence interval in both equations. Figure 24 shows the data points and the regression surfaces for the two relations.

Vertical thin sections of horizontal core plugs provide a better pore geometry–permeability relationship than do the horizontal thin sections. This is probably the result of horizontal laminae, which are better sampled by a vertical thin section. A horizontal thin section may cut through only one or possibly a few of the many laminae in a one-inch diameter horizontal plug, whereas the vertical thin section cuts through all the laminae.

Pore type and lithofacies. An unmixing procedure (Full et al., 1984; Full et al., 1981) was used to analyze the pore data of the Provost Upper Mannville B Pool reservoir. This procedure includes a Q-mode factor analysis with an iterative process to represent each sample as composed of several end members. The number of end members is chosen in such a way that most of the variance of the size distributions can be explained. The end members are derived by an iterative procedure in order to minimize the negative values in their size distributions (Figure 23) and the negatives in the end member compositions for the samples (Table 1). The results significantly simplify the large amount of size distribution data and make it easier to interpret.

Four end members were identified using this unmixing procedure. The pore images in Figure 23 present the closest real images of these four hypothetical end members. In general, end member one represents large, highly connected pores; end member two represents medium size and highly connected pores; end member three is comprised of medium-large sized but poorly connected pores; and end member four represents small, poorly connected pores. Poor 2D connectivity can be caused by two 3D factors. The first is the coordination number, which is the number of neighboring pores connected to a centre pore, i.e., the number of connected throats per pore. The second is the throat size. Both decreasing of the coordination number and lowering the throat size can produce a less connected 2D image.

Table 1 lists the fractional amounts of each end member in each sample. These end member compositions can be plotted within a tetrahedron (Figure 25) to show clearly the relation between end-member pore types and lithofacies. From Table 1 and Figure 25, it follows that end member one is present in significant amounts in the blocky channel oil saturated sands; end member two exists in most samples, particularly in large amounts in the transition zone; end member three is closely associated with the blocky channel water saturated sands; and end member four is a typical component of the channel margin sands. In general, a trend of decreasing pore size, from end member one through end member two, to end member four, is closely related to the fining upward sequence, commonly found in a channel deposit. The water saturated blocky channel sands were more affected by diagenetic processes; therefore, a poorly connected pore network was formed as a result of the significant amount of diagenetic clays. Figure 26 summarizes the general relation between the characteristic pore system end members and the reservoir lithofacies.

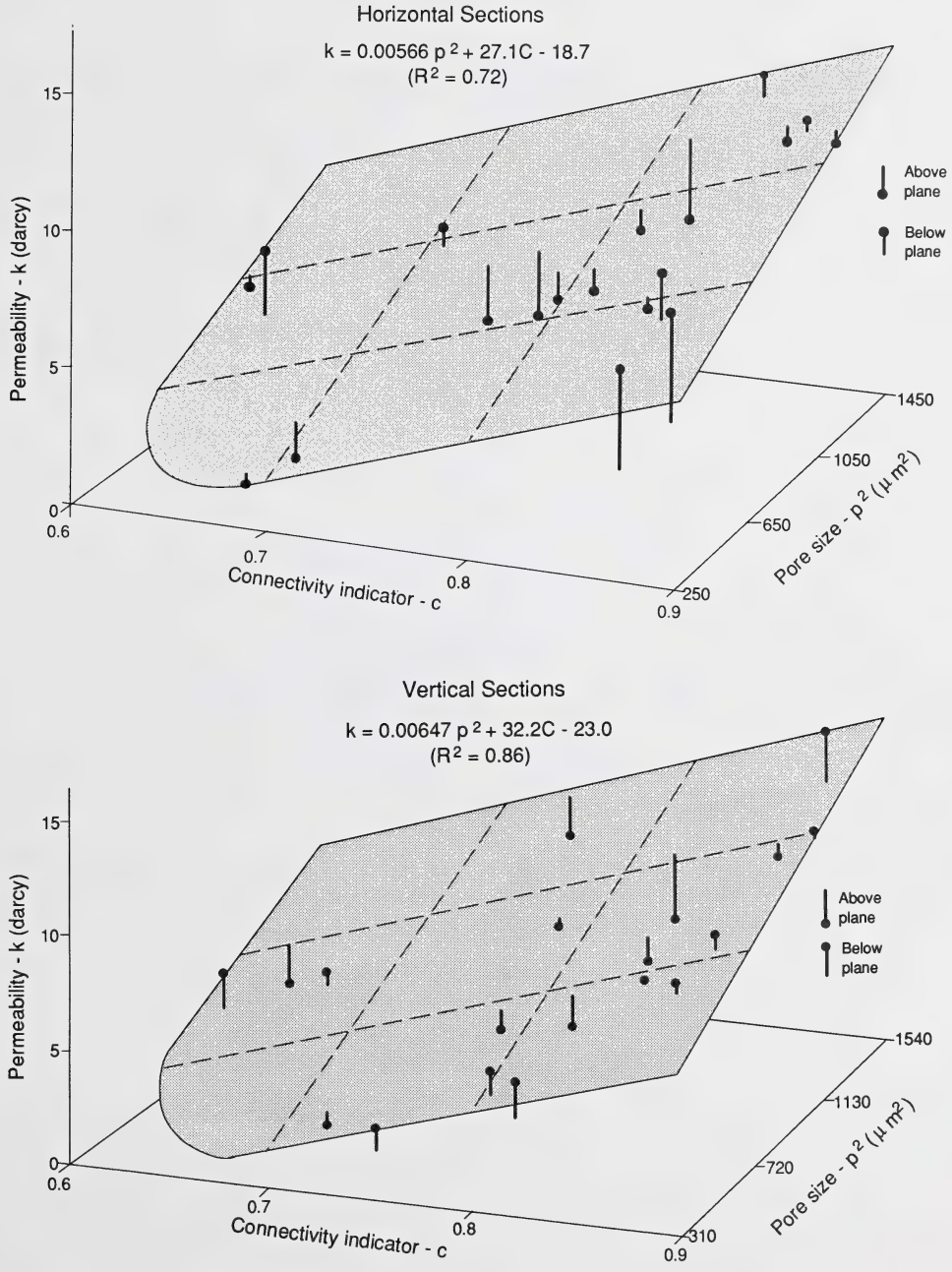

Figure 24. *Regression surfaces between permeability and the square of pore size and connectivity. Solid circles are the data projected on the surfaces (predictions) and vertical lines indicate the distances between data points and their projections.*

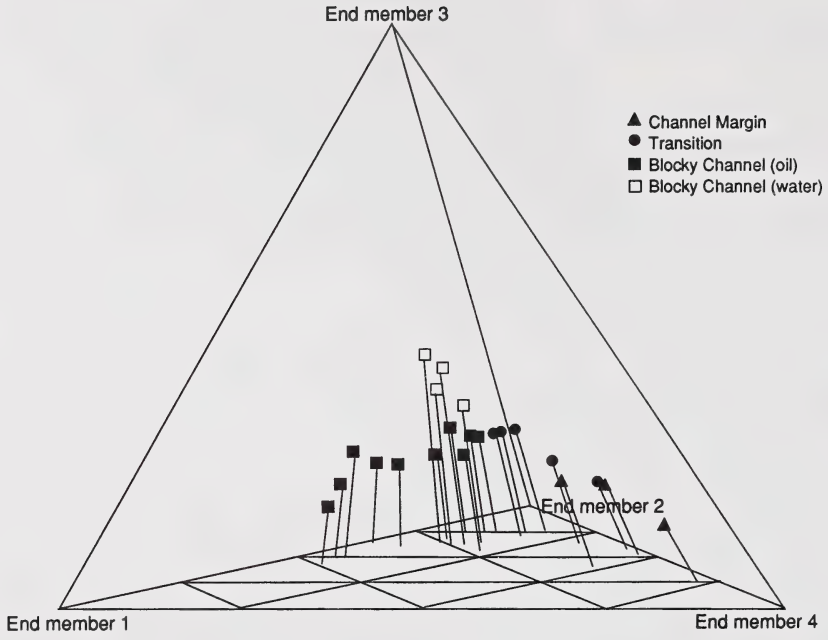

Figure 25. *Quaternary plot of sample compositions and their lithofacies origin. Values from vertical and horizontal thin sections were averaged and then plotted for each sample.*

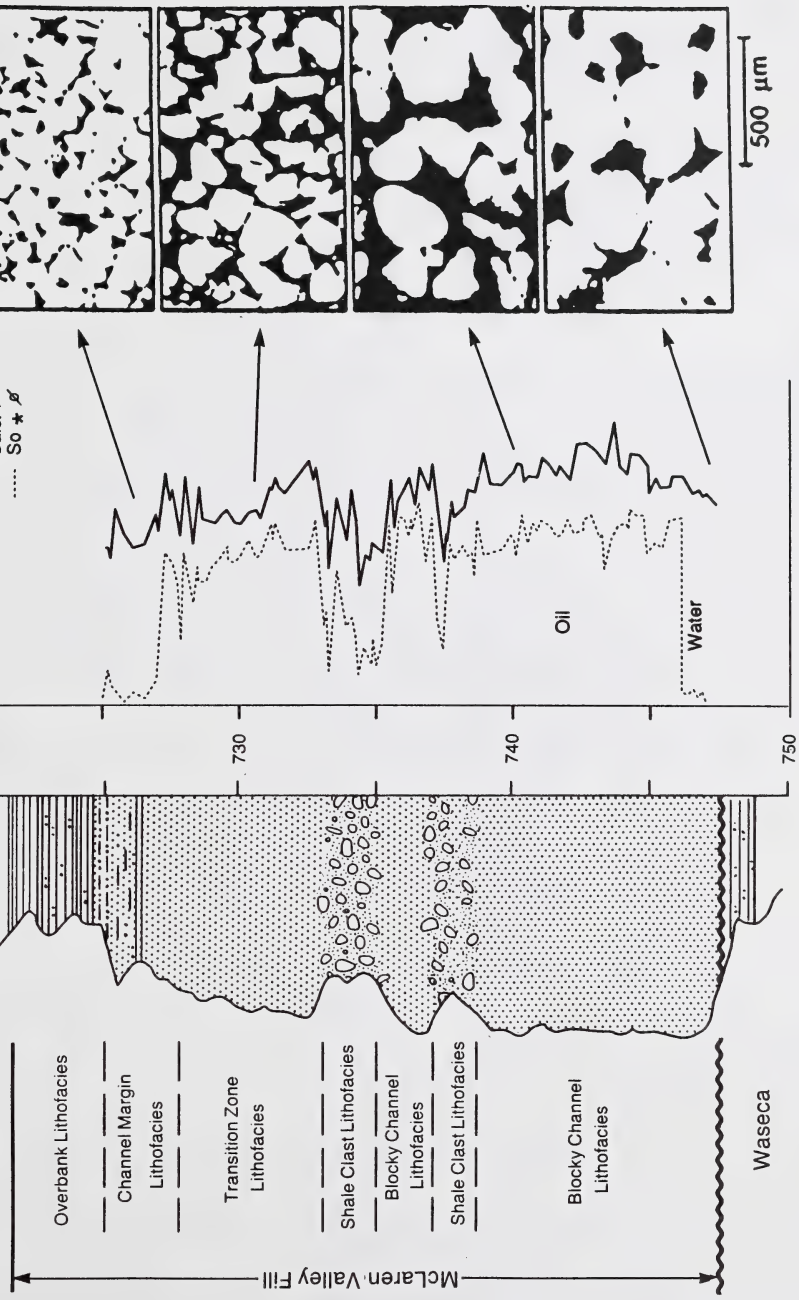

Figure 26. *Reservoir lithofacies and their characteristic pore end members.*

Capillarity and pore type. The laboratory results of capillary pressure and residual saturation measurements on three selected samples are shown in Figure 27. Permeability was measured as part of the special core analysis and values are relatively high compared to values from other samples (Table 1). This is probably because permeability for the three selected samples was measured without overburden pressure.

The horizontal part of the capillary curve, the so called "entrance," "entry," "breakthrough," or "bubbling" pressure, is a measure of the critical throat size. All throats greater than this size can form a continuous network through the sample. This size is also the most important factor in determining permeability (Macmullin and Muccini, 1956). Therefore, it is not surprising to find that the oil saturated blocky channel sample, with large connected pores, has the lowest entrance pressure, largest critical throat size, and highest permeability. The transition zone sample, with small connected pores, has the highest entrance pressure, smallest critical throat size, and lowest permeability. The sample from water zone, which has medium and less connected pores, has a medium permeability and entrance pressure, therefore, a medium critical throat size amongst the three samples.

The irreducible water saturation, the vertical portion of the capillary curve, is a strong function of grain surface area which the wetting phase (water in this case) contacts. The grain surface area is highly related to the clay content of the sample. Figure 27 shows that the sample from the oil-saturated blocky channel sand has the lowest irreducible water saturation, while the water-saturated blocky channel sand sample has the highest irreducible water saturation. In general, the clay content is associated with a decrease in the sand grain size and this is probably true for the two samples from the oil saturated zone. Although the water zone sample has large sand grains, it contains a large amount of clay, as a result of diagenesis, and this probably accounts for its high irreducible water saturation.

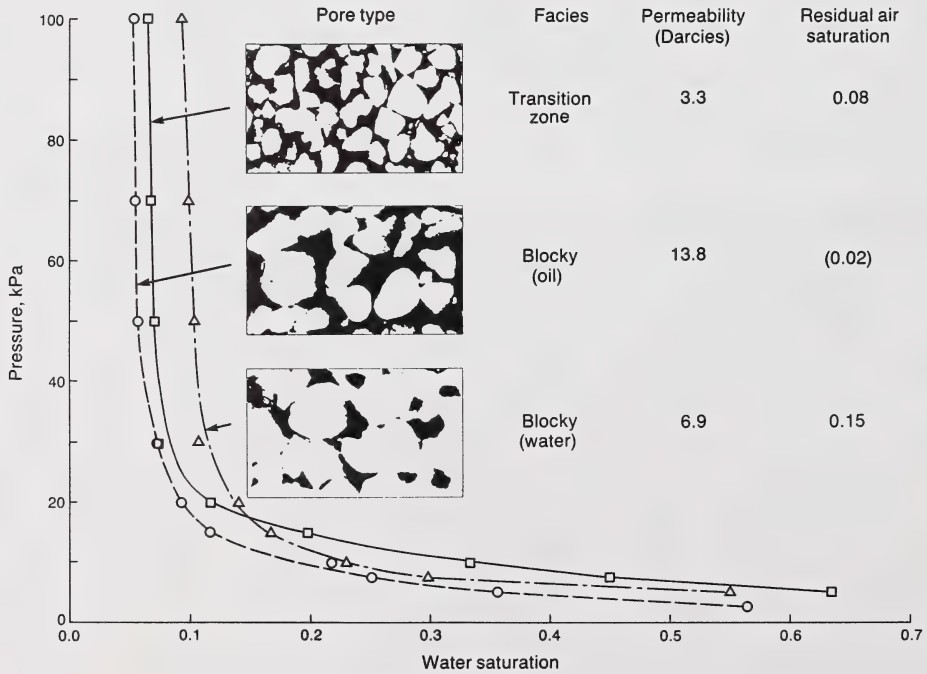

Figure 27. *Capillary pressure and residual saturation analysis results for three selected samples, representing three pore types in the reservoir.*

The residual non-wetting phase saturation (air in this experiment) at the pore scale is highly affected by the throat size, aspect ratio (pore-throat size ratio), and coordination number (Li and Wardlaw, 1986a, 1986b; Kirkpatrick, 1973). Generally, the smaller the throat size and the higher the aspect ratio (i.e., larger pores and smaller throats), the higher the residual air saturation. A decreasing coordination number also results in a higher residual air saturation.

The laboratory experiment was performed by submerging the sample at its irreducible water saturation in brine and then applying centrifuge force to drive the air out of the sample. The blocky channel oil saturated sand sample was saturated with brine (S_{air} = 0.02) immediately after submergence without applying any extra pressure or force. Possible causes are that throats are so large that snap off (Li and Wardlaw, 1986b) rarely occurs; pores are so well connected that dead end pores are almost non-existent; and the sample may not be in a perfectly water wet condition. The transition zone sample, by comparison, has smaller pores and throats; thus, a higher residual air saturation is expected and observed. The residual air saturation is 0.081 under 100 kPa. However, when comparing the transition zone sample to the sample from the water zone, the water zone sample has larger and two-dimensionally less connected pores. Larger pores may result in a higher aspect ratio, while 2D less connected pores can be the result of smaller 3D average throat size and/or coordination number. In any case, a higher residual air saturation is expected and verified by the experimental result which is equal to 0.153 under 100 kPa.

Due to the high viscosity of heavy oil and bitumen, experiments with reservoir fluids are very difficult. In this study, air was used as the non-wetting phase. This not only simulates qualitatively the heavy oil, but even simulates better the steam phase in a steam injection operation. The results clearly indicate a close relationship between pore systems and two-phase flow properties such as capillary pressure curves and residual non-wetting phase saturation. Although the measurement was performed only on three samples, these conclusions may be extended to the three lithofacies associated with these three pore types, because of the previously established relation between lithofacies and pore types.

The flow properties of the channel margin sands can also be estimated qualitatively. According to the pore systems, clay content, and permeability trends, the channel margin sands with small pore size and high clay content are expected to have a lower permeability, higher entry pressure, higher irreducible water saturation, and higher residual air saturation than the underlying transition zone sands.

Quantitative relations between pore characteristics and flow properties may be established with a larger number of samples. Such relations can then be used to predict flow properties directly from pore image observations.

Pore Scale Characterization Discussion

This study has shown that petrographic image analysis (PIA) can effectively obtain pore size and connectivity information, which can be related quantitatively to permeability and qualitatively to capillary pressure and residual saturation. The quantitative relation can be used to estimate permeability values where no measurements are available. With more samples, quantitative relations between pore geometry measurements and capillary pressure and residual saturation may be established and used for an accurate estimation of these properties. Other flow properties, such as relative permeability and foam flow properties, which are controlled by both pore geometry and rock–fluid interactions (e.g., wettability), have the potential to be estimated for specific mineralogy and fluid saturations. PIA can help in the estimation or quantification of those flow properties which are affected by pore geometry.

The relations between pore geometry and flow properties varies from reservoir to reservoir or from formation to formation. For example, a PIA study was performed on samples from the AOSTRA Underground Test Facility Site. Permeability was found to be significantly correlated only with pore size (Reservoir Analysis Project, 1990). This is probably because the connectivity indicator in that reservoir varies in a smaller range and is correlated with pore size. Therefore, pore connectivity is not a significant factor in the regression equation for the permeability of sands at the AOSTRA UTF site.

Sample preparation and imaging techniques can be improved in future studies. In this study, the resolution of the imaging technique was limited by the thickness of the thin section, approximate 30 micrometres. Pore features less than 15 micrometres were thus difficult to identify. This may not be important for highly permeable oil sands samples, but it is crucial for consolidated reservoir rocks, which usually have throat sizes of one micrometre or less. Scanning Electron Microscopy (Dilks and Graham, 1985) or surface staining techniques (Ruzyla and Jezek, 1987) can be used on polished sample surfaces to obtain high resolution pore images.

In conclusion, petrographic image analysis techniques can quantify pore geometry and establish relations between lithofacies, pore systems, and flow properties. These relations improve the understanding of how geological processes control the development of pore systems and affect the flow properties of reservoir rocks. They may be used to estimate flow properties for quantitative reservoir characterization.

SANDY FACIES CHARACTERIZATION

There exists a large amount of petrophysical data measured from core for the sandy facies (blocky channel, transition zone, and channel margin sands) of the Provost Upper Mannville B Pool. The data consist of interval measurements of fluid saturations and porosity, and discrete point (plug) measurements of permeability. However, these data are not at the proper scale for characterizing the reservoir flow units or grid blocks. The data need to be scaled up from core measurements to the flow unit scale for input into the numerical reservoir models used to simulate recovery processes.

Most of the wells in the Provost Upper Mannville B Pool show a definite pattern of permeability variation with depth, in which permeability is relatively constant in the main portion of the reservoir (the blocky channel lithofacies), then decreases towards the top of the reservoir through the transition zone and the channel margin lithofacies. This variability is most clearly seen in the currently active steam pilot area in Sec. 20, Twp. 37, Rge. 1W4 (Figure 28). Not shown in Figure 28, because these wells do not have a water leg, is a lower permeability in the water-saturated blocky channel sands than in the overlying oil-saturated blocky channel sands. This overall trend, of decreasing permeability toward the upper portions of the reservoir and lower permeability in the water-saturated sands, is what one would expect based on the geological nature of the reservoir. The water-saturated sands have undergone more diagenesis and as a result have a higher clay content and a lower permeability than the oil-saturated sands. The blocky channel sands are transitional with the channel margin sands, hence the gradual decrease in permeability from the blocky channel sand to the much less permeable channel margin sands. These trends are also observed in the reservoir pore systems, as discussed in the previous chapter. The oil-saturated blocky channel sands have a large, open pore network. The water-saturated sands have large, less connected pores. In the transition zone between the blocky channel sands to the channel margin sands, the grain size slowly decreases and the pores become smaller but still have a high degree of connectedness. Near the top of the reservoir, in the channel margin sands, there is a higher clay content and smaller grain size, as a consequence of lower energy conditions in the depositional environment. As a result, the pores are smaller and poorly connected, and permeability values are the lowest. The overall fining-upward cycle inherited from the depositional environment is the controlling factor in the permeability trend within the reservoir, except for the diagenetic overprint in the water-saturated sands.

Permeability values vary widely throughout the reservoir, both areally and vertically. These variations are the result of actual permeability variations in the reservoir, variability in core quality when the core (consisting of unconsolidated oil-saturated sand) arrives at the laboratory, and inter-laboratory differences in measurements resulting from different equipment or techniques. This last type of variability was discussed in a previous report (Reservoir Analysis Project, 1989, p. 5–8), where it was noted that equipment differences between two laboratories resulted in different permeability values being reported for the same samples. Permeability variations within the same core from any well are probably not subject to core quality or laboratory variations. Thus, permeability versus depth trends for individual cored wells are real.

Scaling Up From Core to Flow Unit

The scaling up of core analysis measurements from individual wells to a characteristic value for flow units or grid blocks at the reservoir scale requires a sequential process (Cushman, 1984). Data density is different in the vertical than in the horizontal direction, i.e., plug measurements are centimetres apart in the same well, but tens to hundreds of metres between wells. Thus, the first step is to scale up the core analysis measurements to flow units on a well-by-well basis. The next step is to scale up these values to flow unit values at the reservoir scale.

The subdivision of the reservoir into flow units and quantification of permeability for these units on a local or well basis is presented in Figure 29 for the

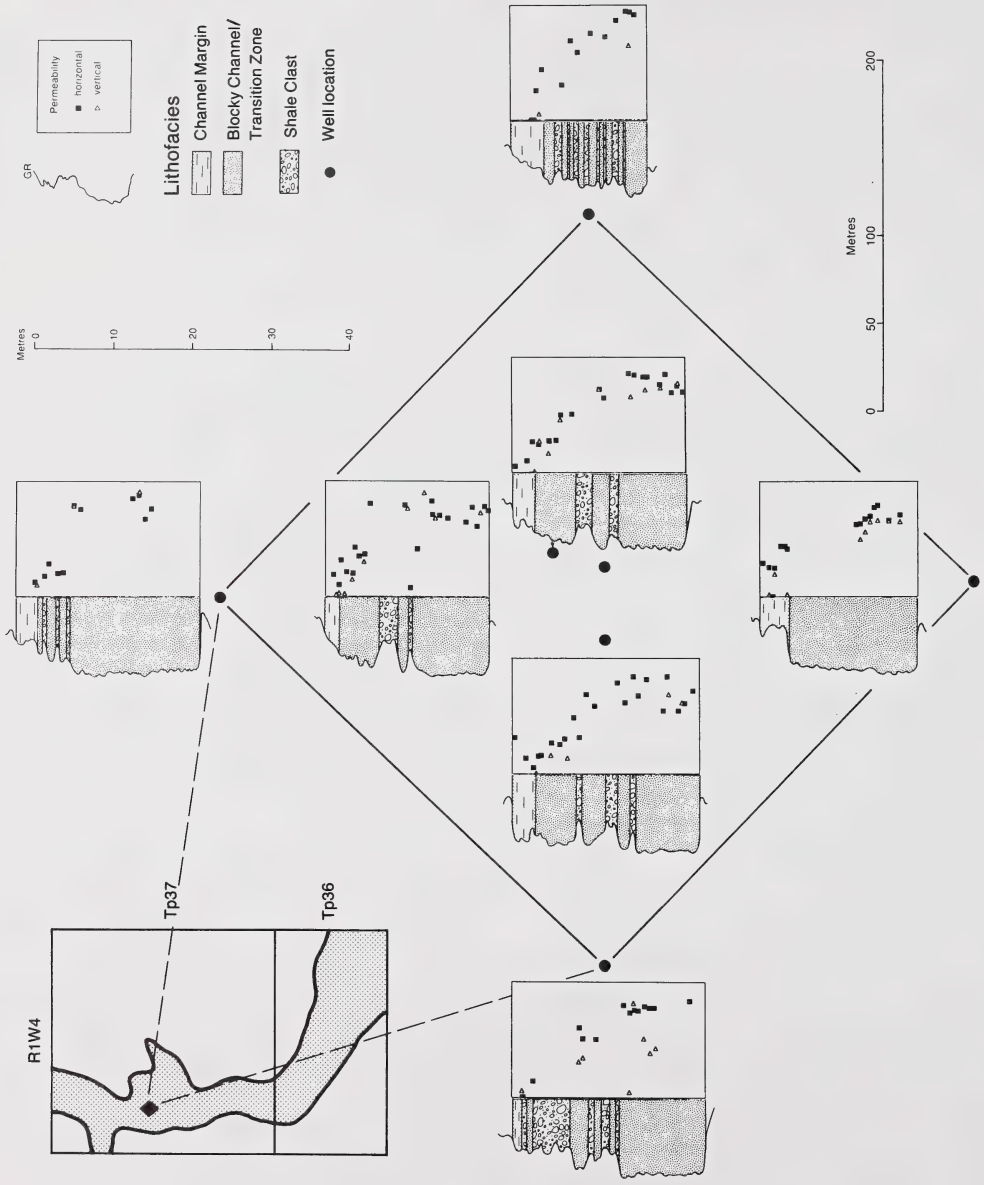

Figure 28. *Permeability trends for wells from the steam pilot in the Provost Upper Mannville B Pool.*

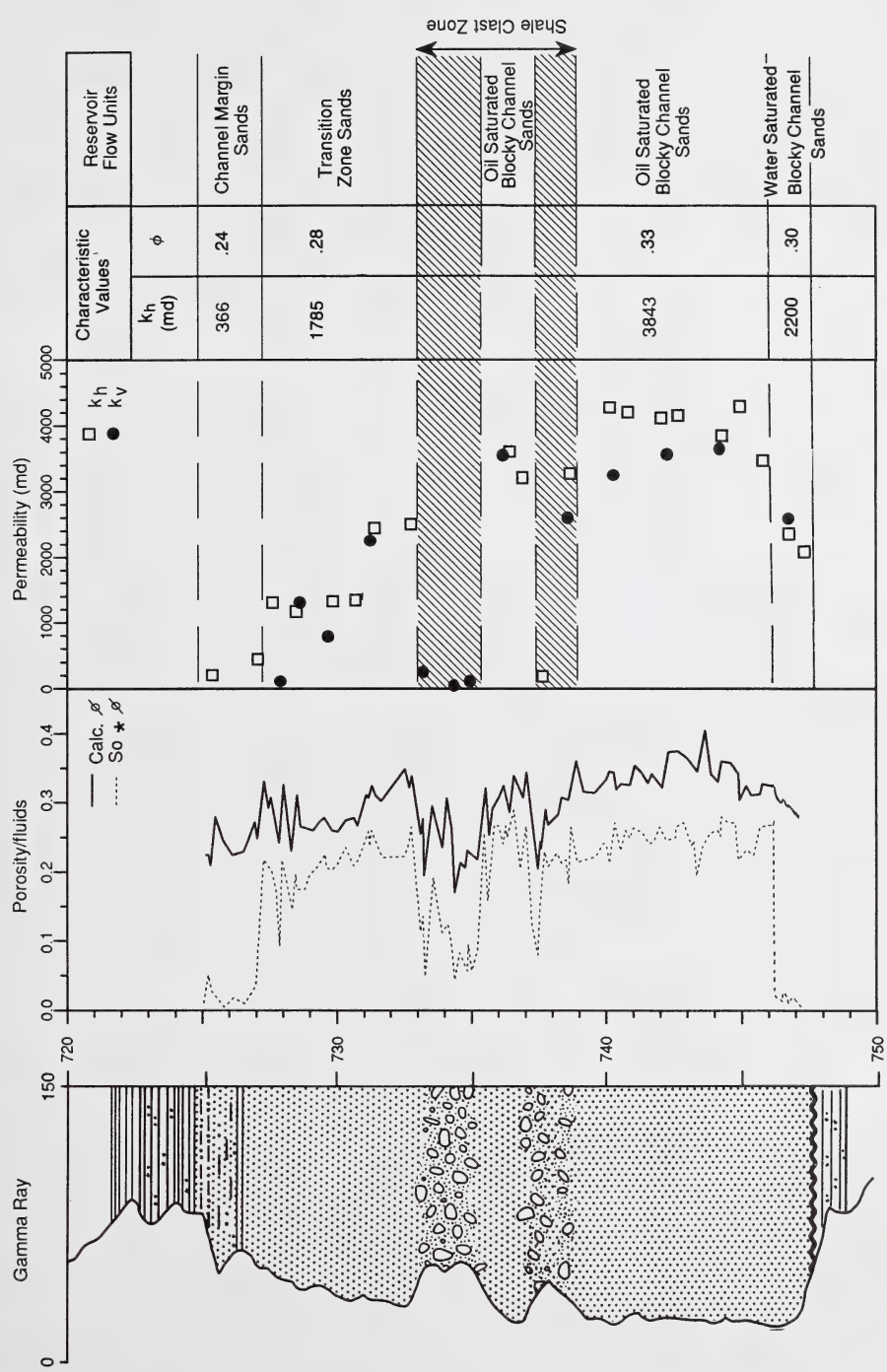

Figure 29. *Sandy facies flow units and their characteristic horizontal permeability and porosity values for a composite example well.*

central well (5A-20-37-1W4, I-23) in the steam pilot pattern. For illustrative purposes, a thin water leg has been added to this well to show the effect of the water saturated blocky channel sands. Based on lithology, fluid saturations, porosity and permeability measurements, and supported by the pore system analysis, the sandy portion of the reservoir has been divided into four flow units, shown in the right hand column. In ascending order, these flow units are: the water-saturated blocky channel sands, the oil-saturated blocky channel sands, the transition zone sands, and the channel margin sands. Permeability values in the blocky channel and channel margin flow units, respectively, vary within a relatively narrow range and show no significant variation with depth. The permeability values in the transition zone flow unit exhibit a gradual decrease from the blocky channel to the channel margin sands (Figure 29).

The scaling up of core measurements to the flow unit scale was discussed by Weber and van Geuns (1989), and their methodology has been adopted in this study. For the blocky channel flow units, the effective permeability values for individual wells were calculated as the geometric average of the individual core plug values. Calculation of the well effective permeability values for the transition zone flow unit took the almost linear trend in permeability variation into account, by calculating the average of this trend. For the channel margin flow unit, the effective horizontal permeability was calculated as the arithmetic average of the core plug values, because of its interbedded sand and shale character. The characteristic porosity for each flow unit on a per-well basis was calculated as the weighted arithmetic average of the individual interval measurements. For the composite example well, the results of these calculations are presented in Figure 29, which shows the characteristic value of k_h and ϕ for the four sandy facies flow units.

The same calculations were performed for all the cored wells in Sections 17 and 20, Twp. 37, Rge. 1W4, with the results given in Table 2. Only the wells in these two sections were used because of core quality considerations, and because the well density (hundreds of metres apart) in this small area (approx. 800 m by 2400 m) is significantly higher than for the other parts of the reservoir, where the well density is one order of magnitude less. Some of the wells in Table 2 have more than one listing for a specific flow unit. This is the result of the interbedded nature of the flow units found in the specific well. For example, for the well AA-05-20-37-1W4 (0B1), the sequence of flow units from the top to the bottom of the reservoir is CM (channel margin sands), TRS (transition zone sands), SCL (shale clast layer), BCO (oil saturated blocky channel sands), SCL, BCO to the base of the reservoir. This indicates that a shale clast layer occurs within the oil saturated blocky channel sands flow unit. The effective horizontal permeability value (k_h) was calculated for the gross BCO interval. However, the effective porosity (ϕ) was calculated for each individual interval because the data base for porosity measurements is so much larger.

Scaling Up to the Reservoir Scale

Effective permeability and porosity values at the well scale represent local conditions, whereas the reservoir represents a larger scale. For reservoir or regional scale simulations there is a need to scale up these well-scale values. While these simulations are seldom performed in reservoir engineering, they are commonly used in hydrogeology and basin analysis. Because this study is concerned with the development of reservoir characterization techniques, this step was undertaken and is presented here. The average thickness of the flow units is of the order of 10 m or less, while their areal extent is of the order of 10^2–10^3 m. Thus, for the next scaling up step (well to reservoir), it is appropriate to use the "shallow water" approximation by which hydraulic conductivity (K) (directly related to permeability, $K = k\rho g/\mu$) is averaged over the thickness of the flow unit and becomes transmissivity (T) (Dagan, 1989). Transmissivity, which is the product of hydraulic conductivity and interval thickness, was determined for individual intervals in each well. In scaling up to the reservoir scale, the individual interval effective properties are combined for the entire flow unit. Transmissivity then becomes a point value in a horizontal system of coordinates. Transmissivity values were calculated for each flow unit at every cored well in Sections 17 and 20, Twp. 37, Rge. 1W4. The number of wells with data are 15, 18, 21, and 2 for the channel margin, transition zone, oil-saturated blocky channel, and water-saturated blocky channel flow units, respectively.

There is no apparent trend in the areal distribution of transmissivity values for each flow unit and the values are lognormally distributed.

Table 2. *Well by well characteristic values for horizontal permeability (k_h), porosity (ϕ), hydraulic conductivity (K), and transmissivity (T) for sandy flow units in the northern portion of the Provost Upper Mannville B Pool (CM, channel margin sands; TRS, transition zone sands; BCO, oil saturated blocky channel sands; BCW, water saturated blocky channel sands; SCL, shale clast layer; BOT, bottom of reservoir).*

Well location	Flow unit	Depth (m)	Thickness (m)	Characteristic value			
				k_h (md)	ϕ	K (m/sec)	T (m/sec)
AA/05-17-037-1W4 (I-9)	CM	731.50	1.18	374	0.313	0.362E-05	0.427E-05
	TRC	732.68	2.68	1488	0.339	0.144E-04	0.386E-04
	BCO	735.36	16.55	2607	0.368	0.253E-04	0.418E-03
	BOT	751.91					
AA/06-17-037-1W4 (K9-C1)	CM	731.50	2.89	229	0.286	0.119E-05	0.345E-05
	TRS	734.39	2.68	1933	0.354	0.187E-04	0.502E-04
	BCO	737.07	9.93	3222	0.368	0.312E-04	0.310E-03
	BOT	747.00					
AF/06C-17-037-1W4 (K9A)	CM	731.50	0.53	451	0.281	0.437E-05	0.231E-05
	TRS	732.03	2.50	1422	0.266	0.138E-04	0.344E-04
	BCO	734.53	13.20	3952	0.345	0.383E-04	0.505E-03
	BOT	747.73					
AH/11C-17-037-1W4 (J-12)	CM	733.60	5.84	372	0.275	0.187E-05	0.109E-04
	TRS	739.44	2.38	3853	0.351	0.373E-04	0.888E-04
	BCO	741.82	12.56	8088	0.335	0.783E-04	0.984E-03
	BCW	754.38	2.74	2261	0.314	0.219E-04	0.600E-04
	BOT	757.12					
AL/11C-17-037-1W4 (0B5)	CM	733.20	2.76	1298	0.276	0.126E-04	0.347E-04
	TRS	735.96	3.69	1425	0.313	0.138E-04	0.509E-04
	BCO	739.65	9.85	2172	0.325	0.210E-04	0.207E-03
	BOT	749.50					
AK/11D-17-037-1W4 (M-13)	CM	728.10	2.26	973	0.240	0.942E-05	0.213E-04
	TRS	730.36	3.47	1746	0.304	0.169E-04	0.5867-04
	BCO	733.83	12.86	2764	0.317	0.268E-04	0.344E-03
	BOT	746.69					
AM/11D-17-037-1W4 (0B6)	CM	729.45	1.59	648	0.316	0.626E-05	0.996E-05
	TRS	731.04	2.92	1068	0.293	0.103E-04	0.302E-04
	BCO	733.96	13.54	1897	0.344	0.184E-04	0.242E-03
	BOT	747.50					
AA/13-17-037-1W4 (I-15)	CM	733.40	3.53		0.265		
	TRS	736.93	3.07	2075	0.312	0.201E-04	0.617E-04
	BCO	740.00	14.00	2573	0.359	0.249E-04	0.349E-C3
	BOT	754.00					
AA/14B-17-037-1W4 (K-15)	CM	728.39	3.19	100	0.280	0.968E-06	0.309E-05
	TRS	731.58	2.47	1877	0.329	0.182E-04	0.449E-04
	BCO	734.05	14.45	3197	0.349	0.310E-04	0.447E-03
	BCW	748.50	1.90	564	0.178	0.546E-05	0.104E-04
	BOT	750.40					
AE/14-17-037-1W4 (K-17)	CM	729.71	2.79	362	0.231	0.351E-05	0.978E-05
	TRS	732.50	2.66	2113	0.310	0.205E-04	0.544E-04
	BCO	735.16	13.84	3482	0.323	0.337E-04	0.467E-03
	BOT	749.00					

Table 2. *Cont'd.....*

Well location	Flow unit	Depth (m)	Thickness (m)	Characteristic value			
				k_h (md)	ϕ	K (m/sec)	T (m/sec)
02/04D-20-037-1W4 (I-21)	CM	726.80	1.40	908	0.255	0.279E-05	0.391E-05
	TRS	728.20	2.21	1927	0.288	0.187E-04	0.412E-04
	BCO	730.41	16.59	3477	0.330	0.337E-04	0.559E-03
	BOT	747.00					
AA/05-20-037-1W4 (0B1)	CM	727.85	1.92	700	0.249	0.611E-05	0.117E-04
	TRS	729.77	74.07	1803	0.323	0.175E-04	0.711E-04
	SCL	733.84	3.50				
	BCO	737.34	40.80	2401	0.312	0.232E-04	0.186E-04
	SCL	738.14	40.89				
	BCO	739.03	9.87	2401	0.321	0.232E-04	0.229E-03
	BOT	748.90					
AB/05-20-037-1W4 (0B2)	CM	724.20	3.01	813	0.216	0.676E-05	0.204E-04
	TRS	727.21	4.20	1198	0.274	0.116E-04	0.487E-04
	SCL	732.41	0.65				
	TRS	732.06	0.11	2224	0.305	0.215E-04	0.237E-05
	BCO	732.17	2.19	3400	0.284	0.329E-04	0.721E-04
	SCL	734.36	2.10				
	BCO	736.46	2.01	3400	0.287	0.329E-04	0.662E-04
	SCL	738.47	0.61				
	BCO	739.08	8.49	3400	0.325	0.329E-04	0.280E-03
	BOT	747.57					
AC/05-20-037-1W4 (H22)	CM	722.50	1.80				
	TRS	724.30	1.70				
	BCO	726.00	1.00				
	SCL	727.00	1.50				
	BCO	728.50	1.55				
	SCL	730.05	5.45				
	BCO	735.50	1.00				
	SCL	736.50	2.50				
	BCO	739.00	6.00	3462	0.393	0.335E-04	0.201E-03
	BCW	745.00	0.08		0.208		
	BOT	745.08					
00/05C-20-037-1W4	CM	722.50	2.46	1338	0.220	0.111E-04	0.273E-04
	TRS	724.96	5.10	5306	0.324	0.514E-04	0.262E-03
	BCO	730.06	19.14	6036	0.343	0.584E-04	0.112E-02
	BCW	749.20	7.60				
	BOT	756.80					
03/05-20-037-1W4 (I-25)	CM	721.25	3.88	615	0.219	0.596E-05	0.231E-04
	TRS	725.13	1.03	1067	0.256	0.103E-04	0.106E-04
	SCL	726.16	0.65				
	TRS	726.81	0.46	1067	0.296	0.103E-04	0.475E-05
	SCL	727.27	0.19				
	TRS	727.46	0.26	1067	0.308	0.103E-04	0.269E-05
	SCL	727.72	0.61				
	BCO	728.33	18.58	3925	0.318	0.380E-04	0.706E-03
	BOT	746.91					

Table 2. *Cont'd.....*

Well location	Flow unit	Depth (m)	Thickness (m)	Characteristic value			
				k_h (md)	ϕ	K (m/sec)	T (m/sec)
04/05B-20-037-1W4 (G-23)	CM	723.24	2.74		0.237		
	TRS	725.98	0.56	766	0.234	0.742E-05	0.415E-05
	SCL	726.54	0.86				
	TRS	727.40	0.24	1057	0.310	0.102E-04	0.246E-05
	SCL	727.64	5.26				
	TRS	732.90	1.67	2493	0.306	0.241E-04	0.403E-04
	SCL	734.57	0.85				
	TRS	735.42	0.30	2917	0.288	0.282E-04	0.847E-05
	SCL	735.72	3.02				
	BCO	738.74	9.80	4102	0.351	0.397E-04	0.389E-03
	BOT	748.54					
05/05A-20-037-1W4 (I-23)	CM	723.85	2.86	366	0.239	0.354E-05	0.101E-04
	TRS	726.71	5.89	1159	0.284	0.112E-04	0.661E-04
	SCL	732.60	2.61				
	BCO	735.21	1.49	3843	0.311	0.372E-04	0.555E-04
	SCL	736.70	0.51				
	BCO	737.21	0.43	3843	0.271	0.372E-04	0.160E-04
	SCL	737.64	0.77				
	BCO	738.41	8.49	3843	0.332	0.372E-04	0.316E-03
	BOT	746.90					
AB/06-20-037-1W4 (J-24)	CM	720.00	1.50				
	TRS	721.50	3.50				
	BCO	725.00	2.50				
	SCL	727.50	2.30				
	BCO	729.80	2.50				
	SCL	732.30	1.20				
	BCO	733.50	4.97	3765	0.369	0.365E-04	0.181E-03
	SCL	738.47	0.30				
	BCO	738.77	6.23	3765	0.344	0.365E-04	0.227E-03
	BOT	745.00					
02/06-20-037-1W4 (K-23)	CM	726.80	2.95		0.187		
	TRS	729.75	1.45	1854	0.272	0.180E-04	0.260E-04
	SCL	731.20	2.05				
	TRS	733.25	0.25	1854	0.270	0.180E-04	0.449E-05
	SCL	733.50	0.50				
	BCO	734.00	0.60	4375	0.284	0.424E-04	0.254E-04
	SCL	734.60	0.31				
	BCO	734.91	0.46	4375	0.327	0 424E-04	0.195E-C4
	SCL	735.37	0.30				
	BCO	735.67	0.74	4375	0.317	0.424E-04	0.314E-04
	SCL	736.41	0.59				
	BCO	737.00	0.75	4375	0.340	0.424E-04	0.318E-04
	SCL	737.75	0.66				
	BCO	738.41	0.59	4375	0.309	0.424E-04	0.250E-04
	SCL	739.00	1.00				
	BCO	740.00	0.53	4375	0.324	0.424E-04	0.225E-04
	SCL	740.53	0.56				
	BCO	741.09	2.91	4375	0.357	0.424E-04	0.123E-03
	BOT	744.00					

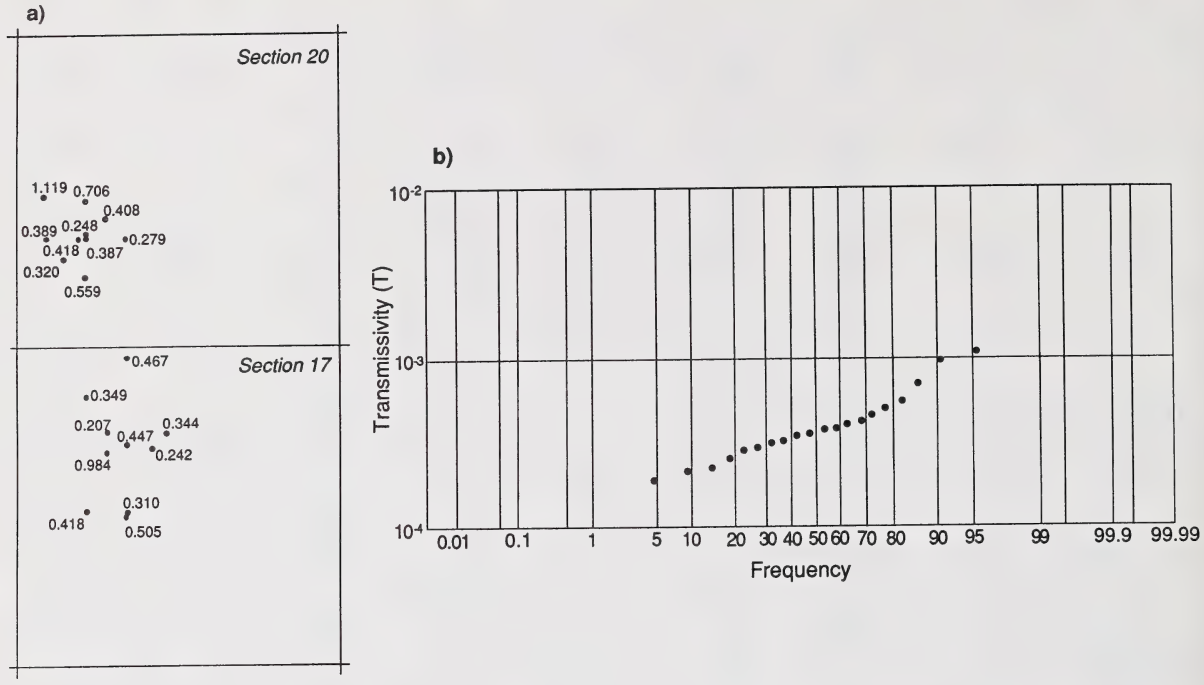

Figure 30. *Areal distribution (a) and cumulative probability plot (b) for transmissivity in the oil saturated blocky channel sand flow unit (areal transmissivity values are* $\times 10^{-3}$ m^2 */ sec).*

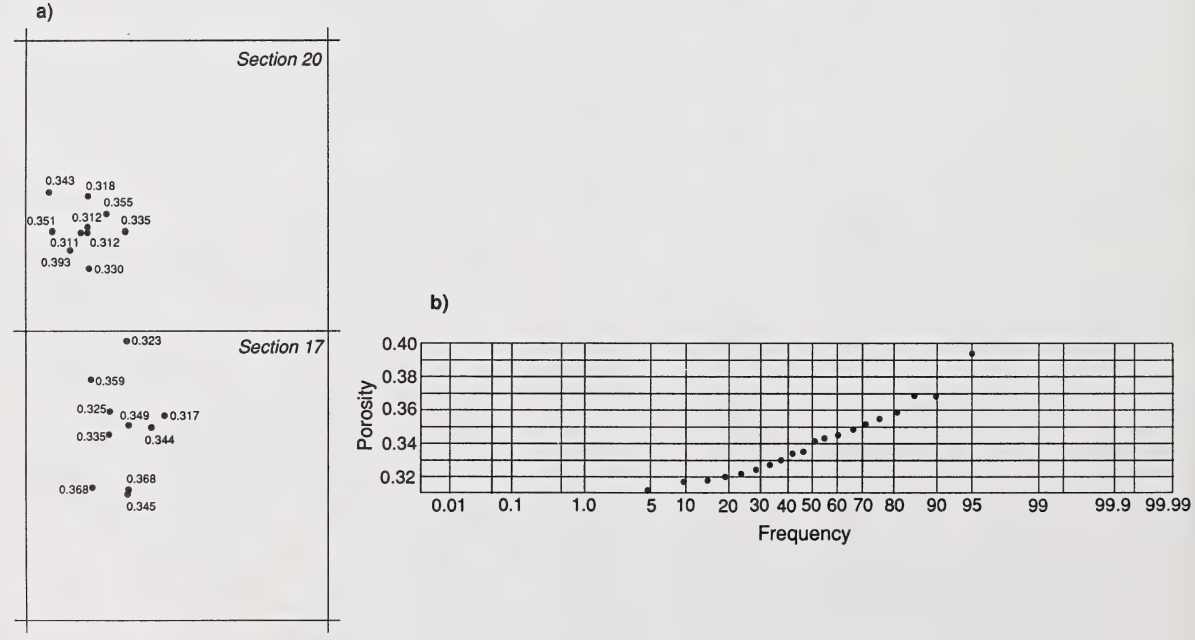

Figure 31. *Areal distribution (a) and cumulative probability plot (b) for porosity in the oil saturated blocky channel sand flow unit.*

Table 3. *Reservoir-scale characteristic values of porosity and transmissivity for the sandy flow units in the northern portion of the Provost Upper Mannville B Pool.*

Flow unit	Number of wells	Porosity		Transmissivity (10^{-4} m^2/sec)	
		Characteristic value	Variance σ	Characteristic value	Variance (σ of ln T)
Channel margin sands	15	0.255	1.1×10^{-3}	0.095	0.706
Transition zone sands	18	0.306	7.0×10^{-4}	0.514	0.285
Oil-saturated Blocky Channel sands	21	0.342	4.0×10^{-4}	4.200	0.177
Water-saturated Blocky Channel sands	2	0.246	–	0.250	–

Figure 30 presents the areal distribution and cumulative frequency plot for transmissivity values of the oil saturated blocky channel sands flow unit. The effective (or characteristic) transmissivity value for each flow unit was calculated as the geometric average of the respective frequency distribution. In the absence of any areal porosity trend, the effective porosity value at the flow unit scale (normally distributed, Figure 31) was taken as the arithmetic average of the well values. Table 3 presents the characteristic transmissivity and porosity values at the reservoir scale for the northern portion of the Provost Upper Mannville B Pool. These effective values are dependent on the flow conditions (Dagan, 1989), which in this case are assumed to be steady and uniform for the natural flow regime.

Permeability Anisotropy

Only the horizontal component of permeability has been considered in the previous discussion. It is a matter of debate in both the scientific and reservoir engineering communities how vertical permeabilities should be averaged to arrive at a characteristic value for "relatively uniform" flow units, such as the sandy portions of the Provost Upper Mannville B Pool. In the area of Sections 17 and 20, Twp. 37, Rge. 1W4, there are 58 k_v and 328 k_h core plug measurements. In order to arrive at a realistic effective value for vertical permeability, the k_v/k_h anisotropy was investigated. A companion k_h measurement was identified for every k_v measurement, on the basis of proximity and flow unit. This resulted in 33 pairs of k_v and k_h data points in the oil-saturated blocky channel sand flow unit, 17 pairs in the transition zone sand flow unit, and 8 pairs in the channel margin sand flow unit.

In the oil-saturated blocky channel sands, the k_v/k_h anisotropy ranges from 0.30 to 1.4 with a mean of 0.91 and a standard deviation of 0.21. Figure 32 presents a histogram of the k_v/k_h anisotropy and a scatter plot of k_v versus k_h for the oil-saturated blocky channel sands. Assuming that as k_h approaches a value of 0.0, k_v also approaches 0.0, a linear (least mean squares) correlation between k_v and k_h was found:

$$(3) \quad k_v = (0.866 \pm 0.034)\, k_h$$

with a correlation coefficient of $R^2 = 0.95$.

The k_v/k_h anisotropy ratio for the transition zone sands varies from 0.02 to 2.05 with a mean of 0.77 and standard deviation of 0.48. Figure 33a presents a scatter plot of k_v versus k_h for the transition zone sands. No correlation between k_v and k_h is presented for this flow unit because of the wide scatter in the data. For the channel margin sands, no statistics were calculated because of the small number of samples and the wide scatter of data points. The scatter plot for the channel margin sands (Figure 33b) could be interpreted as showing two populations: one in which the presence of horizontal clay laminae in the sands limit the value of k_v independently of k_h; and a second, more isotropic one where k_v and k_h could be related. In general, the vertical permeability for the channel margin sands is much lower than the horizontal permeability because of the interbedded silts and shales that occur in this flow unit. No data were available on vertical permeability for the water-saturated blocky channel sands. However, it may be assumed that the k_v/k_v ratio for these sands would be similar to that of the oil-saturated blocky channel sands because of their similar depositional origin.

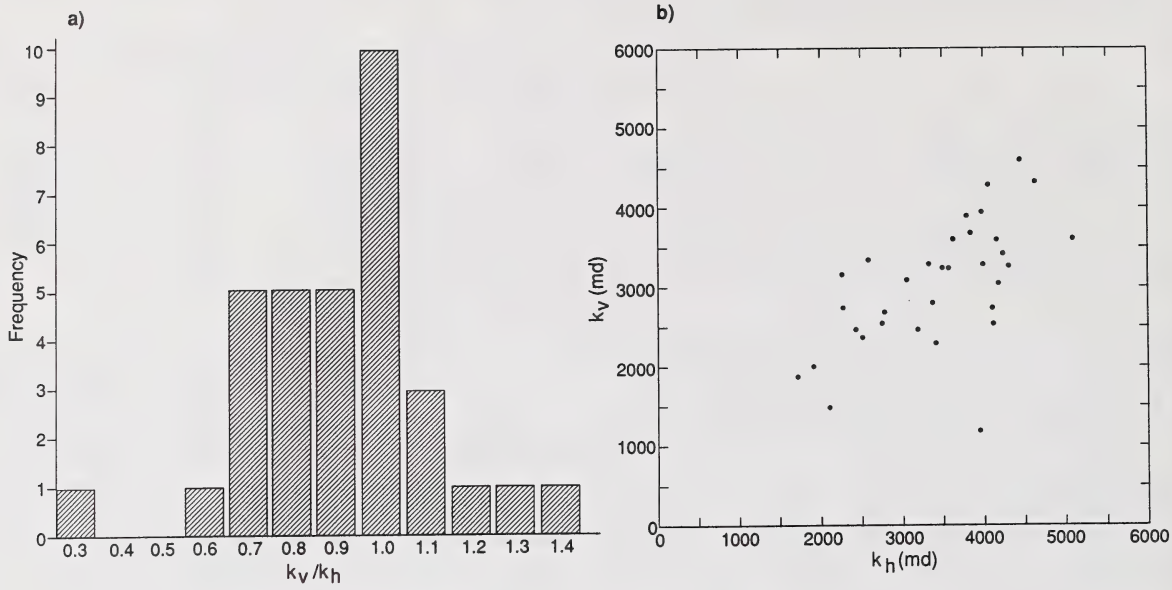

Figure 32. *Histogram for k_v/k_h anisotropy values (a) and scatter plot of k_v versus k_h (b) for samples from the oil saturated blocky channel sand flow unit.*

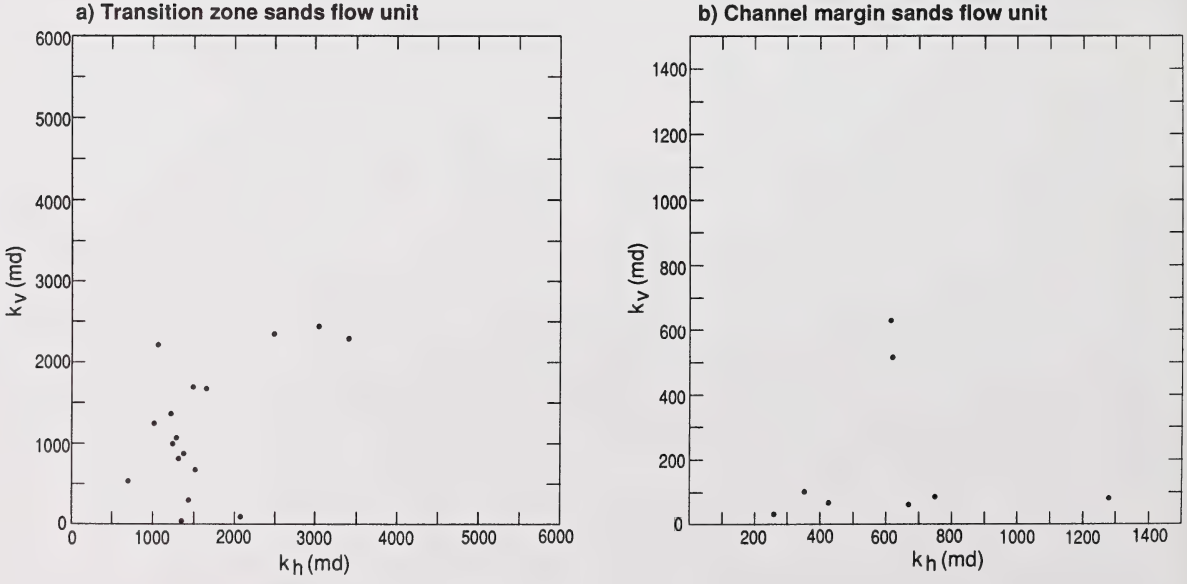
a) Transition zone sands flow unit
k_v (md)
k_h (md)
0 1000 2000 3000 4000 5000 6000
b) Channel margin sands flow unit
k_v (md)
k_h (md)
0 200 400 600 800 1000 1200 1400

Figure 33. *Scatter plots of k_v versus k_h for the transition zone sand flow unit (a) and the channel margin sand flow unit (b).*

HETEROGENEOUS FACIES CHARACTERIZATION

As observed in core, the shale clast lithofacies (Figure 9) is extremely heterogeneous. Individual clasts range in size from several millimetres to tens of centimetres and in shape from almost spherical to very flat. They are distributed in a seemingly random fashion and their local density (i.e., fraction by area) varies considerably over vertical distances of tens of centimetres. The shale clasts have permeability values that are probably at least three orders of magnitude smaller than that of the surrounding sand. Thus, zones of shale clasts are expected to represent significant barriers to fluid flow in the reservoir, and should be taken into account in reservoir recovery process simulations.

Numerical reservoir simulations require division of a region of the reservoir into grid blocks, each characterized by single values for permeability, porosity, and other petrophysical parameters. Because of computational limitations, grid blocks are typically constrained to have dimensions of at least metres and often tens or even hundreds of metres. When a clast zone is present within a region being simulated, a single grid block within the clast zone will contain a huge number of individual clasts. The challenge is to utilize observable properties of the shale clast distribution to assign effective values to the grid block permeability and porosity. What is required is a suitable method of "averaging" the properties of interest. More generally, the replacement of small scale complexity by a simpler description at larger scales—a ubiquitous process in science—can be described as a "scaling up" process (Lasseter et al., 1986; Bachu and Cuthiell, 1990).

In certain cases, the average of a spatially varying transport property such as permeability is known exactly. For example, consider the permeability of a layered region consisting of two layers of constant thickness, one having permeability k_1, the other k_2. Suppose that the fractions of the region occupied by the two types of layers are f_1 and f_2 ($= 1 - f_1$), respectively. With respect to flow parallel to the layers, the effective permeability of the region is given by the weighted arithmetic mean, k_{arith}, of the individual layer values, that is, by:

$$(4) \quad k_{arith} = f_1 k_1 + f_2 k_2$$

For flow perpendicular to the layers, the effective permeability is given by the weighted harmonic mean, k_{harm}, of the individual layer values:

$$(5) \quad \frac{1}{k_{harm}} = \frac{f_1}{k_1} + \frac{f_2}{k_2}$$

Both of the two idealized results (4) and (5) are easily generalized to more than two types of layers. Another idealized case consists of a spatially random distribution of permeability within a region. Suppose there are fractions $f_1, f_2, \ldots, f_N$ of permeability values $k_1, k_2, \ldots, k_N$, distributed randomly within the region. Then, under certain conditions (Warren and Price, 1961; Matheron, 1967), the effective permeability of the region is given by the geometric mean, k_{geom}:

$$(6) \quad \log\left(k_{geom}\right) = \sum_{j=1}^{N} f_j \log\left(k_j\right)$$

Considering distributions of shale clasts such as that shown in Figure 9, it is evident that the sand/shale distributions are neither completely layered nor completely random. Therefore, none of the simple predictions given by equations (4), (5), or (6) are expected, a priori, to be suitable. Alternative methods of scaling up need to be considered.

A number of methods for scaling up transport properties have recently been proposed both in the hydrogeological and reservoir engineering literature. One approach is the averaging of the equations satisfied by the phase variables, taking into account the interphase boundary conditions (Quintard and Whitaker, 1987). A different approach (Dagan, 1982, 1986; Gelhar et al., 1979; Gelhar and Axness, 1983) considers the spatial heterogeneity as random, and uses the apparatus of stochastic processes within the framework of a statistical theory of transport processes in porous media. These two approaches and

others are reviewed and compared in greater detail by Bachu and Cuthiell (1990). Although they are of great theoretical value, these methods are in many cases of limited practical applicability because of excessive, sometimes insurmountable mathematical and computational complexity. A much simpler "streamtube" approach has been used to compute effective permeabilities for systems of large, flat shale lenses (Haldorsen and Lake, 1984; Begg and King, 1985; Begg et al., 1987). The method is not, however, applicable to dense configurations of shales or shales of non-rectangular shape. A more generally applicable, but still straightforward approach utilizes fine scale numerical simulations to find the resulting flow for a particular heterogeneity distribution and pressure drop. Effective permeability is then computed using Darcy's law (Warren and Price, 1961; Begg and King, 1985; Desbarats, 1987b; Deutsch, 1989). The last approach has been used in this study since it is the most suitable for the complex, binary heterogeneity represented by shale clasts.

Although shale clast distributions appear to be reasonably uniform (in a statistical sense) over distances on the order of 10 cm, they cannot normally be considered uniform over regions as large as simulator grid blocks. It is therefore useful to approach the calculation of effective permeability of a grid block in two separate steps: first, scaling up to a scale of about 10 cm; then, scaling up again to the scale of the grid block.

Both scaling up steps have two main requirements: representing the geometry and spatial characteristics of the heterogeneity, and simulating the fluid flow. Representing the geometry is not completely straightforward since core observation provides only small, two-dimensional samples of the clasts. In general, three-dimensional distributions of clasts must be simulated using stochastic methods based on two-dimensional data. Flow simulations conducted for the simulated clast distributions require special methods to deal with the very complex geometry of the shale clasts.

Most of this chapter focuses on the calculation of effective permeability for regions of the reservoir the size of simulator grid blocks. Generally, the calculations are based on distributions of shale clasts observed in core from the Provost Upper Mannville B Pool reservoir. However, the last two sections generalize and extend the results to other sand/shale heterogeneities, and to the calculation of effective porosity and compressibility of shale clast zones under transient flow conditions.

Geometry and Architecture of Shale Clast Zones

As a prelude to characterizing the flow properties of the heterogeneous shale clast lithofacies, it is essential to understand the characteristics of this heterogeneity. The geometry and architecture of the heterogeneity should be expressed, as much as possible, in quantitative terms. When complete information or quantitative descriptions are not directly available—an inevitable situation with subsurface geology—recourse can be made to stochastic simulation techniques to provide an approximation to the unknown characteristics.

A shale clast zone exhibits heterogeneity at several distinct length scales, as illustrated in Figure 18. The fundamental heterogeneity is represented by the contrast in properties between individual shale clasts and the surrounding sand matrix. This heterogeneity is further characterized by the sizes, shapes, and spatial distributions of the shale clasts. It may be argued, in an informal sense, that a region of the typical diameter of core or having dimensions of the order of 10 cm is just large enough to provide a representative sample of the sand–shale geometry. By contrast, a 1 cm × 1 cm (or smaller) region might contain only sand or only shale and therefore would not provide a meaningful sample of the shale clast distribution. In the following, this basic length scale is referred to as "core scale."

At a somewhat larger scale, clasts occur in distinct layers that are on the order of a metre in thickness and several to tens of metres in lateral extent. A typical example of a layer observed in core is shown in Figure 34. The data for this example came from digitizing all of the clast outlines observed in that interval of core. It is apparent that there are distinct sublayers or "beds" within this layer. The transition between one bed and the next is marked by a sudden change in the size distribution and/or shapes of the clasts, while within the same bed these properties change gradually if at all. These features are expected geologically, since different beds are created by individual events, which are not likely to

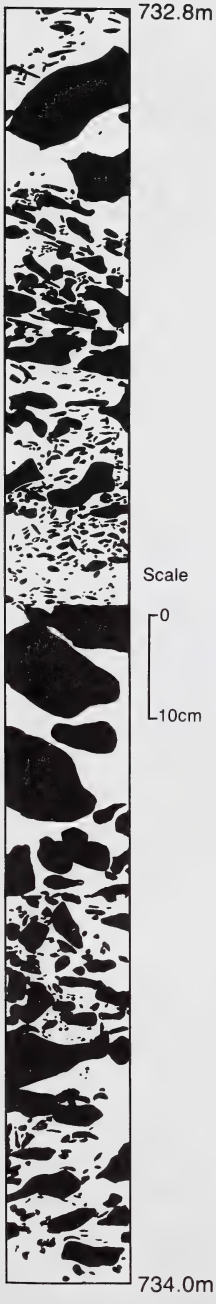

Figure 34. *Digitized version of a typical shale clast layer.*

result in similar clast characteristics. The spatial variations in clast shape, size, and density characterize the heterogeneity at the layer scale.

At yet a larger scale, which will be referred to as "zone" scale, individual shale clast layers are interbedded with layers of sand. Figure 35 shows the interpreted outline of a shale clast zone in a portion of the Provost Upper Mannville B Pool. The zone is between four closely spaced wells, and the layers of clasts are shown as they were observed in core. As is apparent in the figure, individual shale clast layers cannot generally be correlated between wells and therefore represent a "non-deterministic" heterogeneity (Haldorsen and Lake, 1984) at the zone scale.

Core scale characteristics. It is attractive to consider obtaining three-dimensional information about the shapes and distributions of clasts by some direct, non-invasive technique, if possible. A scoping experiment to test the possibility of using x-ray computed tomography (CT) for this purpose was carried out using CT equipment available at the Alberta Research Council. A sample of slabbed core was used for the test (full core not being available). Although the x-ray attenuation contrast between the shale and sand provided good discrimination of the two lithologies, the resolution of the available CT equipment was not adequate to provide detailed shapes of the smaller clasts. Thus, although the technique might be useful with higher CT resolution, it was not helpful in this study.

As an alternative, two-dimensional core scale information was collected from three cored wells in the Provost Upper Mannville B Pool. Two of the wells (05/5A-20-37-1W4 and 04/5B-20-37-1W4) were located in the same experimental pilot pattern and had a separation of 200 m. These two wells will be referred to as wells A and B, respectively. The third well (14-29-37-1W4) is located several kilometres from wells A and B, and will be referred to as well C.

Clast data were captured by manually tracing the outlines of all observed clasts in the clast zone from core for each of the three wells. The clast outlines were subsequently digitized, thus being represented as polygons with as many as 100 sides. The final data set comprised some 7000 clast outlines, representing approximately 20 m of core.

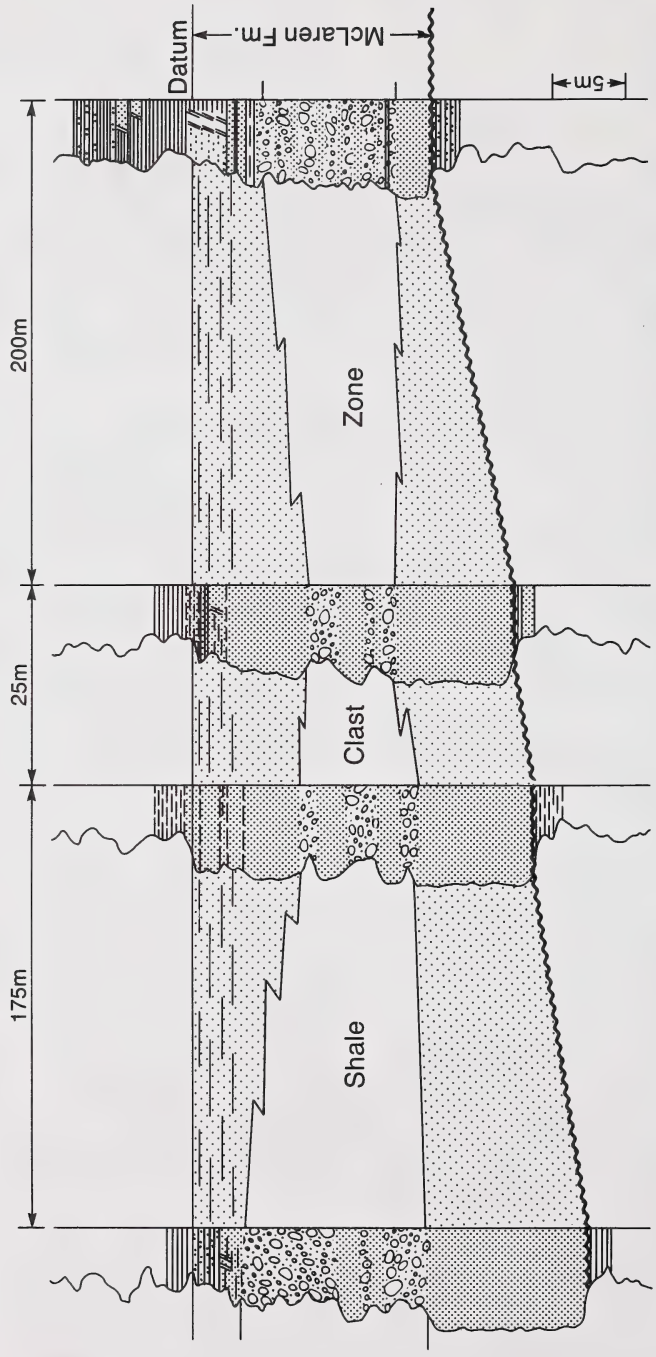

Figure 35. *Stratigraphic cross section through four closely spaced wells with core control showing the geometry of a shale clast zone.*

In principle, similar data could be captured using computerized image analysis techniques. This would, however, have been difficult with the available core because of the very poor visual contrast between some of the clasts and the sand as a result of absorption of oil by the clasts. However, in any large scale efforts to capture heterogeneity data of this type, automated data capture techniques should be developed and used.

The clast outlines in the data set are defined mathematically as polygons. The properties (e.g., area) of the polygons are readily calculated by standard numerical techniques. To define an orientation for a polygon, it is useful to compute the "moment of inertia" tensor for the polygon (Tough and Miles, 1984), where this terminology comes from mechanics. The tensor has associated with it a principal axis which may be taken to define the orientation direction of the clast. This objective mathematical definition agrees well with visual intuition in real cases. The "length" and "width" of the clast are defined as the dimensions of the smallest rectangle oriented in the principal direction circumscribing the clast (Figure 36). An "aspect ratio" is defined as the width/length ratio, and a "shape factor" as the area of the clast divided by the area of the circumscribing rectangle. The latter parameter is a measure of how nearly the clast fills the enclosing rectangle; it has the value 1.0 for a rectangular clast and $\pi/4$ (0.785) for an elliptical clast.

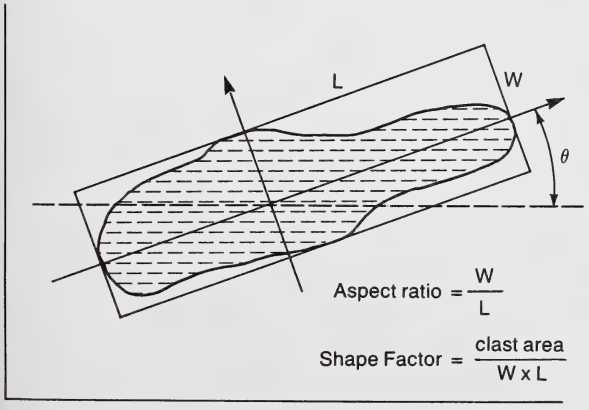

Figure 36. *Geometric parameters characterizing a shale clast. Arrows illustrate the principal axes of the moment of inertia tensor.*

Figure 37 shows distributions of clast length, orientation, aspect ratio, and shape factor for each of the three wells. Statistical properties of these distributions are summarized in Table 4.

Table 4. *Means and standard deviations (in parentheses) of the clast characteristic distributions shown in Figure 37.*

Clast parameter	Well A	Well B	Well C
Length (cm)	−0.13	−0.21	−0.32
(log scale)	(0.33)	(0.32)	(0.31)
Orientation	0.2	1.9	3.5
(degrees)	(36.2)	(35.3)	(46.4)
Aspect ratio	0.52	0.52	0.58
	(0.18)	(0.18)	(0.18)
Shape factor	0.68	0.73	0.72
	(0.09)	(0.06)	(0.07)

The length distributions (Figure 37a) are approximately lognormal with means around 5 mm. There are noticeable differences between wells; in particular, well C, which is more distant from wells A and B than the latter are from each other, contains significantly smaller clasts. However, the widths (standard deviations) of the three distributions are very similar. Since only complete clasts were analyzed, there is a bias; large clasts are more likely than small clasts to be cut off by the edges of the core and thus excluded from analysis.

The orientation distributions (Figure 37b) show that the clasts are predominantly subhorizontally aligned, although a significant number are as much as 30° and a few up to 90° from horizontal. The angular distribution is considerably broader for well C. Aspect ratios (Figure 37c) are broadly distributed with a mode somewhat less than 0.5. Again, the clasts from well C have a significantly different distribution of aspect ratios than those from the other two wells. The shape factor distributions (Figure 37d) peak at about 0.75 and indicate very few clasts with shape factor near 1. This shows that the clasts are closer to being ellipses (shape factor 0.785) than rectangles (shape factor 1.0). Curiously, in the case of shape factor, there is more difference between the nearby wells (A and B) than between B and the more distant well C.

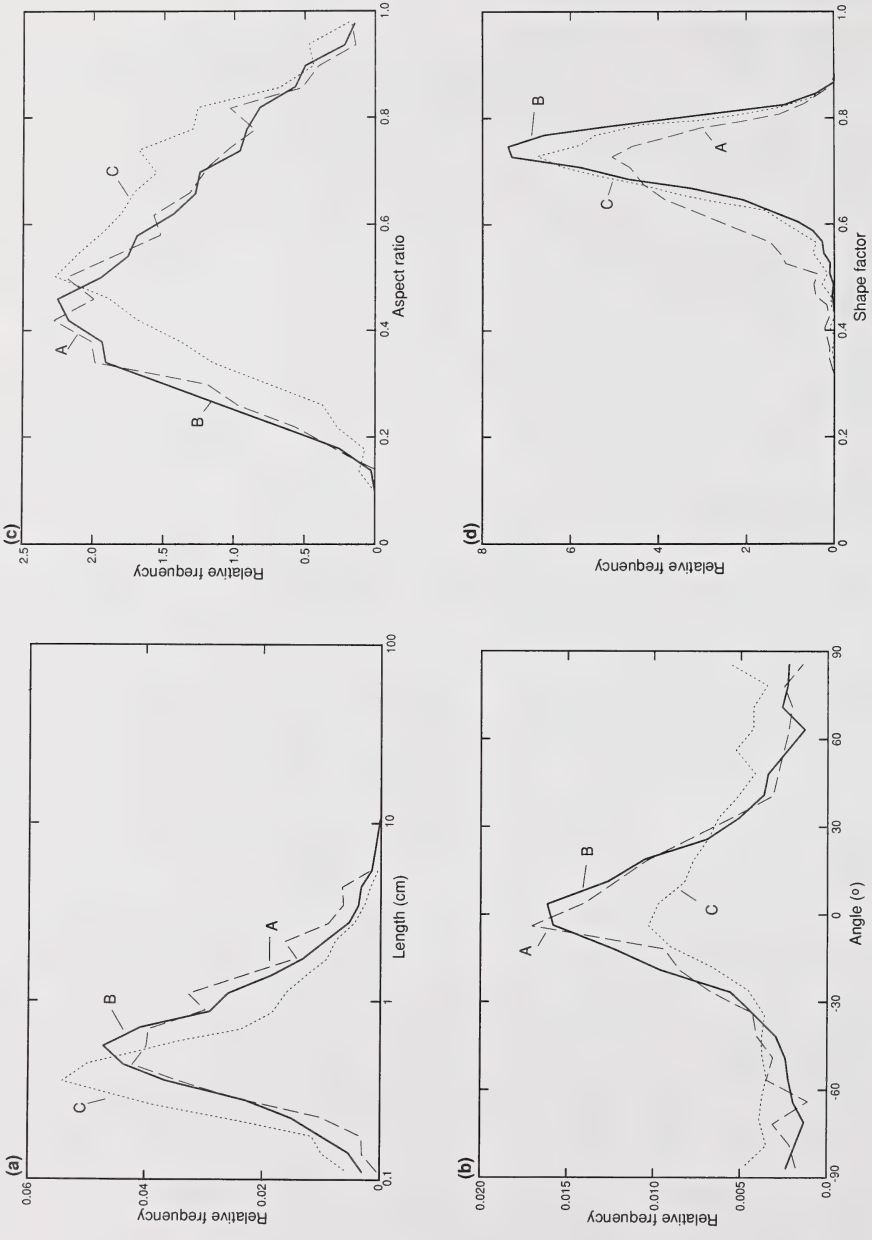

Figure 37. *Frequency distributions for clast parameters in wells A, B, C: (a) length, (b) orientation, (c) aspect ratio, (d) shape factor.*

Statistical analysis reveals that the properties length, aspect ratio, shape factor, and orientation have relatively little correlation. For example, the correlation coefficient between length and aspect ratio is −0.2, indicating a weak negative correlation between the properties. This justifies the independent treatment of length and aspect ratio in simulating clast geometry (see later).

In addition to the properties of individual clasts, a potentially important factor controlling permeability reduction is the spatial relationship among clasts. Spatial correlations in geological data are traditionally captured in a semi-variogram for the variable of interest. For the clast heterogeneity, the appropriate variable is one which recognizes the essentially binary character of this type of heterogeneity, the so-called "indicator" variable $I(x)$ defined at any spatial location x by:

$$(7)\quad I(x) = \begin{cases} 1, \textit{for } x \textit{ in shale} \\ 0, \textit{for } x \textit{ in sand} \end{cases}$$

In the geostatistical approach, a particular core sample is regarded as a single realization of a spatial random field. With appropriate assumptions of stationarity (Journel and Huijbregts, 1978), a semi-variogram $\gamma(h)$ is defined as:

$$(8)\quad \gamma(h) = \frac{1}{2N} \sum_{i=1}^{N} \left\{ \left[I(x) - I(x+h) \right]^2 \right\}$$

where the summation is over the N pairs of locations separated by a particular "lag," h. Semi-variograms can be computed in practice by rasterizing (that is, approximating on a lattice of square cells) the clasts found within a particular region, then performing the summation in equation (8) over all cells with the same separation h. In making this calculation, it is essential to choose a region large enough to contain a reasonable sample of the heterogeneity, yet small enough for the distribution of heterogeneities to be statistically homogeneous or stationary. A practical choice of region in light of the structure within clast layers is all or part of a single bed, limited of course by the physical width of the core. An indicator semi-variogram is shown in Figure 38 for one sample of shale clast data (see inset in figure). Only horizontal and vertical lags are considered for illustration. Both the vertical and horizontal semi-variograms for the sample are fit very well by a standard exponential type of variogram:

$$(9)\quad \gamma(h) = \gamma_s \left(1 - e^{-\alpha h}\right)$$

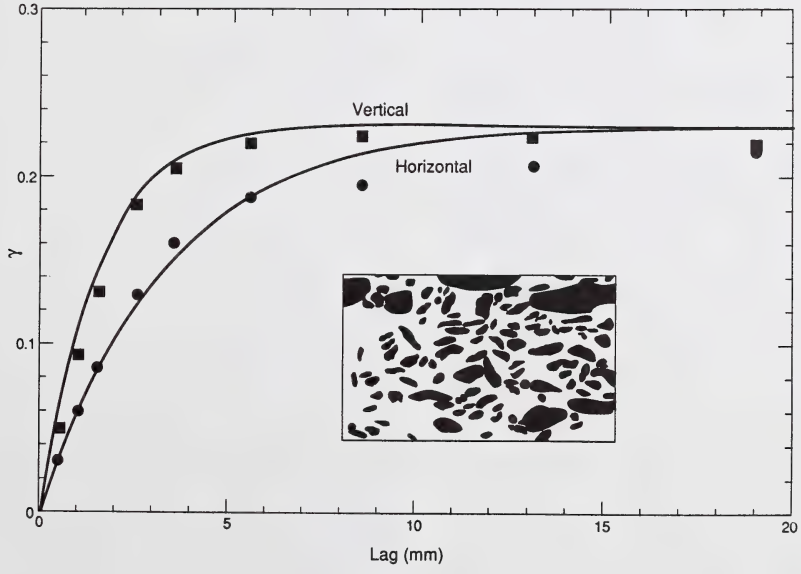

Figure 38. *Semi-variograms for vertical and horizontal lags for a sample of digitized clast data set (inset).*

Assuming that any correlations present are of finite range, the sill value, γ_s, should theoretically equal $f(1-f)$, where f is the shale clast fraction (Desbarats, 1987b). Both horizontal and vertical fits in Figure 38 assume this theoretical sill value.

The rate at which the semi-variograms approach their "sill" or asymptotic values γ_s as lag increases is determined by the parameter α. A slower approach to the sill (smaller α) reflects a greater spatial correlation range in the corresponding direction. For the case shown and in general, a greater range of correlation is present for horizontal lags than for vertical. This reflects the predominantly subhorizontal orientation of the clasts and their typically elongated shape. Semi-variograms for other samples of similar size generally display different ranges of correlation from this example (i.e., different parameters α). This is a consequence of variations in the sizes of clasts for different regions.

Large scale characteristics. At the core scale, it is the shape and location of clasts that characterize the heterogeneity geometrically. At the larger reservoir grid block scale, the appropriate description is one in terms of the averaged variable "shale clast fraction." This variable can, in principle, be defined at any point in space as the fraction of shale clasts within some representative averaging volume surrounding the point. Based on previous discussions, a practical averaging volume is a region of about core size, that is, with dimensions of order 10 cm. This change in the nature of the description of the same property between different scales is typical of multiscale phenomena. For example, it is analogous to the replacement of pore and grain shapes at the microscale by porosity at core scale.

The data from a vertical well provide only a one-dimensional sample of the true three-dimensional variation in shale clast fraction within a clast zone. This vertical distribution can be obtained for each of the three wells that were digitized. The distribution of shale clast fraction for well B, using a 20-cm sampling interval, is shown in Figure 39. Individual shale clast layers can be recognized in the figure as contiguous groups of 20-cm intervals having non-zero shale fraction. The set of 20-cm shale clast fraction values within each layer may be regarded as a "sample" and differences between layers may be tested statistically.

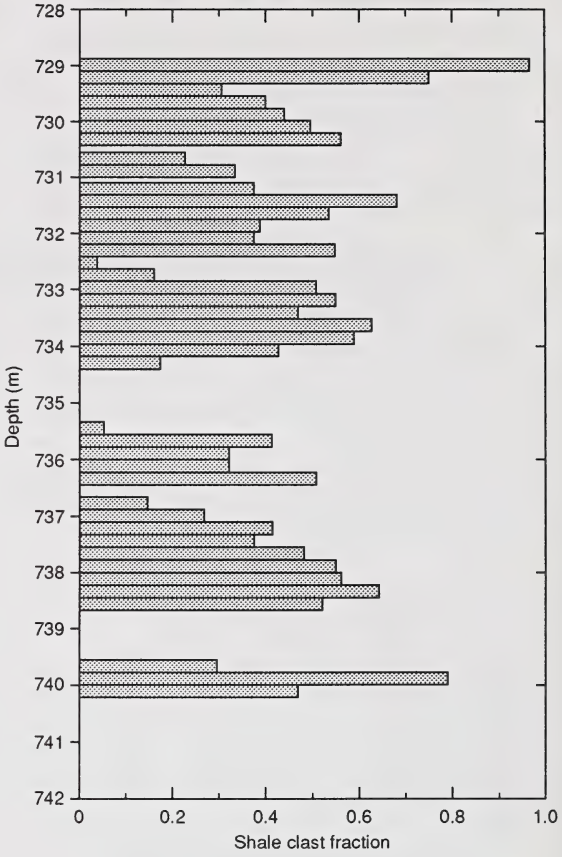

Figure 39. *Distribution of shale clast fraction with depth for well B (20 cm sampling intervals).*

An analysis of variance for these data shows no significant difference between the mean shale clast fractions in the different layers (significance level = 0.47). That is, one cannot statistically disprove the assertion that the samples representing different layers were all selected from the same population. An assumption consistent with this result is that all core-sized regions selected from anywhere within the clast layers in the same well come from the same statistical population. The frequency distribution associated with that population may be inferred by pooling all of the 20-cm interval values of shale clast fraction for all layers. For well B, the resulting frequency distribution for shale clast fraction is shown in Figure 40.

Figure 40 shows the frequency distribution of shale clast fraction, but reveals nothing about the

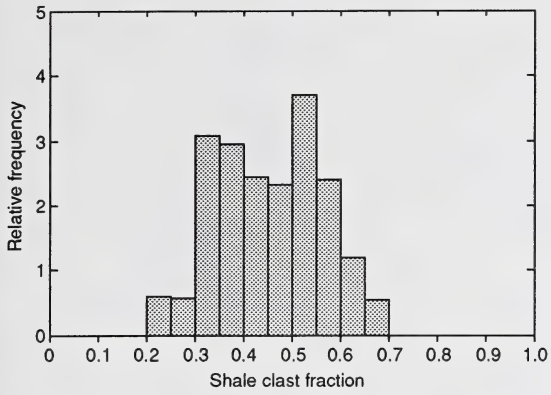

Figure 40. *Shale fraction distribution within layers in well B based on observed fractions (20 cm sampling interval) from all layers.*

spatial distribution of this variable, which has an important impact on flow. For example, if a certain distribution of shale clast fractions were arranged in a completely stratified fashion within a single layer of shale clasts, the vertical permeability of that layer would be lower than if the same shale clast fractions were arranged in a more spatially random manner. The spatial variations, or correlations of shale clast fraction would ideally be described by a semi-variogram. In the present case, a full 3D semi-variogram describing shale clast fraction correlations cannot be determined since only one-dimensional data are available. In principle, 2D or 3D spatial information could be obtained from outcrop studies, which were not a part of this project. In the absence of other information, the approach adopted was to consider several possible scenarios for spatial variability, especially extreme cases with regard to flow.

Generating Synthetic Core Scale Distributions of Clasts

The three-dimensional (3D) geometry of shale clasts is required in order to estimate the flow properties of a core scale region containing clasts. However, only two-dimensional (2D) information about the clasts is readily available. This leads to the need for simulating 3D clast distributions, that is, creating them by some computational process. Two basic problems need to be addressed: how to infer 3D shapes from 2D data and how to simulate realistic spatial arrangements in 3D. The first problem, that of reconstructing 3D shape information from 2D section data, was approached using stereological methods. Methods of simulating spatial variability in geological systems can be classified broadly as either "continuous" or "discrete" (Haldorsen and Damsleth, 1990). The continuous methods, which normally utilize the tools of geostatistics, have found their most fruitful application in describing rock properties that vary continuously, such as porosity or permeability within sand bodies. Discrete methods have been applied to simulating the external geometry of features that are inherently discrete such as sand bodies, facies, and shales. A discrete method therefore seems more appropriate for the creation of synthetic clasts and was the method of choice for this study.

In order to readily apply stereological methods to infer 3D clast properties, an assumption is required about clast shapes. Two-dimensional sections of clasts have some resemblance to ellipses, at least in an average sense (Figure 37, Table 4). This suggests that three-dimensional clasts may be approximated by oblate ellipsoids, surfaces of revolution resulting from rotating an ellipse about its minor axis. By definition, oblate ellipsoids produce ellipses when sliced by planes parallel to their minor axis, and circles when sliced at right angles to that axis.

To employ oblate ellipsoidal "clasts" for numerical flow simulations, the synthetic clasts need to be represented discretely on a computational grid (a 128 × 128 × 128 grid was used in the present study). This makes it difficult to represent non-horizontal clasts. Therefore, the ellipsoids were always assumed to be oriented horizontally, corresponding to the average orientation of real clasts (Figure 37b). Choosing x and y axes in the horizontal plane, and the z axis vertically, an oblate ellipsoidal surface is defined mathematically by the points (x, y, z) satisfying the equation:

$$(10)\quad \frac{(x-x_c)^2}{a^2}+\frac{(y-y_c)^2}{a^2}+\frac{(z-z_c)^2}{b^2}=1$$

where a is half the longest dimension of the ellipsoid, b is half the shortest dimension, and (x_c, y_c, z_c) are the coordinates of its centroid. The aspect ratio of the oblate ellipsoid is defined as b/a.

If a region containing a large number of oblate ellipsoids, having a variety of sizes and aspect ratios, is sliced by a vertical plane, then a collection of ellipses will be observed in the resulting 2D section. These ellipses will also have some statistical distribution of sizes and aspect ratios. If the distribution of ellipse shapes obtained from many such sections is known, stereology allows the original size and aspect ratio distributions of the ellipsoids to be inferred. Details of this procedure are discussed in Appendix B.

The 2D data required for the stereological calculation were taken from a subset of the complete clast data set. Specifically, four intervals from the clast data for well B were selected, each being of comparable width and height, having a relatively large number of clasts, and being suitable for subsequent 2D flow simulations. The selected intervals are shown in Figure 41 and the distributions of clast length and aspect ratio for the pooled set of clasts from the four intervals are shown in Figure 42. Since length and aspect ratio have a relatively weak statistical correlation, the statistical distributions of length and aspect ratio can be considered independently.

Any ellipses resulting from sectioning an ellipsoid have the same aspect ratio as the ellipsoid. Therefore, the distribution of ellipsoid aspect ratios must be the same as the 2D distribution shown in Figure 42b.

The 2D length distribution is fit very well by a lognormal distribution (R^2 = 0.989) as shown in Figure 42a. When this distribution is used as input to the stereological calculation, it produces a 3D frequency distribution of ellipsoid sizes that is also lognormal. More explicitly, the number of 3D ellipsoids having maximum (horizontal) dimension between s and ds is given by

$$(11)\quad dN(s) = \left(\frac{N_o}{s}\right)\exp\left\{-c\left[\log\left(\frac{s}{s_o}\right)\right]^2\right\} ds$$

where c = 8.0, s_o = 0.347 cm, and N_o is a dimensionless normalizing constant. Details of this calculation are described in Appendix B.

The size distribution given by equation (11) and the aspect ratio distribution of Figure 42b were used to create synthetic clast distributions. For practical simulations, the lognormal clast size distribution (equation (11)) was rescaled to have s_o = 11.3 in grid units and was cut off for sizes smaller than 4 grid units and larger than 40 grid units. The lower limit ensured that the oblate ellipsoidal shapes could still be represented to some degree for the smallest sizes, while the upper limit prevented single large clasts from overly dominating the flow.

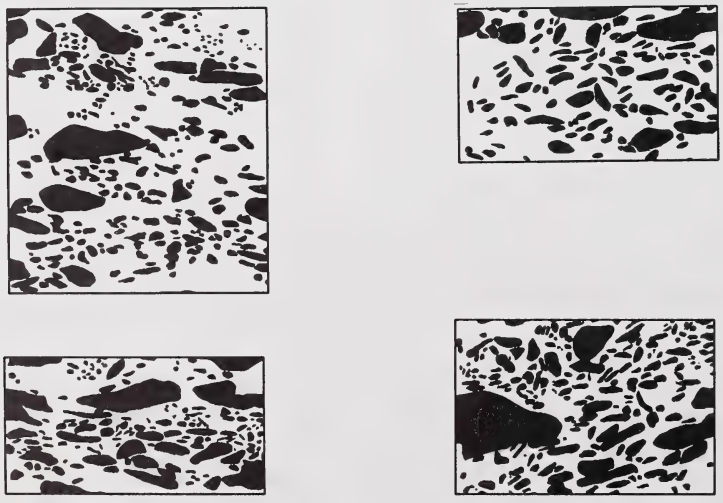

Figure 41. *Shale clast intervals from well B used as the basis of stereological calculations.*

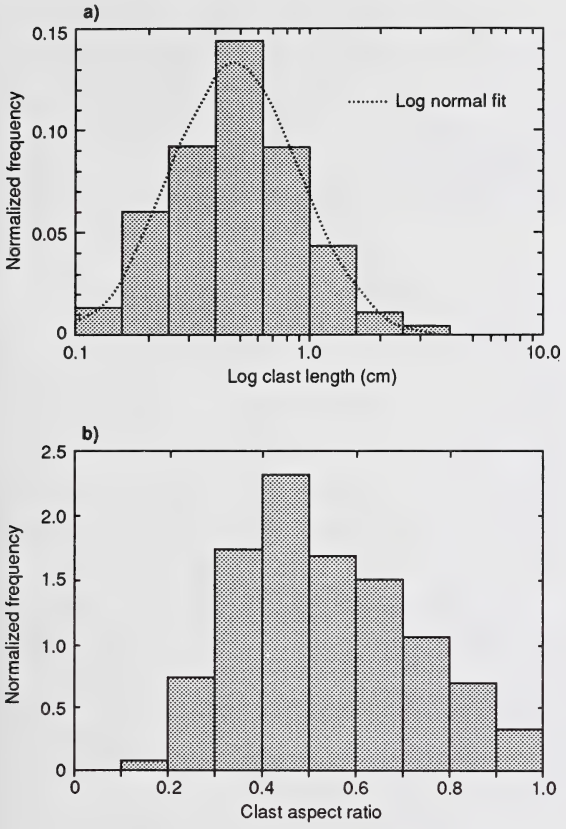

Figure 42. *Frequency distributions for length (a) and aspect ratio (b) based on all clasts from the intervals shown in Figure 41. The dashed curve in (a) represents a lognormal fit to the data.*

The 3D flow simulation program developed in this study requires that synthetic clast regions be represented on a cubical grid, in practice having dimensions 128 × 128 × 128. Clasts (oblate ellipsoids) are introduced one at a time onto this grid as discretized forms satisfying equation (10). The size of each ellipsoid is selected from the frequency distribution given in equation (11), and its aspect ratio from the frequency distribution shown in Figure 42B. Each new clast is introduced on the grid at a random location. The approach is thus a very simple type of discrete simulation method (Haldorsen and Damsleth, 1990), similar to the technique proposed by Haldorsen and Lake (1984) for simulating large shale lenses. Given the geological origin of clasts, the assumption of random (uncorrelated) locations for individual clasts seems reasonable.

The centroid location of each new clast is chosen subject to the requirement that the clast have only a certain maximum overlap with clasts already created. In practice, the maximum allowed overlap was chosen to be 5% of the volume of the new clast, and the requirement was satisfied by simply trying new locations until the new clast fitted. The small overlap permits clasts to touch, as they are observed to do in core.

During the numerical construction of clast distributions, statistical information is accumulated about the distributions of size and aspect ratio of ellipses in all of the $x-z$ planes of the grid (i.e., 128 planes). These distributions can be compared with those for real shale clasts to test the numerical procedure of creating synthetic clasts. Figure 43 compares the length distribution of 2D ellipses for a particular 3D simulated clast region with the input distribution for real clasts. The distributions agree very well, particularly for larger clast sizes. There is some disagreement at smaller sizes resulting from having imposed a lower cutoff of four grid blocks on the size of the ellipsoids generated. However, clasts from this lower end of the size distribution contribute very little to the total volume fraction of clasts. Figure 44 shows a similar comparison of aspect ratios between the synthetic 2D sections and the real clasts, and again, the agreement is good.

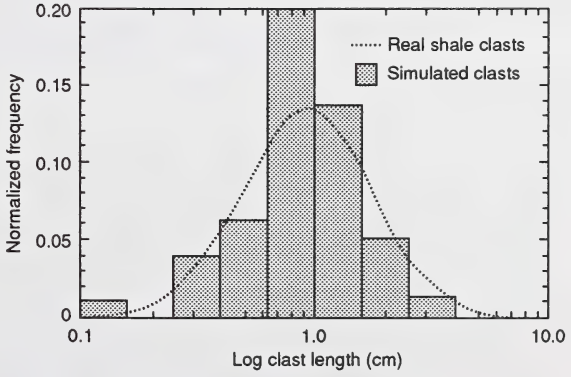

Figure 43. *Comparison of length distribution of clasts from 2D sections of a 3D simulated clast interval with the distribution for real shale clasts shown in Figure 42a (dashed curve).*

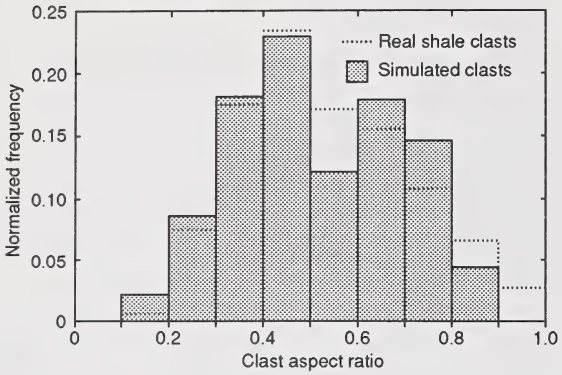

Figure 44. *Comparison of aspect ratio distribution of clasts from 2D sections of a 3D simulated clast interval with the distribution for real shale clasts shown in Figure 42b (dashed bars).*

It is also worthwhile to compare the semi-variograms for synthetic and real 2D shale clast intervals. Figure 45 shows semi-variograms computed for horizontal and vertical lags for one cross section of a 3D simulated clast system. As in the case of real shale clasts (Figure 38), the two directional semi-variograms are very well fit by a standard exponential model (equation (9)). The simulated clasts were positioned randomly in space. Therefore, the similarity in the form of real and simulated variograms suggests that the real clasts are also distributed randomly, as argued earlier on physical grounds.

Estimating Core Scale Permeability

In principle, the permeability of a core sample containing shale clasts could be measured directly. However, such measurements were not possible in this case study since full diameter core was unavailable. Analogue and numerical methods were employed as alternatives. Compared with direct measurements, the numerical method has the advantage of greater potential for generalization and extension.

The overall scheme of the numerical calculations is illustrated in Figure 46. From the original digitized clast outlines, 3D synthetic clast systems were constructed by methods which were discussed in the previous section. Three-dimensional numerical flow simulations were performed for a number of these

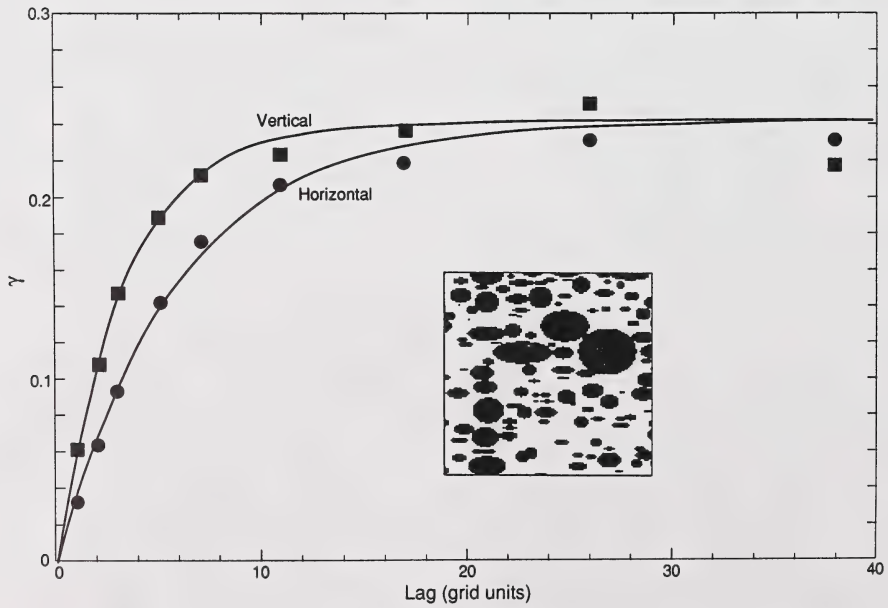

Figure 45. *Semi-variograms for vertical and horizontal lags for a 2D section of a simulated 3D clast interval (inset).*

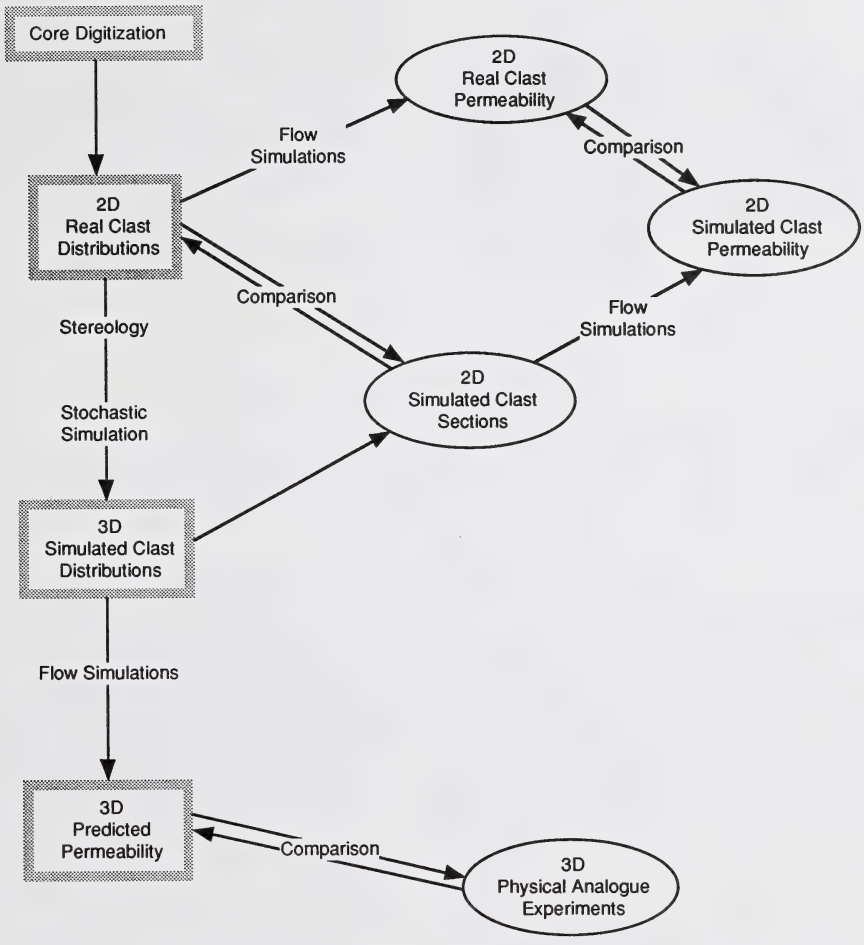

Figure 46. *Flow chart for numerical permeability calculations.*

synthetic clast regions, resulting in values for effective horizontal and vertical permeability of the regions. Comparison of the statistical properties of 2D sections of the synthetic clast systems with those from the digitized core provided some assurance that the 3D regions were being properly synthesized. The procedure was further tested by comparing results of 2D flow simulations for slices of the simulated clast regions with results of 2D flow simulations for actual clast intervals. Finally, results of 3D physical analogue experiments were compared directly with results of the 3D numerical simulations.

Core scale numerical flow simulations. A numerical flow simulation calculates an effective permeability by simulating a permeameter. The basic concept is illustrated in Figure 47. A "sample" of unknown permeability is saturated with fluid and subjected to a constant pressure difference between two opposite faces, $P_t - P_b$ in the figure. The other faces of the sample are assumed to be impermeable to flow. At steady-state, fluid will flow at a constant rate through the region. If the sample were homogeneous, the volumetric flow rate, Q, of fluid would be related to the pressure drop by Darcy's law:

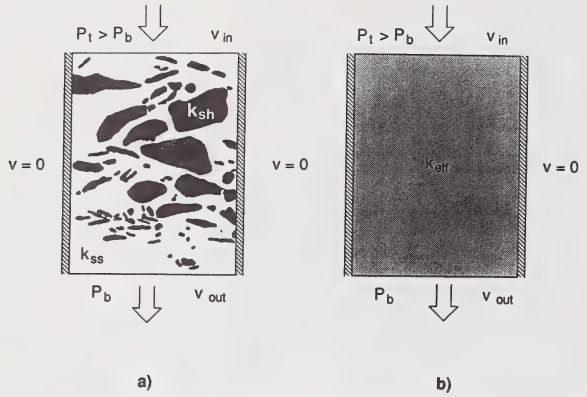

Figure 47. *The concept of a numerical permeameter: (a) heterogeneous sample; (b) equivalent homogeneous sample.*

$$(12)\quad \frac{Q}{A} = \left(\frac{k}{\mu}\right) \cdot \frac{\left(P_t - P_b\right)}{h}$$

where A is the sample cross section normal to flow, h is the height of the sample, and μ is the viscosity of the fluid. The parameter k would represent the permeability of the sample. In the case of an unknown, and in general non-homogeneous sample, equation (12) is taken to *define* the "effective permeability" of the sample. That is, if a volumetric flow Q results from a pressure difference $(P_t - P_b)$, then the effective permeability of the sample is defined as:

$$(13)\quad k_{eff} = \frac{Q\mu h}{A\left(P_t - P_b\right)}$$

Thus, the sample is regarded as equivalent to a sample of the same size with homogeneous permeability k_{eff} (Figure 47b).

The objective of the numerical simulation procedure is to impose the appropriate pressure and no-flow boundary conditions, compute the steady-state fluid flow rate, and thereby determine the effective permeability defined by equation (13). By changing the boundary conditions of the simulations, flow can be simulated in different directions and corresponding directional permeability values can be determined.

Most of the calculations carried out have utilized a finite difference (FD) method of simulation. Methods of this type have long been employed to solve systems of differential equations that arise in science and engineering. In the case of steady-state flow of a single incompressible fluid through a porous medium, the equations being solved are the differential form of Darcy's law (assuming no gravity):

$$(14)\quad v = -\left(\frac{k}{\mu}\right)\nabla P$$

and the mass conservation (or continuity) equation:

$$(15)\quad \nabla \cdot v = 0$$

where v is the Darcy velocity of the fluid. Combining these two equations, a single equation results:

$$(16)\quad \nabla \cdot \left(\frac{k}{\mu}\nabla P\right) = 0$$

It should be noted that the permeability k in equations (14), (15), and (16) is a local permeability; that is, it varies with position in the medium. This is in contrast to the effective permeability defined in equation (13) for the core scale region. For a system consisting of sand and shale clasts, the local permeability has a bimodal distribution, with relatively large values in the sand and much lower values in the shale. For simplicity, the distribution of permeability values can be approximated as binary, with sand being characterized by a single value and shale by another. Other researchers have found (Desbarats, 1987a; Begg et al., 1985) that this approximation introduces negligible error. A further assumption was made that permeability within either the sand or shale clasts was isotropic.

The FD calculation was performed on a grid consisting of an array of square grid blocks in two dimensions or cubical grid blocks in three dimensions. The binary sand/shale system was represented on this grid by assigning one of two values ("sand" or "shale") and its corresponding permeability to each of the blocks. The method of constructing the sand/shale distribution in three dimensions was described in the previous section. In the 2D case of shale clast outlines represented by polygons, a standard rasterization procedure was used to convert the clasts into a discrete form on the grid.

The flow simulation solves for the steady-state pressure at each of the grid "nodes" (corners of grid blocks). Details of the numerical method are given in Appendix C. Once the final pressure field has been found, the total flow through one face of the block can be found by using Darcy's law (equation (12)) for each of the blocks making up that face, and adding the results. Finally, the effective permeability for the whole region is found using equation (13).

An important practical issue in the use of the FD method is the choice of grid size. Since the FD method uses a discrete approximation to both the geometry of the clasts and the differential flow equations, discretization errors are inevitable. The size of these errors decreases with smaller grid spacing (i.e., greater number of grid blocks). However, the computation time increases very rapidly with the number of grid blocks limiting the size of the grid that can be used in practice.

These considerations can be illustrated with a specific example. Table 5 shows the computation time and calculated vertical permeability for one actual 2D shale clast interval (the interval having shale clast fraction 0.351 in Figure 54) as a function of grid size. The dramatic reduction in CPU time for smaller grid sizes is apparent. Perhaps surprisingly, the estimates of permeability do not change greatly over this range of grid sizes. From this and other cases examined in a similar manner, it seems that grid sizes as small as 100×100 can be used to give reasonable permeability predictions. When computer time is not critical, finer grids are of course preferred.

Table 5. *FD simulation performance for different grid sizes having shale clast fraction 0.351 illustrated in Figure 54.*

Grid size	Execution time (minutes)	Effective vertical permeability
586×386	240.0	0.1532
418×261	112.2	0.1519
335×209	59.4	0.1539
279×174	41.2	0.1543
213×133	17.4	0.1573
167×104	8.8	0.1542
117×73	3.0	0.1525

For three-dimensional simulations, the restrictions on grid size due to CPU and memory requirements are more stringent. With available computing resources (a DEC MicroVAX-3300), a practical limit for grid size was found to be $128 \times 128 \times 128$, and this grid size was used for all of the core scale simulations. Extrapolating from the 2D experience represented by Table 5, it is believed that discretization errors in 3D are probably less than about 5%.

At an early stage of the project, some 2D numerical flow calculations were performed using a finite element model (FEM). The model used was a commercial code known as FE3DGW (Gupta et al., 1984). The FEM approach differs substantially from the FD method, with the largest practical differences being in the form and size of the grid used to discretize the equations. The FEM uses an irregular grid comprised of quadrilateral elements, in contrast to the regular square grid used in the FD calculations. While the irregular elements confer some advantage in representing irregular geometry and the FEM is generally more computationally efficient, the construction of the FEM grid was a tedious, manual process that limited the practical utility of the method. The FEM approach is also not easily extended to three dimensions for clast geometries. However, the results of the FEM calculations (Bachu and Cuthiell, 1990) that were performed provided independent checks on the FD calculations.

Physical analogue measurements of effective permeability. Numerical calculations generally produce discretization errors of some (usually unknown) magnitude. It is therefore useful to validate the numerical results by means of independent physical measurements. As discussed previously, direct measurement of permeability using core was not possible. As alternatives, several types of physical analogue systems were utilized.

Validation of the 2D flow simulations was obtained using an electrical analogue method. The technique was similar to one used previously for systems of shale lenses (Dupuy and LeFebvre du Prey, 1968) and exploits the mathematical analogy between single phase fluid flow and the conduction of electrical current. A two-dimensional clast region is represented by a sheet of electrically conducting paper, with holes cut into it in the shapes of clasts, and equipotentials

created at each end using highly conducting paint. The effective conductivity is found by comparing the resistance of the sheet with "clasts" (i.e., holes) to that of the original sheet with no "clasts." Since the holes in the paper have zero electrical conductivity, the analogue results correspond strictly to shale clasts of zero permeability in the fluid flow case.

In order to provide experimental confirmation of the 3D numerical simulations, a constant head permeameter was designed and built. The permeameter is illustrated in Figure 48. It is constructed of aluminum and consists of a water reservoir connected to a chamber holding the sample for which the permeability is to be measured. A constant head is maintained during flow by means of low restriction overflows on both the water reservoir and the sample cell.

Analogue 3D clast systems were constructed by embedding quartzite pebbles in 10/20 resin-coated frac sand that could be consolidated by heating the sand in an oven at 140°C for 10 hours. This provided solid blocks, 20 cm on a side, for use in the permeameter.

The pebbles used in the blocks ranged in size from 1.2 to 7.6 cm and had an average aspect ratio of approximately 0.5, similar to that of actual clasts (Figure 37c). In order to simulate the randomness of real shale clast distributions, the pebbles were placed in the sand manually, as randomly as possible, with a predominantly subhorizontal orientation. A number of blocks were constructed, with volume fractions of pebbles ranging from 10% to 35%.

A block could be placed in the permeameter in any of three orientations. For each flow direction, the flow rate was determined by measuring the volume of water leaving the permeameter during a 60-second period following the stabilization of flow. Six such measurements were averaged. To find the permeability reduction caused by the pebbles, flow measurements were also performed for two reference blocks containing no pebbles. Results of these experiments will be discussed in the next section.

Following completion of the flow measurements, the blocks were cut into slabs at about 2.5-cm spacing. The cuts were made vertically, so that the sections produced could be compared with those observed for real shale clasts in core. The pebble outlines in each slice were digitized by methods similar to those used for the clasts. Figure 49 shows several examples of the 2D sections obtained by this method. Based upon visual examination of the sections, it was concluded that four of the blocks could be regarded as reasonable analogues of clasts. The digitized pebble outlines for these four blocks were also used as the basis for 2D numerical flow simulations, the results of which could be compared with similar 2D results for digitized shale clasts.

Results and discussion. Numerical flow simulations were performed for eight three-dimensional cases, with varying fractions by volume of simulated clasts. In each case, a 128 × 128 × 128 simulation grid was employed and both vertical and horizontal flow were simulated. Figure 50 illustrates a single vertical cross section through the middle of each of the eight simulated regions.

Table 6 summarizes the properties of the simulated clast intervals and the computed horizontal and vertical permeabilities for each. The intervals span a range of simulated clast fractions from less than 10% to over 70% and, for the largest fractions, contain more than 5000 oblate ellipsoids. In all of the simulations, the ratio of shale to sand permeability was taken to be 0.001.

The horizontal and vertical permeability values for the eight cases are shown in Figure 51. In this figure, and others to be shown later, effective permeability is expressed in a dimensionless form relative to the permeability k_{ss} of the sand matrix. Effective permeability, thus defined, approaches unity as the fraction of clasts approaches zero.

Figure 51 shows a reduction of nearly a factor of 10 in permeability when 70% clasts are present in the sand matrix. The corresponding reduction in horizontal permeability is around a factor of 5. The greater reduction in vertical permeability relative to horizontal occurs over the entire range of shale fractions. This anisotropy of permeability at the core scale is a consequence of the oblate or flattened shape of the simulated (or real) clasts, which presents a greater impediment to vertical flow than to horizontal.

A generalized weighted mean model (Korvin, 1982; Journel et al., 1986):

$$(17)\quad k_{eff} = \left[f \left(\frac{k_{sh}}{k_{ss}} \right)^{\omega} + 1 - f \right]^{(1/\omega)}$$

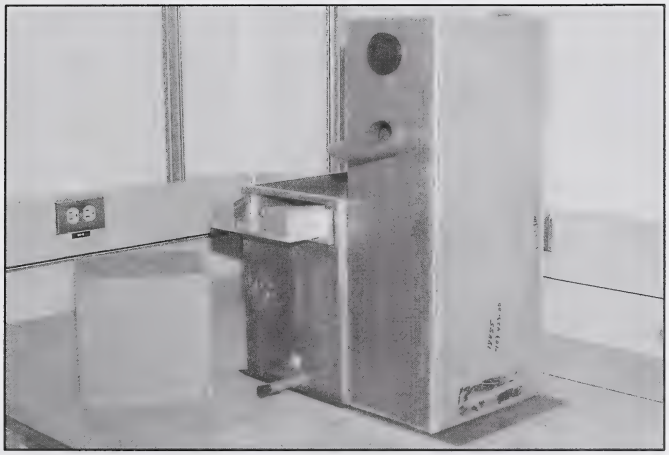

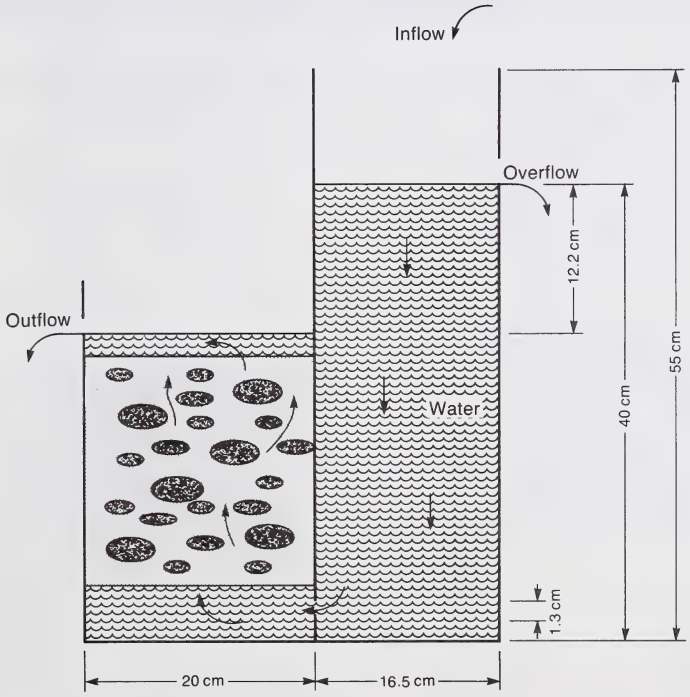

Figure 48. *Permeameter used in physical flow experiments.*

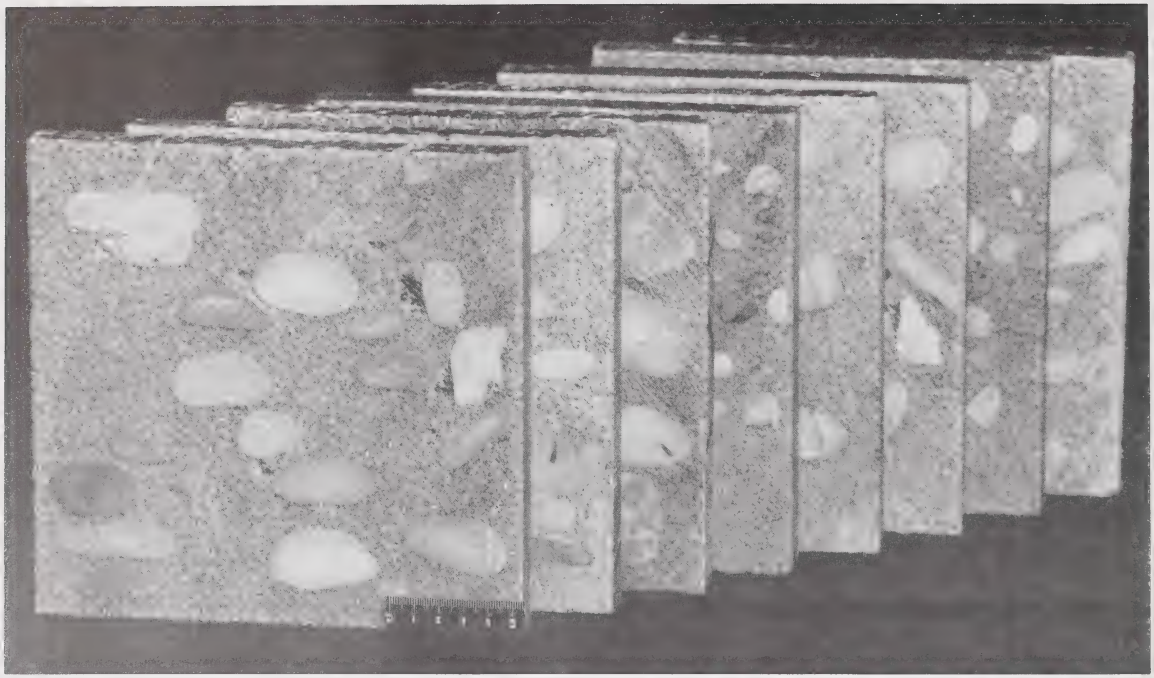

Figure 49. *Slabs from one of the physical analogue blocks.*

Table 6. *Effective permeabilities calculated using the FD method for simulated 3D clast intervals ($k_{sh}/k_{ss} = 0.001$).*

Shale clast fraction	Number of clasts	Effective vertical permeability	Effective horizontal permeability
0.098	666	0.812	0.869
0.219	1355	0.623	0.721
0.310	2073	0.491	0.604
0.416	2829	0.378	0.482
0.511	3635	0.278	0.382
0.598	4483	0.203	0.293
0.656	5188	0.159	0.237
0.718	5350	0.114	0.182

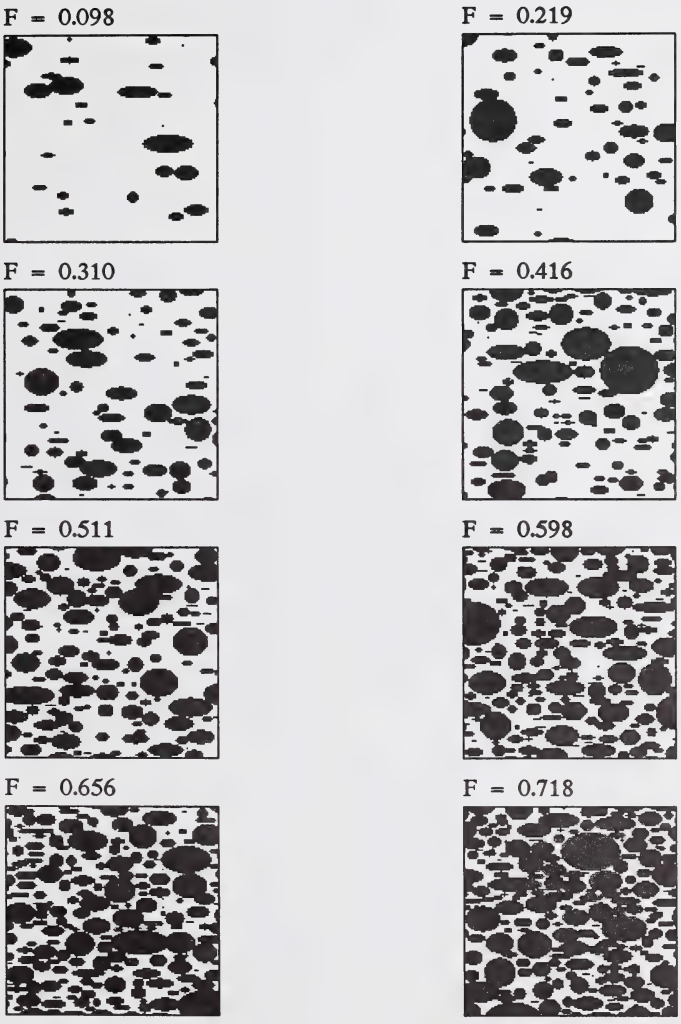

Figure 50. *Vertical section near the middle of each of eight simulated 3D clast intervals.*

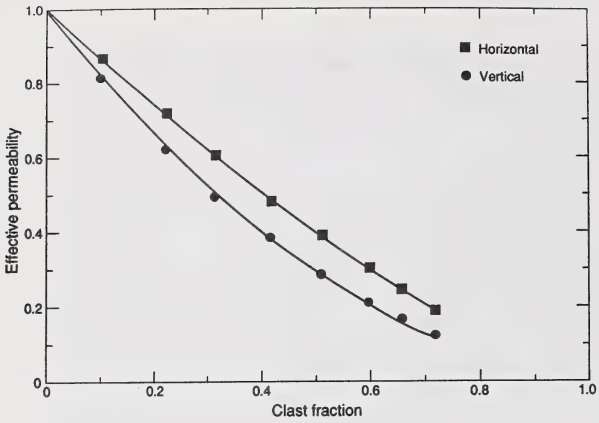

Figure 51. *Horizontal and vertical permeability computed for 3D simulated clast intervals. Generalized weighted mean fits (curves) have exponents 0.530 (vertical) and 0.734 (horizontal).*

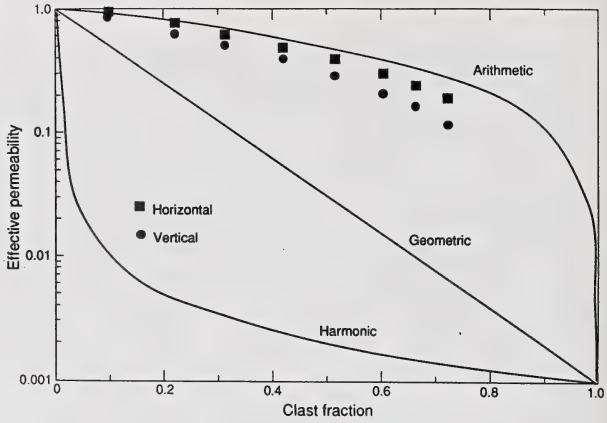

Figure 52. *Comparison of 3D simulation results for clasts with standard arithmetic, geometric, and harmonic mean predictions.*

provides excellent fits to the dimensionless effective permeabilities in Figure 51. In equation (17), k_{sh} and k_{ss} are the shale and sand permeability, respectively, f is the shale clast fraction, and ω is an exponent found by least-squares fitting. For the 3D numerical cases, (k_{sh}/k_{ss}) has the value 0.001 and the values of ω for horizontal and vertical effective permeability are, respectively:

$$\omega_h = 0.734 \; ; \; \omega_v = 0.530$$

The generalized weighted mean fits, shown in Figure 51, are characterized by R^2 = 0.99999 for the horizontal data points and R^2 = 0.9993 for the vertical. The generalized weighted mean model provides a smooth interpolation between the standard arithmetic, geometric, and harmonic averages, which correspond to ω = 1, 0, and –1, respectively. The 3D simulation results lie between the geometric and arithmetic average predictions. Figure 52 compares the simulation results with the three standard averages and shows that substantial errors would be made by using any of the standard means to compute effective permeability.

Physical flow experiments were conducted to validate the numerical results. The effective permeabilities obtained from the experiments are shown in Figure 53 together with those of the numerical simulations. It is evident that the physical results are lower for all "clast" fractions; the typical difference (in relative terms) being about 10 – 15%. It might be supposed that this difference was caused by the differences in shape between pebbles and the oblate ellipsoids. However, results to be presented later show that small differences in shape have little impact on effective permeability. If the pebbles had lower aspect ratios on average than those of the ellipsoids, the physical analogues would be expected to have lower vertical permeability. However, the

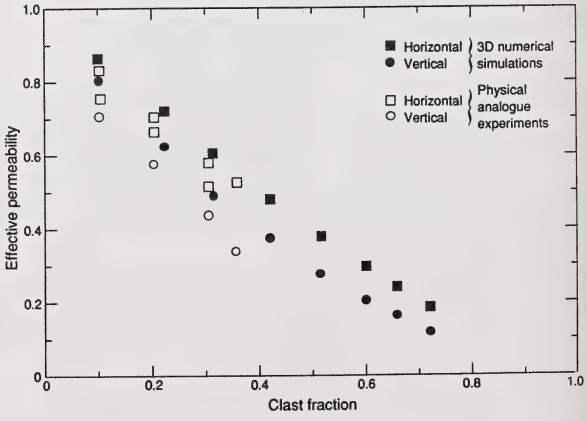

Figure 53. *Comparison of results from 3D numerical simulations with results from physical analogue experiments.*

horizontal permeability would be expected to be higher than that found in the numerical simulations. Instead, both vertical and horizontal permeabilities are lower for the physical analogues.

Based upon other, indirect validation of the 3D numerical calculations, the authors believe that the numerical results are more reliable than those from the physical experiments. Several experimental causes can be postulated for systematically low experimental permeability measurements. One is the possibility of trapped air in the consolidated blocks, causing reduced permeability due to two-phase flow (relative permeability) effects. Also, the emplacement of pebbles in the blocks might have affected the surrounding matrix permeability, thus affecting the comparison with the reference (pebble-free) blocks.

A number of 2D numerical flow simulations were performed at an earlier stage of the study using intervals of the actual digitized shale clast data. Comparing the results of these simulations with the results of the 3D calculations serves to test the reliability of the stereological method of determining 3D clast properties, and also demonstrates the effect of dimensionality (i.e., 2 versus 3) on effective permeability. The 16 shale clast intervals shown in Figure 54 were used to perform the 2D flow simulations using a 2D version of the FD flow simulator. The intervals represent a range of shale clast fractions from less than 3% to nearly 50%. As much as possible, intervals were selected according to the criteria of: (1) reasonably uniform spatial distribution of clasts, (2) large numbers of clasts, and (3) no large clasts dominating or obstructing the flow. These criteria were based on visual inspection of the digitized intervals and were intended to ensure representativeness. In regions containing a few, large clasts, a core scale region is simply not large enough to provide a representative sample of clasts and therefore such regions were eliminated from consideration. Obviously, criteria (1) and (2) had to be relaxed in order to locate intervals with very low densities of clasts. It proved impossible to locate suitable intervals with higher shale clast fractions without violating criterion (3).

The simulations and their results are summarized in Table 7 and Figure 55. The grid sizes used for these simulations, typically about 400×400, were sufficient to provide good resolution of even the smallest, millimetre-sized clasts.

An independent check of the 2D numerical results was provided by electrical analogue experiments. These experiments were performed on two of the 16 intervals, with two independent replications in one case. Results of these measurements are shown for comparison in Table 7 and are in good agreement with the numerical results.

Results of the 2D numerical flow simulations were compared with results of simulations using 2D sections of the eight simulated 3D clast cases. Five planes of grid blocks were selected from each of the 3D cases, at distances of 20, 40, 60, 80, and 100 grid spacings from one vertical face of the $128 \times 128 \times 128$ grid. For each such plane, two 2D flow simulations were performed to calculate effective vertical and horizontal permeability. Figure 56 compares results of these synthetic 2D simulations with results for the actual shale clast cross sections. There is very good agreement, for both directions of flow and over the complete range of "clast" fractions. This can be interpreted in two ways. One interpretation is that it indirectly validates the procedure used to synthesize the 3D clasts. The 3D clast blocks were created to have similar 2D properties to real shale clasts and the similarity of the 2D flow properties appears to confirm this. However, one can also argue that the result shows that details of shape (the synthetic clasts being considerably smoother) have little effect on flow.

Two-dimensional flow simulations were also performed on the digitized pebble images from the slabs of blocks used in the physical flow experiments. In Figure 57, the results of these calculations are compared with those of the 16 actual shale clast cases. The 2D pebble clast permeability is systematically higher than that of actual shale clasts for both the vertical and horizontal directions. It is tempting to ascribe these differences to the generally smoother contours of the pebbles, compared with the shale clasts. However, the permeability of the synthetic sections of the oblate ellipsoidal clasts (also smooth) was much closer to that of the real shale clasts. One possible reason for the higher permeability of the 2D pebble clasts might be that the pebbles were not really distributed randomly, as were the real shale clasts and the ellipsoidal clasts.

It is instructive to compare the permeability reduction in two dimensions with that in three

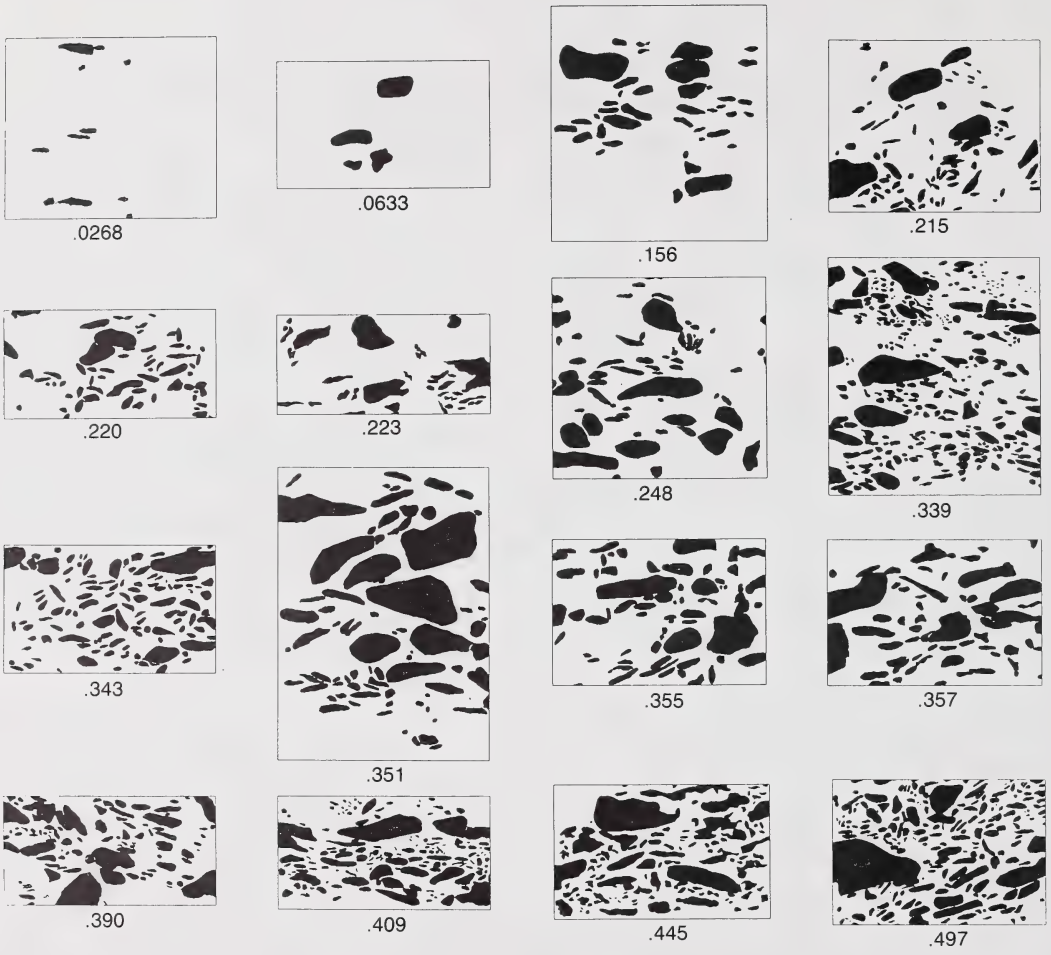

Figure 54. *Core scale intervals for which flow simulations were performed. The shale clast fractions are indicated below each interval.*

Table 7. *Effective permeabilities calculated using FD method for the clast intervals shown in Figure 54 ($k_{sh}/k_{ss} = 0.001$).*

Shale clast fraction	Effective vertical permeability	Effective horizontal permeability	Electrical analogue	
			vertical	horizontal
0.027	0.887	0.959		
0.063	0.845	0.885		
0.156	0.576	0.748	0.613	0.771
0.215	0.499	0.610		
0.220	0.478	0.571		
0.223	0.432	0.571		
0.248	0.406	0.561		
0.339	0.244	0.469		
0.343	0.261	0.451		
0.351	0.187	0.474	0.184, 0.182	0.486, 0.482
0.355	0.270	0.401		
0.357	0.166	0.439		
0.390	0.252	0.301		
0.409	0.171	0.385		
0.444	0.153	0.337		
0.497	0.129	0.256		

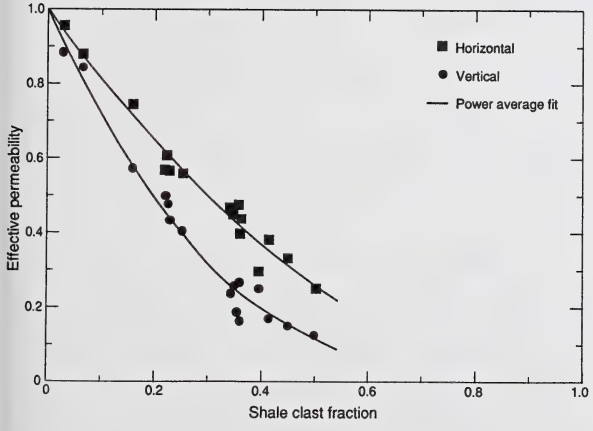

Figure 55. *Effective permeability of 2D clasts computed for the intervals shown in Figure 54. Generalized weighted mean fits (curves) have exponents 0.243 (vertical) and 0.486 (horizontal).*

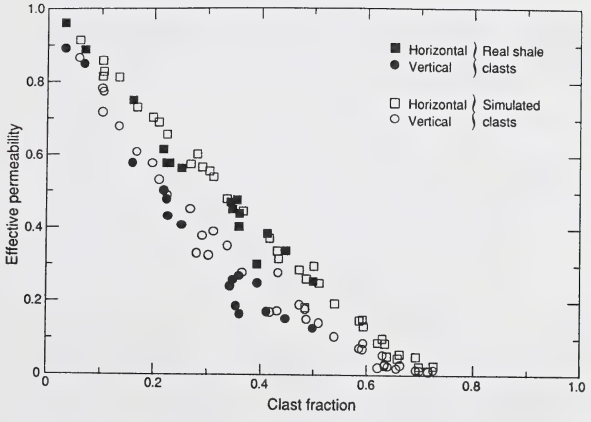

Figure 56. *Comparison of simulation results for real 2D clast sections with results for cross sections of simulated 3D clast sections.*

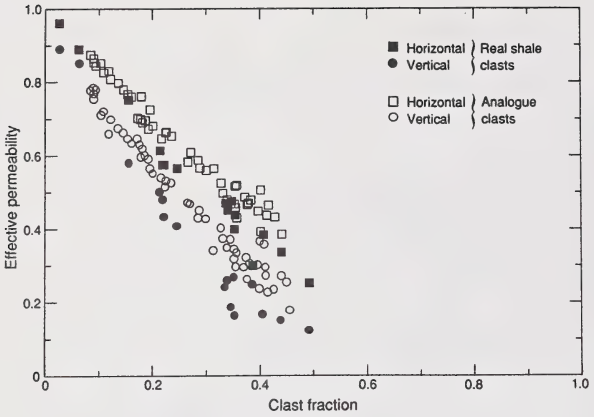

Figure 57. Comparison of simulation results for real 2D clast sections with results for cross sections of physical analogue pebble blocks.

dimensions. Figure 58 shows the 3D numerical simulation results and the 2D results for sections of the same 3D synthetic clast distributions. Permeability is reduced considerably more in 2D, for the same "clast" fraction, than it is in 3D. This expected result agrees with general arguments that have been advanced in the literature (Matheron, 1967; Gutjahr et al., 1978; Desbarats, 1987b)

Scaling Permeability Values Up to the Reservoir Grid Block Scale

The previous section has shown how the effective permeability of a core scale region can be estimated. For practical reasons, it is important to know the effective permeability of much larger regions—those corresponding to typical reservoir simulation grid blocks. If clasts were relatively uniformly distributed throughout a grid block, then the core scale results would apply directly to the larger scale of the grid block and Figure 51 would give the grid block permeability values. However, clasts are generally not distributed uniformly throughout shale clast zones, as previously discussed. Rather, they occur in distinct layers interbedded with layers of sand, and the volumetric density of clasts varies significantly within any particular layer. These characteristics need to be recognized in estimating permeabilities at the grid block scale.

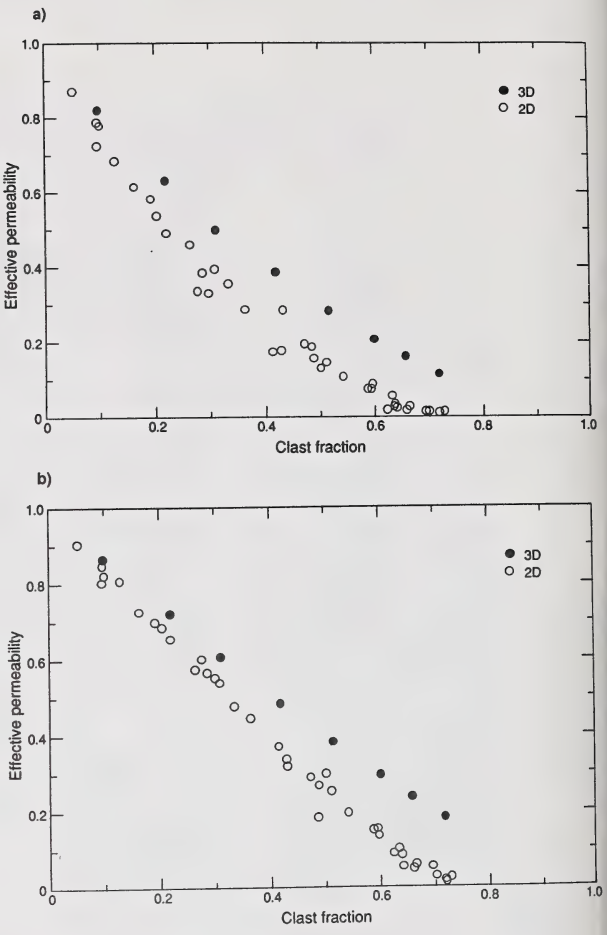

Figure 58. Comparison of effective permeability computed for 3D simulated clast cases with permeability for 2D sections of the 3D cases: (a) vertical; (b) horizontal.

Consider a region within a shale clast zone with dimensions of metres representing a reservoir simulation grid block. If this region is divided into cells with dimensions of 10–20 cm, then each cell corresponds to a core scale region and can be characterized using the results of the previous section. The array of cells or "fine grid" can be used as the discrete elements in flow simulations for the large grid block, and those simulations may be used to compute effective permeabilities of the large block (Lasseter et al., 1986). The entire process amounts to a scaling up; the core scale calculations produce values to be input to the grid

block calculations, which in turn provide grid block permeabilities for a reservoir simulation. Three different grid block sizes are involved: a grid spacing of millimetres or less at the core scale, a spacing of order 10 cm at the layer scale, and a spacing of order metres to tens of metres at the reservoir scale. This section focuses on the intermediate, grid block, or "layer scale" calculation.

Like the core scale calculation, the calculation of permeability at the larger grid block scale requires first that the variability associated with the heterogeneity be specified at this scale, then that flow is simulated to obtain an effective permeability. Because of the inaccessibility of large scale subsurface data describing the heterogeneity, the initial description of the variability requires a numerical approach, as does the flow simulation.

Simulating large-scale spatial characteristics of shale clast zones. Depending on the size of the grid block being considered, it may contain part or all of a single shale clast layer, or many shale clast layers. In either case, the lack of subsurface data means that assumptions are needed about the spatial distribution of shale clast fraction within a layer. Two types of layers may be considered:

- Type 1: Random variation. Shale clast fraction is assumed to vary completely randomly within the layer. That is, there is no correlation between the values at neighboring points.
- Type 2: Uncorrelated complete stratification. Shale clast fraction is laterally stratified. That is, shale clast fraction varies only vertically and not laterally within the layer. The vertical variation is assumed to have no spatial correlation.

For either idealized type of spatial variation, the statistical frequency of shale clast fraction values is assumed to follow some particular distribution. In all of the calculations reported here, the frequency distribution shown in Figure 40 was assumed. The two types of assumed spatial variation represent extremes. In reality, some horizontal and vertical correlation is to be expected but not complete stratification.

To simulate larger simulator grid blocks, the spatial distribution of shale clast layers must also be considered. As discussed earlier, individual shale clast layers cannot be correlated between wells. Layers are expected to extend laterally for metres to tens of metres and to have a greater extent parallel than perpendicular to the channel direction. Based upon core data (see Figure 39), layer thicknesses range from less than one metre to several metres. The spatial distribution of layers within a shale clast zone is assumed to be random. With this assumption, the shale clast layers are similar to the "stochastic" or "discontinuous" shales considered by other researchers (Haldorsen and Lake, 1984).

The configuration of layers within the grid block is created using a program that implements an algorithm from Haldorsen and Lake (1984). The program creates layers as rectangular parallelopipeds within a sand matrix. For simplicity, layers are considered to be square in plan view, but have a range of horizontal sizes and thicknesses. Starting with a sand-filled block, individual clast layers are added one at a time, each having a randomly chosen centroid. The horizontal and vertical dimensions of each new layer are selected from independent lognormal frequency distributions having specified means. A newly added layer is allowed to overlap existing layers by up to 10% of the volume of the new layer. This condition is tested before actually adding the layer, and if it is not met, a new position is chosen and the overlap retested. This procedure is repeated until the overlap condition is satisfied. New layers are added to the block until a specified fraction of the block is occupied by layers. As each layer is created within a region, a shale fraction distribution is assigned to its interior either in a spatially random manner for a Type 1 layer or in a stratified manner for a Type 2 layer. Examples of grid blocks having these two types of layers are illustrated in Figure 59. For both cases, the values of shale clast fraction were selected according to the frequency distribution in Figure 40.

Numerical flow simulation methodology. The finite difference flow simulation program used at the layer scale differs in only one significant way from the program used at core scale. The core scale program assumed that permeability for a particular grid block could have only two possible values, corresponding to sand and shale. By comparison, the layer model allows a finite number of possible permeability values for each grid block. Therefore, when creating the

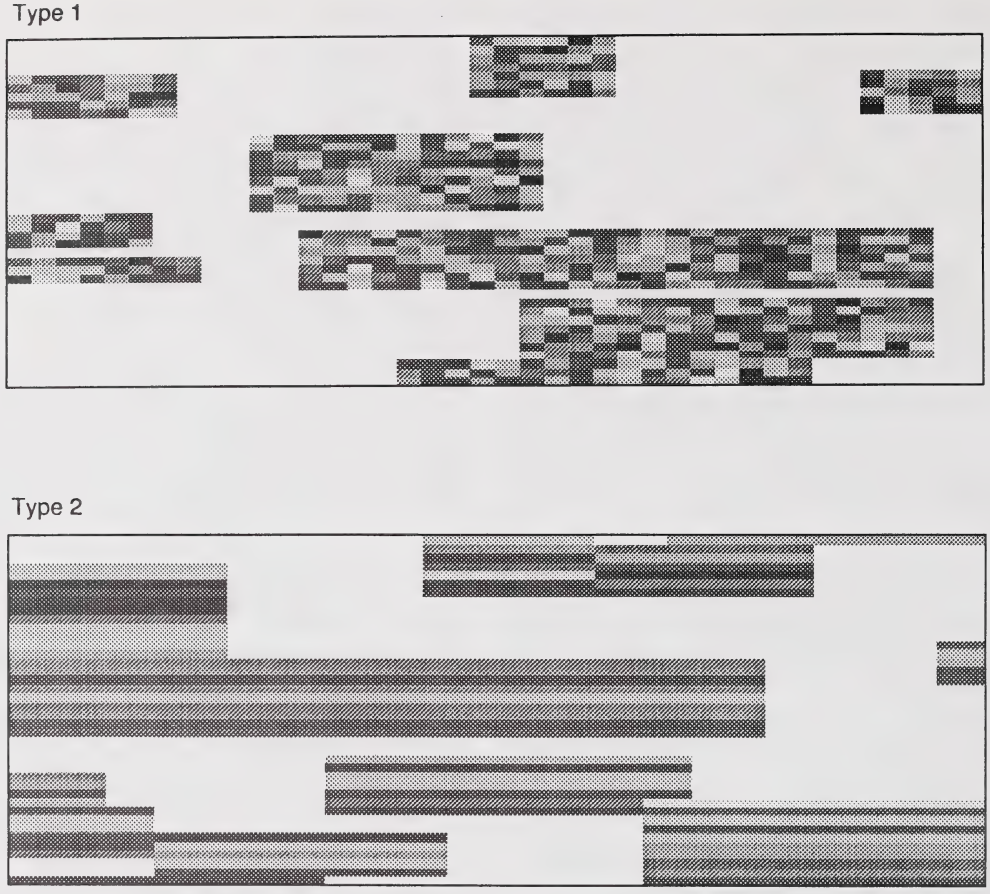

Figure 59. *Examples of cross sections from simulated clast layer distributions containing Type 1 and Type 2 layers.*

spatial distribution of shale clast fractions within a layer by the methods described above, only a discrete set of shale clast fractions were used. For example, all shale clast fractions between 0.20 and 0.25 were represented as 0.225 in the simulated layer. Correspondingly, only a finite set of core scale permeability values were assigned to the fine grid blocks constituting the layer. The model permits grid sizes of up to $80 \times 80 \times 80$ to be used and the grid blocks need not be cubes as they were with the core scale model. With grid blocks of dimensions 20 cm or more, regions with dimensions of tens of metres may be simulated.

A practical goal is to find methods of estimating grid block permeability based on observations in a well passing through the grid block. Others have addressed this goal (Haldorsen, 1989) by creating a number of equally possible synthetic grid blocks "conditioned" to the observations in a well or wells. A different approach—very much empirical rather than theoretical—was taken for this study. Synthetic grid blocks made up of arrays of small grid cells representing either of the two idealized types of layers were constructed. "Wells" through the grid block were considered after the grid block was constructed and represented simply as vertical columns of the small grid cells. Estimates of the grid block permeability were made by computing different averages over properties of the grid cells found in the synthetic "wells." Since true shale clast layers are not

known to be either Type 1 or Type 2, it was hoped to find an easily calculated well average that provided a reasonably good estimate of grid block permeability for either type of layer.

It is useful to distinguish two cases: (1) a reservoir grid block corresponding to a single shale clast layer, and (2) a large grid block (e.g., in a multiwell simulation) containing many layers of shale clasts interbedded with layers of sand. These "small grid block" and "large grid block" cases are discussed separately.

Permeability of a small reservoir grid block. In this case, the reservoir grid block to be characterized is assumed to lie entirely within a single shale clast layer. In the Provost Upper Mannville B Pool reservoir, shale clast layers are typically about one-metre thick (e.g., Figure 39). Therefore, simulations were carried out for a hypothetical grid block of rectangular parallelopipedal shape, having horizontal dimensions 5 m × 5 m and thickness 1 m. The fine grid size was 20 × 20 × 5. If the true layer were of Type 2, the estimation of permeabilities would be simple: vertical permeability would be the harmonic mean of the core scale values of vertical permeability obtained for the fine grid cells in the well; horizontal permeability would be the arithmetic mean of the horizontal permeability values obtained within the well. Therefore, only spatially random (Type 1) layers were simulated.

The synthetic wells were selected in a regular pattern with a spacing of five grid blocks in each lateral direction on the fine grid. Each of the wells was regarded as an independent sample of the layer, and various averages were computed for each such sample. Since the grid was five grid cells deep, each average was computed using five values from grid cells in the well. The vertical flow results for one synthetic layer are summarized in Table 8.

Similar results are summarized in Table 9 for horizontal flow in the same synthetic block.

There is of course a great deal of statistical variation between the estimates from different "wells." This is inevitable given the small sample size of five used to compute each average. To evaluate the usefulness of a particular estimation method, it is appropriate to look at the final two rows of Tables 8 and 9, which give the averages and standard deviations over all the wells. The deviations of these averages from the true permeability for the block are a measure of the average error expected for many such estimates of permeability. Of the standard averages (the first three well columns), the arithmetic mean provides the best estimate of block permeability for both the vertical and horizontal directions. However, the "core scale" estimates, CSV and CSH, are nearly as good. The latter estimates are much easier to apply in practice since they require only a value for the average shale fraction in the well, combined with the core scale results (Figure 51). Other independently simulated layers produced the same conclusions.

The above discussion assumed a Type 1 layer. If, instead, each of the wells in the above case was considered as a sample from an independent, stratified

Table 8. *Estimates of vertical permeability of a synthetic layer based on wells (vertical columns of grid cells) through the layer. Calculated vertical permeability for the layer = 0.346. (AV, arithmetic mean of vertical permeability values from well grid cells; GV, geometric mean of vertical permeability values in well; HV, harmonic mean of vertical permeability values in well; CSV, core scale estimate of vertical permeability (Figure 51) based on the arithmetic average shale fraction in the well).*

Well	Permeability estimate			
	AV	GV	HV	CSV
1	0.439	0.432	0.426	0.436
2	0.359	0.347	0.333	0.353
3	0.351	0.332	0.314	0.342
4	0.307	0.271	0.245	0.289
5	0.368	0.361	0.353	0.365
6	0.303	0.272	0.239	0.289
7	0.333	0.305	0.279	0.320
8	0.383	0.368	0.352	0.376
9	0.402	0.372	0.343	0.388
10	0.331	0.331	0.330	0.331
11	0.256	0.241	0.226	0.249
12	0.242	0.237	0.232	0.240
13	0.261	0.257	0.253	0.259
14	0.388	0.361	0.329	0.376
15	0.379	0.373	0.367	0.376
16	0.316	0.302	0.287	0.310
Mean	0.339	0.323	0.307	0.331
St. Dev.	0.054	0.054	0.056	0.054

Table 9. Estimates of horizontal permeability of a synthetic layer based on wells (vertical columns of grid cells) through the layer. Calculated horizontal permeability for the layer = 0.449. (AV, arithmetic mean of horizontal permeability values from well grid cells; GV, geometric mean of horizontal permeability values in well; HV, harmonic mean of horizontal permeability values in well; CSV, core scale estimate of horizontal permeability (Figure 51) based on the arithmetic average shale fraction in the well).

Well	Permeability estimate			
	AV	GV	HV	CSV
1	0.543	0.538	0.533	0.542
2	0.465	0.456	0.446	0.463
3	0.455	0.441	0.428	0.452
4	0.406	0.378	0.357	0.398
5	0.475	0.470	0.464	0.474
6	0.404	0.379	0.353	0.398
7	0.436	0.414	0.394	0.430
8	0.488	0.477	0.465	0.485
9	0.502	0.480	0.459	0.496
10	0.441	0.440	0.439	0.441
11	0.359	0.347	0.335	0.356
12	0.347	0.343	0.339	0.346
13	0.367	0.364	0.361	0.366
14	0.490	0.469	0.446	0.485
15	0.486	0.482	0.478	0.485
16	0.422	0.411	0.399	0.419
Mean	0.443	0.431	0.418	0.440
St. Dev.	0.054	0.055	0.056	0.054

(Type 2) layer, then the true permeabilities for the layer represented by each well would simply be the values in columns HV of Table 8 and AV of Table 9 as a consequence of stratification. Suppose, however, that the core scale estimates CSV and CSH were used in this case as well. Comparing these estimates with the true (HV and AV) values, the average error is about 5%. Therefore, based on the shale clast fraction distribution assumed in these simulations (from well B), the estimates CSV and CSH represent practical estimates with acceptable accuracy for either Type 1 or Type 2 layers. In other words, the variability in shale clast fraction within a layer is sufficiently small that the core scale permeability estimates can be applied at this larger scale.

Permeability of a large reservoir grid block. Large reservoir grid blocks are assumed to contain many shale clast layers interbedded with layers of sand. For example, the block might include the entire interval through the shale clast zone in Well B (Figure 39).

To perform flow simulations for a single large grid block, the same numerical flow model described previously for the small grid block calculations was utilized. The only difference was that a larger grid was needed to incorporate a number of shale clast layers within the block. Specifically, the example considered here is a grid block 8-m thick and 24 × 24 m laterally. Adequate resolution can be obtained using a 40 × 40 × 40 grid within this block. Shale clast layers were created on the grid by the discrete method described in the section "Simulating large scale spatial characteristics of shale clast zones."

As in the case of the single layer grid block calculations, a number of vertical "wells" were sampled for each synthetic grid block and various averages were computed for each such well. There were 64 sample wells in each block, spaced equally at five grid cell intervals in both horizontal directions. Each consisted of a vertical column of 40 grid cells and all well averages were computed from values in those 40 cells.

Table 10 presents the results of vertical permeability calculations for 12 simulated grid blocks, six containing only layers of Type 1 and six containing only Type 2 layers. Different mean layer sizes were chosen for different simulations but layer thicknesses in all 12 simulations were lognormally distributed with a mean of 0.7 m. Cases were constructed in which "clast" layers occupied either 0.3 or 0.5 of the entire block, the remainder being occupied by sand. The abbreviations for the well averages in Table 10 are the same as those used previously (Tables 8 and 9), with the addition of "Zone Harmonic Mean of Vertical" or ZHMV. The latter is obtained by combining all of the shale clast layers in the well together and computing a vertical permeability for the combined layers based on their overall average shale clast fraction and the core scale prediction of Figure 51. Then the harmonic mean is computed of this value and the value for sand (1 in normalized units), weighted by the respective fractions of shale clast layers and sand layers in the well (for example, if 25 of the well cells were within clast layers and 15 within sand, the relative weightings would be 25 and 15).

Table 10. *Computed vertical permeability of simulated large grid blocks and averages estimated from vertical "wells" through the blocks. Well averages were computed for each of 64 wells, then averaged over all wells. k_{eff} is the calculated dimensionless vertical permeability of the block. "Zone fraction" represents the fraction of the block occupied by shale clast layers. Well averages are defined in text.*

Block	Layer type	Layer size (m)	Zone fraction	k_{eff}	Well averages			
					AV	GV	HV	ZHMV
1	1	4	0.3	0.677	0.793	0.705	0.591	0.624
2	1	4	0.5	0.613	0.744	0.644	0.526	0.563
3	1	8	0.3	0.652	0.810	0.725	0.608	0.645
4	1	8	0.5	0.520	0.663	0.563	0.465	0.499
5	1	12	0.3	0.646	0.804	0.714	0.592	0.626
6	1	12	0.5	0.525	0.667	0.567	0.468	0.501
7	2	4	0.3	0.664	0.806	0.720	0.605	0.638
8	2	4	0.5	0.601	0.757	0.664	0.555	0.583
9	2	8	0.3	0.633	0.806	0.719	0.605	0.636
10	2	8	0.5	0.474	0.676	0.566	0.455	0.491
11	2	12	0.3	0.544	0.774	0.666	0.523	0.576
12	2	12	0.5	0.473	0.688	0.591	0.488	0.524

In all cases, the ZHMV average provides an estimate within about 10% of the computed effective permeability of the block, when averaged over all observation wells. The estimate is usually low for Type 1 layers and high for Type 2 layers and therefore seems to be a practical compromise when the true layer type is unknown. It is easy to estimate in a practical case since it requires only values for the fraction of the well occupied by layers and the average shale clast fraction within layers. Furthermore, this average reduces to the CSV average suggested for single layer grid blocks when the fraction of the grid block occupied by shale clast layers approaches unity.

Table 11 presents similar results for horizontal permeability of the same 12 simulated blocks. Again the abbreviations for well averages are as before except for the "Zone Arithmetic Mean of Horizontal" or ZAMH, which has the following meaning. All clast layers in the well are combined together and a horizontal permeability computed for them based on their average shale clast fraction and the core scale predictions (Figure 51). Then the arithmetic mean is computed of this value and the value for sand (1 in normalized units), weighted by the fractions of shale clast layers and sand layers in the well. In all cases the ZAMH average provides a very good estimate of block permeability, when averaged over many wells. Like the ZHMV, it is easy to calculate or estimate in practice.

Sample grid block calculations. The characterization of shale clast flow units for the composite example well illustrated in Figure 29 provides a practical illustration of the averaging methods described above. The upper layer of shale clasts in this well has approximately 40% shale clasts by area, as observed in core. Applying the core scale estimates of Figure 51 to this layer (as suggested above), the effective horizontal and vertical permeability of the layer are given by 0.5 and 0.4, respectively, of the permeability of sand. The sand permeability can be taken from the blocky channel sand flow unit separating the two shale clast flow units; this sand unit has horizontal permeability 3843 md and vertical permeability 3328 md. The numerical calculations of this report have assumed that the permeability of the sand matrix was isotropic. However, a reasonable extension of the numerical results simply applies the vertical reduction factor (0.4) to the vertical permeability of sand (3328 md) and the horizontal reduction factor (0.5) to the horizontal permeability of sand (3843 md). This produces values:

Table 11. *Computed horizontal permeability of simulated large grid blocks and averages estimated from vertical "wells" through the blocks. Well averages were computed for each of 64 wells, then averaged over all wells. k_{eff} is the calculated dimensionless horizontal permeability of the block. "Zone fraction" represents the fraction of the block occupied by shale clast layers. Well averages are defined in text.*

Block	Layer type	Layer size (m)	Zone fraction	k_{eff}	Well averages			
					AH	GH	HH	ZAMH
1	1	4	0.3	0.826	0.826	0.771	0.701	0.825
2	1	4	0.5	0.777	0.784	0.721	0.646	0.782
3	1	8	0.3	0.827	0.840	0.787	0.717	0.839
4	1	8	0.5	0.710	0.717	0.653	0.587	0.715
5	1	12	0.3	0.828	0.835	0.778	0.704	0.834
6	1	12	0.5	0.714	0.719	0.656	0.589	0.718
7	2	4	0.3	0.831	0.837	0.783	0.714	0.836
8	2	4	0.5	0.784	0.796	0.737	0.669	0.795
9	2	8	0.3	0.825	0.836	0.782	0.713	0.835
10	2	8	0.5	0.706	0.726	0.654	0.580	0.723
11	2	12	0.3	0.811	0.808	0.739	0.650	0.806
12	2	12	0.5	0.719	0.738	0.675	0.608	0.736

$$k_h = 1922 \text{ md}; k_v = 1331 \text{ md}$$

for the permeability of the upper shale clast layer flow unit.

The bottom shale clast flow unit in the composite example well (Figure 29) actually consists of two layers of shale clasts, one containing 40% clasts and the other 10% clasts, separated by a layer of sand. The two shale clast layers each occupy 0.4 of the interval while the sand layer makes up the remaining 0.2 of the interval. Since it contains several distinct layers, this flow unit is treated by the methods described in "Permeability of a large reservoir grid block." The combined shale clast sublayers have an average shale clast fraction $(0.4 \times 0.4 + 0.4 \times 0.1)/0.8 = 0.25$. This shale clast fraction leads to core scale effective permeability $k_h = 0.67$ and $k_v = 0.58$ (Figure 51). The average ZAMH, which provides an estimate of horizontal permeability for the flow unit, is given by $0.8 \times 0.67 + 0.2 \times 1 = 0.7360$, where the two terms correspond to shale clasts and sand, respectively. The appropriate average to estimate vertical permeability of the flow unit is ZHMV, calculated by $1/ZHMV = 0.8/0.58 + 0.2/1 = 1.579$, or $ZHMV = 0.6333$. Again, to convert these dimensionless permeability reductions to actual permeability of the flow unit, they are multiplied by the horizontal and vertical components of sand permeability (3843 md and 3328 md, respectively). The resulting permeability values for the lower shale clast layer flow unit are:

$$k_h = 2828 \text{ md}; k_v = 2108 \text{ md}$$

Generalizations to Other Types of Heterogeneity

The results presented so far in this chapter relate to the observed shale clast zones in the Provost Upper Mannville B Pool reservoir. To increase the applicability of these results, it is useful to extend them to other geometries and other types of heterogeneity. Since the numerical flow model has proven to be stable, reliable, and accurate, it provides an ideal vehicle for generalizing the results.

Shale fraction appears to be the most important factor determining the permeability of a region containing a binary heterogeneity like shale/sand. Accordingly, most of the results have been presented in terms of this variable. The fact that vertical and horizontal permeabilities of shale clast intervals are different suggests that aspect ratio is also another primary factor influencing permeability. Real aspect ratios may range from nearly unity for clasts in some

reservoirs to very low values for large shale lenses. The ratio of shale to sand permeability is also expected to have a large impact on effective permeability, since, as the ratio tends to unity, the permeability must approach that of sand, no matter what the distribution and density of shales. For real shales in sand, the ratio is nearly always very small and the shales behave as if they were essentially impermeable. However, larger permeability ratios are of interest for the physically analogous case of heat conduction in binary geological structures since the thermal conductivity ratio is generally much closer to unity. Heat transfer processes are of practical interest for in-situ thermal recovery processes.

It is also worthwhile to consider the effects on permeability of the shapes of the heterogeneities since real shales may range from approximately elliptical to much more rectangular. Besides the primary variables, more subtle characteristics, such as the distribution of sizes and the distribution of aspect ratios, may affect the permeability of a sand/shale system.

This section examines the influence of a number of characteristics of binary heterogeneities by means of numerical flow simulations. In each case, the shale clast results already obtained in the previous section are used as a "baseline" reference for comparative purposes.

Effect of aspect ratio. Different sand/shale systems are characterized both by different average aspect ratios and by different statistical distributions of aspect ratio among the shales. Both of these factors may influence the flow characteristics of the system. The statistical distribution of aspect ratio will be considered first.

The baseline clast simulations utilized the aspect ratio distribution (based on core observation) shown in Figure 42b. In order to construct a dramatically different distribution, the clast creation program was modified to produce all of the clasts (oblate ellipsoids) with the same aspect ratio. That is, the distribution of Figure 42b was replaced with a δ-function distribution. In order to compare with the baseline results, the aspect ratio was chosen to be 0.54, the mean of the earlier distribution. In addition, the same distribution of sizes was used as for the baseline case.

Figure 60 compares the results for a number of cases with fixed aspect ratio and varying shale fraction with those from the baseline simulations (Figure 51). Both horizontal and vertical permeability are virtually unchanged by this change in the distribution of aspect ratios. In predicting the effective permeability, only the average aspect ratio appears to be important.

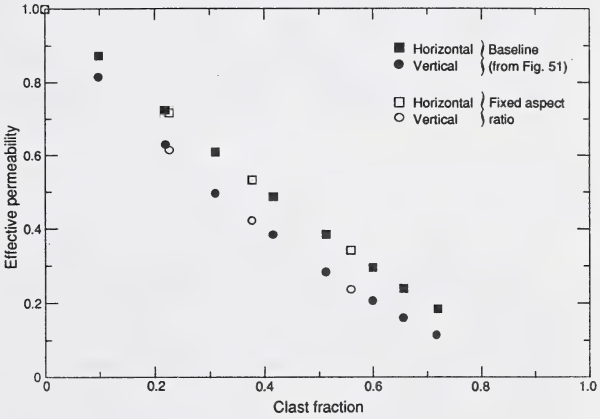

Figure 60. *Comparison of effective permeability for clasts having a realistic aspect ratio distribution (baseline) with effective permeability for clasts all having the same aspect ratio (0.54).*

Now consider the effect of different average aspect ratios. Based on the above results, only cases having a δ-function distribution of aspect ratios (i.e., having the same aspect ratio for all of the shales) are considered. In order to isolate the effects of aspect ratio, the same (baseline) size distribution is used for all of the simulations.

An important special case is that having aspect ratio unity; this is the idealized isotropic case of spherical heterogeneities. For this case, synthetic samples were created directly, using a slightly modified version of the clast creation program. However, to simulate aspect ratios smaller than those of the real clasts, a different strategy was employed. This strategy is based directly on the differential equation governing the flow (equation (16)). With

the assumptions made here—primarily the assumption that heterogeneities are always oriented horizontally—the permeability tensor reduces to horizontal and vertical components and the flow equation may be written:

$$(18)\quad \frac{\partial}{\partial x}\left(k_h \frac{\partial P}{\partial x}\right)+\frac{\partial}{\partial y}\left(k_h \frac{\partial P}{\partial y}\right)+\frac{\partial}{\partial z}\left(k_v \frac{\partial P}{\partial z}\right)=0$$

where k_h is the local horizontal permeability (that is, it is different in sand and shale) and k_v is the local vertical permeability. Suppose now that a re-scaling is applied to the coordinate system, replacing x, y, and z by:

$$(19)\quad x' = cx\ ;\ y' = cy\ ;\ z' = z$$

In terms of the new coordinates, all horizontal dimensions, and in particular the sizes of features in the x and y directions, are "stretched" by the factor c. Expressed in terms of these new coordinates, equation (18) becomes:

$$(20)\quad \frac{\partial}{\partial x'}\left(c^2 k_h \frac{\partial P}{\partial x'}\right)+\frac{\partial}{\partial y'}\left(c^2 k_h \frac{\partial P}{\partial y'}\right)+\frac{\partial}{\partial z'}\left(k_v \frac{\partial P}{\partial z'}\right)=0$$

In the new coordinate system, the horizontal permeability, k_h, is effectively increased by a factor c^2. This mathematical result may be used in simulating different aspect ratios. For example, consider a simulated region containing spheres and having a permeability anisotropy K_h/K_v = 1/4 within both the sand and the shale. If the coordinate transformation (19) is performed with c = 2, the system becomes one of oblate ellipsoids with aspect ratio 0.5 and permeability ratio K_h/K_v = (1/4) × 4 = 1, that is, an isotropic case with reduced aspect ratio.

Using this technique, simulations were performed for ellipsoids with aspect ratio 0.2 and 0.1. Results of these simulations are shown in Figure 61 together with generalized weighted mean fits to each set of points. The exponents, ω, of the fits are presented separately in Table 12.

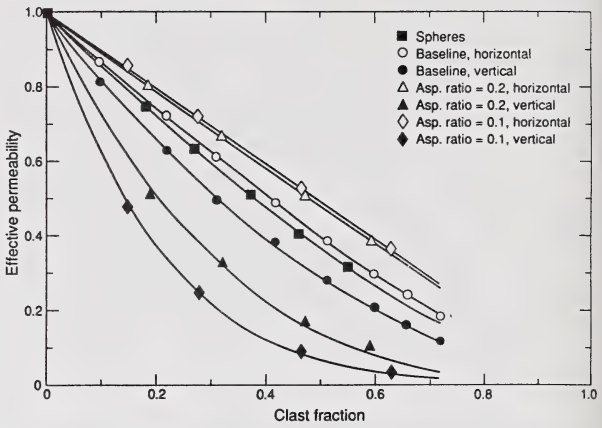

Figure 61. *Effective permeability for clast distributions having different aspect ratios.*

Table 12. *Generalized weighted mean exponents for different aspect ratios computed using a 3D numerical model.* (k_{sh}/k_{ss} = 0.001)

Aspect ratio	ω_v	ω_h
1.0	0.671	0.671
0.54	0.530	0.735
0.2	0.272	0.918
0.1	0.116	0.952

For randomly distributed spherical "clasts," the horizontal and vertical permeabilities are of course identical. As the aspect ratio is reduced, the difference between horizontal and vertical permeability increases and horizontal permeability approaches the arithmetic mean prediction (ω = 1). For aspect ratios 0.1 and lower, the arithmetic mean can safely be used to predict the horizontal permeability. However, the harmonic mean (ω = –1) is still a rather poor approximation to the vertical permeability for aspect ratio 0.1.

Results for aspect ratio 0.1 are compared in Figure 62 with results for a similar case obtained by Deutsch (1989). Deutsch simulated the case of randomly placed disks having a circular horizontal cross section and diameter 10 times their thickness. Agreement between his results and those obtained here is very good for both horizontal and vertical permeability.

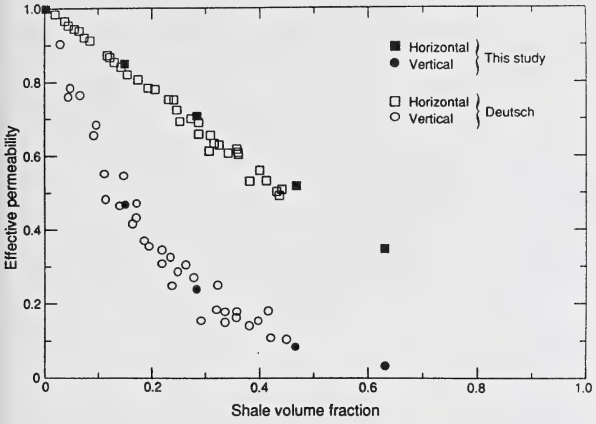

Figure 62. *Comparison of results for aspect ratio 0.1 with those of Deutsch (1989).*

Effect of shale permeability. For real shale and sand, the ratio k_{sh}/k_{ss} can nearly always be assumed to be very small—less than, say 0.001. However, higher ratios are of interest for other types of heterogeneity, in particular for the analogous problem of heat transport. Therefore, a set of simulations was conducted in which this ratio was varied from the value 0.001 heretofore assumed. Figure 63 shows the results of simulations for the same shale configuration (the 3D baseline case having shale fraction 0.416) in which permeability ratio k_{sh}/k_{ss} was varied from 0.0001 to 0.4.

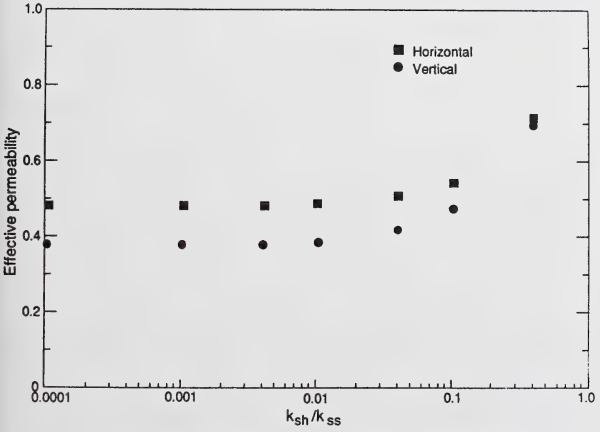

Figure 63. *Dependence of effective permeability on ratio of shale to sand permeability for a simulated 3D interval.*

Effective permeability does not change significantly as the permeability ratio k_{sh}/k_{ss} is reduced below about 0.01. This asymptotic behavior justifies the assumption made in many of the numerical calculations that a ratio k_{sh}/k_{ss} = 0.001 effectively represents impermeable shales.

Effect of clast shape. Results presented in the section discussing core scale permeability suggest that small variations in the shape of the shale clasts have little effect on permeability. For example, 2D sections of 3D mathematically simulated clast intervals and real 2D clast intervals had very similar effective permeability for the same clast fraction, even though the latter appear considerably rougher than do their synthetic counterparts.

A more extreme change in shape is represented by the difference between oblate ellipsoidal clasts and rectangular parallelopipedal clasts. The synthetic clast generation program was modified to produce rectangular parallelopiped shapes rather than ellipsoids, and flow simulations were conducted for various shale fractions. For comparison with the baseline clast (oblate ellipsoid) results, the parallelopipeds were constructed with the same x and y dimensions, the same size distribution, and the same aspect ratio distribution as the ellipsoids.

The results for parallelopipeds are compared with those for clasts in Figure 64. This significant change in shape has surprisingly little effect on permeability.

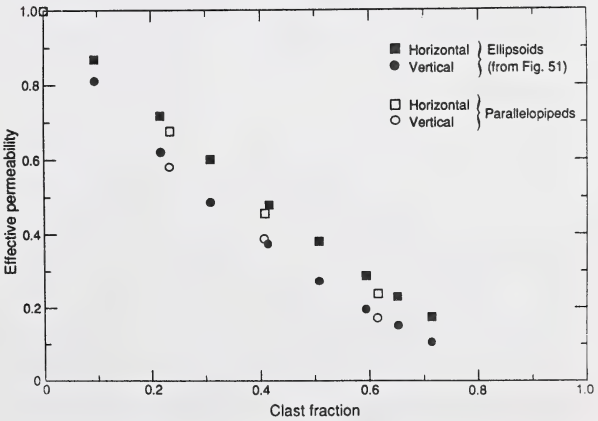

Figure 64. *Comparison of effective permeability for ellipsoidal clasts (from Figure 51) and parallelopipedal shales having the same distributions of size and aspect ratio as real shale clasts .*

Effect of clast size distribution. The baseline simulations assumed that clast sizes were distributed according to the lognormal frequency distribution given in equation (11). Sensitivity to this assumption can be tested by choosing different size distributions. As an extreme case, a δ-function distribution with all clasts having identical size was considered. The size was chosen to be the mean size used in the baseline clast simulations. For the first set of simulations, aspect ratios were distributed as they were for the baseline cases (i.e., Figure 42b). The results are shown in Figure 65. The effect of size distribution appears to be very small, at least over the range of shale fractions (less than about 0.6) commonly encountered in the field.

Another set of simulations was performed in which both size and aspect ratio were fixed at their baseline mean values. Figure 66 compares the results of these simulations with those of the baseline case (Figure 51). The small differences shown in this figure suggest that only the average size and aspect ratio are critical in determining effective permeability.

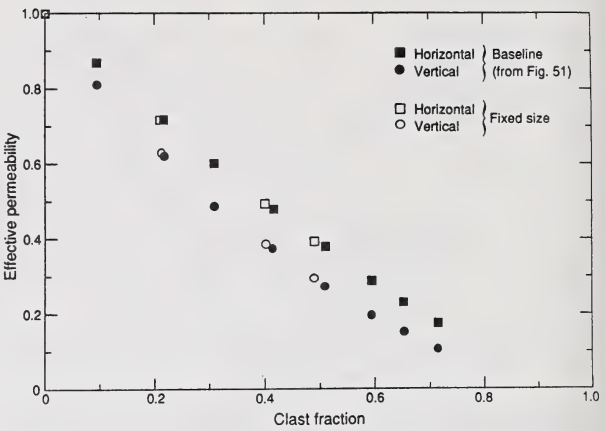

Figure 65. *Effective permeability of simulated clast intervals having a realistic distribution of clast sizes and having a single size. The aspect ratio distribution of Figure 42b is used for both cases.*

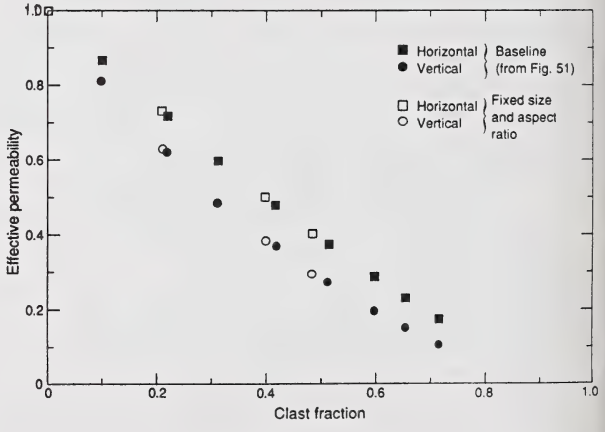

Figure 66. *Comparison of effective permeability for clasts having realistic distributions of size and aspect ratio with clasts that all have the same size and aspect ratio.*

Core Scale Effective Parameters in Transient Fluid Flow

The previous chapters of this report regarding the characterization of the heterogeneous shale clast facies have dealt with the issue of defining and estimating, at various scales, the values of effective permeability for the case of steady-state flow conditions (i.e., flow rates constant in time). However, steady-state flow is very seldom used in reservoir process simulations or encountered in reality during reservoir exploitation. The flow rates (injection, extraction) vary, and it is necessary to assess if the effective permeability values during transient flow are the same with the ones estimated for steady-state conditions. If the transient and steady-state effective values are not equal, then the question becomes how can they be estimated, and what is the error in using steady-state values for transient flow conditions.

Few studies to date have dealt with the problem of transient flow in heterogeneous porous media. Warren and Price (1961) and Dagan (1982) have shown that the value of effective permeability during transient flow is variable and different from its steady-state value. For this reason, it is very difficult, if not impossible, to compute the effective values of permeability and compressibility during transient fluid flow. The approach used by Warren and Price

(1961) of simulating a pressure build-up and computing an effective value for permeability using a Horner-type plot assumes a constant value during transient flow. The perturbation method used by Dagan (1982) is valid for the limiting case of early time, and has more theoretical than practical value. For these reasons, a different approach was adopted here. Using a numerical experiment approach, finite element simulations were used in this study to determine effective values for both transport and accumulation terms (permeability and compressibility) during transient fluid flow. The finite element method was used in the transient-flow simulations instead of the finite differences method because the finite differences code used so far was developed to handle only steady-state flow. The finite elements code FE3DGW (Gupta et al., 1984), readily available, was used for the transient-flow simulations. As mentioned previously, for the same accuracy, the finite element method requires far less grid nodes than the finite differences method, but this advantage in computer resources is sometimes more than offset by the manpower resources needed in setting up the finite element grid. Also, manually setting up a 3D finite element grid for the synthetic oblate spheroid clasts is very difficult if not impossible, while developing an automatic procedure would have required an unwarranted large effort. For this reason, the transient flow simulations were run for a single 2D case of actual heterogeneity from core.

Considering only saturated flow of a slightly compressible fluid (water), the macroscopic-scale flow through any core region is described by the equations (Peaceman, 1977):

$$(21)\quad \bar{v} = -\frac{k}{\mu}\left(\nabla p - \rho \bar{g}\right)$$

$$(22)\quad \nabla \cdot \bar{v} + \phi c \frac{\partial p}{\partial t} = 0$$

where p is pressure, k is permeability, $\bar{v}$ is specific flow rate, ϕ is porosity, μ is viscosity, ρ is density, $\bar{g}$ is the gravity vector, c is compressibility, and t is time. By applying constant but different pressures on any pair of opposite sides of a core region, and considering the other two sides as impervious, in effect a permeameter is simulated numerically, allowing for the computational measurement of the flow rate Q, therefore of the specific flow rate v. In the simulations, the liquid density ρ and viscosity μ are considered constant. The obvious advantage of the numerical experiments is that any parameter or boundary condition can be changed individually, allowing for the systematic investigation of various effects.

The numerical simulations are based on the geometry of the core region characterized by a shale clast fraction of 0.351 (Figure 54), which was described by a 966-nodes finite element grid. Different situations of heterogeneity were analyzed by assigning various parameter values to the shale clasts and the sand matrix. In order to differentiate the effects of variable permeability from the effects of variable compressibility, one parameter was considered as homogeneous and of equal value for both clasts and sand matrix, while the other was taken according to the clast distribution. The pressure p was assumed to be initially the same everywhere throughout the core region. For time $t > 0$, a sudden constant increase in pressure was imposed and maintained on one side, while the opposite side was maintained at the initial value. The other two sides were considered impervious. The numerical simulations were run until steady-state conditions were achieved, computing at every time step the input and output flows.

The flow behaviour is compared with the transient flow through the same core region characterized by the steady-state effective permeability k_{eff}, or by the arithmetic mean of the product (ϕc). The results are presented in dimensionless form as the variation in time of the specific flow rate, normalized with respect to its steady-state value. The time is normalized with respect to the characteristic time τ defined by:

$$(23)\quad \tau = \frac{\mu(\phi c)\, L^2}{k_{eff}}$$

where L is a characteristic length in the flow direction, in this case the dimension of the core region. The use of dimensionless variables allows the comparison of cases characterized by different parameters, geometry, and/or boundary conditions, as well as generalization of the results.

Figure 67 shows the variation in time of the input and output flows for the cases of heterogeneous permeability (k_{sh} and k_{ss}), and uniform homogeneous permeability equal to the steady-state effective value k_{eff}, for top to bottom and bottom to top flows. It can

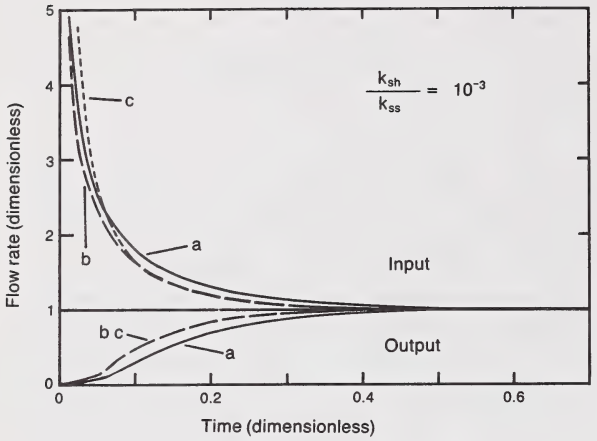

Figure 67. *Variation in time of the input and output flows through the core region with f = 0.351 shale clasts, for homogeneous porosity and compressibility and: (a) steady-state effective permeability k_{eff}, top to bottom flow; (b) heterogeneous permeability k_{sh} and k_{ss}, top to bottom flow; (c) heterogeneous permeability k_{sh} and k_{ss}, bottom to top flow.*

be seen that the effective permeability during slowly varying flow (discharge from the core region) is always greater than the steady-state value, toward which it decreases gradually (higher flow rate at outflow for the heterogeneous case than for the case of homogeneous steady-state value), as predicted theoretically by Dagan (1982). The numerical simulation of a pump test by Warren and Price (1961) corresponds to sudden and rapidly varying pressure gradients, similar to the ones at the inflow boundary of the core region simulated here. In this case, too, the transient effective permeability has higher values than the steady-state one (accordingly higher flow rate) for very early times. However, during middle to late times of the transient flow, the situation is reversed and the effective permeability has smaller values than at steady-state (accordingly lower flow rate). The Horner-plot interpretation of the numerical pump test by Warren and Price (1961) corresponds to the middle and late times of the transient flow, hence their conclusion that the transient value of the effective permeability is about 10% less than the steady-state value.

Further examination of Figure 67 shows that the flow behaviour during transient is dependent on the flow direction, particularly during early time. In this case, for the same pressure drop, the input or output transient flows are not equal when the flow directions are top to bottom or bottom to top. Because the pressure gradients are significantly higher at input than at output, the differences are greater for input flows; nevertheless, they exist also for output flows. The explanation for this directional dependence resides in the non-uniform distribution of the shale clasts within the sand matrix. When the flow conditions change, the flow rate is controlled by the local value of effective permeability, which is determined by the local distribution of heterogeneities.

The variability in the accumulation term of equation (22) was treated previously only by Freeze (1975) and Dagan (1982). In his stochastic analysis, Freeze (1975) took into account individually the two components of the specific storage: porosity ϕ and compressibility c. Dagan treated them as a single parameter and has shown, using perturbation expansions, that for slowly varying flow, the corresponding effective value relaxes to its arithmetic mean value. The porosity and compressibility of the shale clasts and of the sand matrix vary in a small range, such that the shale-to-sand ratio of the term (ϕc) varies generally between 1 and 3. The case of $(\phi c)_{sh}/(\phi c)_{ss} = 2.5$ is considered here, for shale clasts and sand matrix having the same permeability. It is assumed a priori that the result of Dagan (1982) applies, and that the space average $(\phi c)_A$ can be used instead of the statistical mean. Figure 68 presents the variation in time of the dimensionless flow rates at input and output, for the case of shale and sand values for the term (ϕc) according to the clast distribution, and for the case of homogeneous value equal to the weighted average $(\phi c)_A$. Comparison of the variation of the flow rates in the two cases indicates that indeed the effective value of the term (ϕc) is time dependent and that it relaxes to its space-average value. The use of the space or arithmetic average as the effective value seems to be a good approximation for slowly varying flow (in this case, the output flow at all times, and the input flow at late times). For rapidly varying flow, the error in using the space average as the effective value for (ϕc) most probably depends on the ratio $(\phi c)_{sh}/(\phi c)_{ss}$.

As opposed to permeability, the term (ϕc) does not change its scalar character because of the

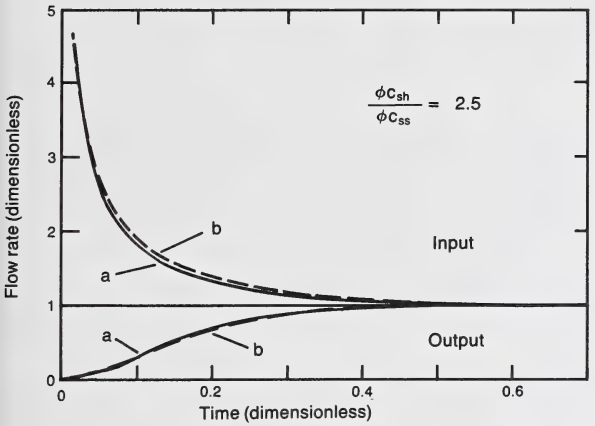

Figure 68. *Variation in time of the input and output flows through the core region with f = 0.351 shale clasts, for homogeneous permeability, and: (a) homogeneous space-average value $(\phi c)_A$ and (b) heterogeneous values $(\phi c)_{sh}$ and $(\phi c)_{ss}$.*

heterogeneities (an expected result given the form of the basic equation (22)). However, its effective value exhibits a dependence on the flow conditions similar to the dependence of the effective permeability during transient flow. To illustrate this point, Figure 69

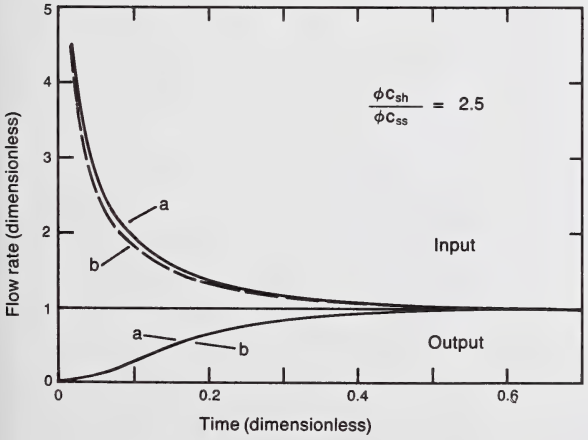

Figure 69. *Variation in time of the input and output flows through the core region with f = 0.351 shale clasts, for homogeneous permeability and heterogeneous porosity and compressibility, for: (a) vertical flow and (b) horizontal flow.*

presents the variation in time of the input and output specific flow rates for vertical and horizontal flow through the core region of characterized by a shale clast fraction of 0.351, for homogeneous permeability and heterogeneous porosity and compressibility. The difference in flow rates, more obvious for rapidly varying flow, reflects differences in the effective values of the term (ϕc).

The above numerical results confirm the theoretical results of Dagan (1982) that the effective value of the term (ϕc) is time dependent and that the arithmetic or space-average value represents a good approximation for the case of slowly varying flow. In addition, they show that the effective value is dependent on the flow conditions as well, but to a lesser extent than permeability.

In closing the subject of transient flow through core scale heterogeneous porous media, it must be stated that the use of values of steady-state effective permeability and space-average porosity and compressibility in the analysis of unsteady flow incorrectly predicts the actual flow rates. They are underestimated or overestimated, depending on the flow conditions and on the heterogeneity to matrix ratios of permeability and of the term (ϕc). For example, the use of steady-state permeability k_{eff} underestimates the output flow, but overestimates the input flow during middle and late transient times (Figure 67). In this case, $k_{sh}/k_{ss} < 1$. In the case of porosity and compressibility($(\phi c)_{sh}/(\phi c)_{ss} > 1$), use of the space-average value $(\phi c)_A$ has an opposite effect and overestimates the output flow, but underestimates the input flow (Figure 68). The error introduced by the use of steady-state effective permeability is greater, being probably related to the permeability contrast spanning three orders of magnitude, as opposed to the (porosity × compressibility) contrast of a factor of three. However, since the two errors in this case are in opposite directions, the net effect for the case simulated is an attenuated under or overestimation, as illustrated in Figure 70. The relative error is illustrated in Figure 71 as the ratio of the input or output flow rates computed with effective values, to the respective flow rates computed for the actual heterogeneity distribution. Although, for the simulated case, the relative errors seem large for the output flow and small for the input flow, one must take into account the fact that, in absolute value, the output and input flow rates are respectively very small and very large (Figure 70). Thus, the overall error could be significant at least during early times of transient flows.

The results presented so far have significant implications for the determination of reservoir characteristics using pump or drillstem tests, and for the deterministic predictive reservoir modelling in which single "equivalent" values are used.

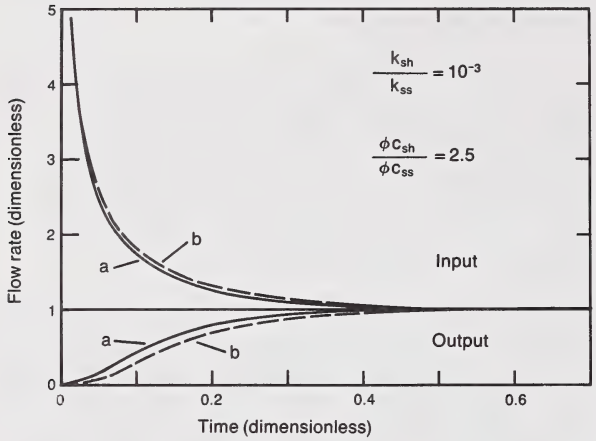

Figure 70. *Comparison of the input and output flows through the core region with f = 0.351 shale clasts, when: (a) the medium heterogeneity (shale clasts and sand) is taken into account and (b) the medium is considered homogeneous with steady-state permeability k_{eff} and space-average porosity and compressibility $(\phi c)_A$.*

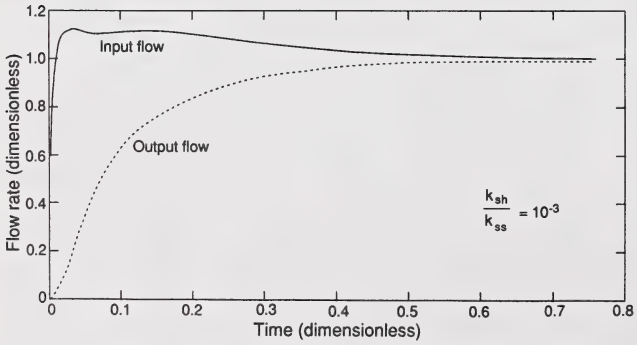

Figure 71. *Relative error in computed flow rates during transient flow, when using steady-state effective permeability and space-average compressibility instead of actual values according to heterogeneity distribution: (a) input flow and (b) output flow.*

QUANTITATIVE CHARACTERIZATION OF THE RESERVOIR

Effective values for permeability and porosity have been derived in the previous sections of this report for the five flow units identified in the Provost Upper Mannville B Pool. The values for the sandy portion of the reservoir were scaled up from the core to the flow unit scale using standard statistical averaging methods. For the heterogeneous shale clast layers in the reservoir, numerical modeling techniques were used to scale up permeability from the core to the layer and zone scale. The combination of these two different approaches has provided a quantitative characterization of the reservoir. Effective values for permeability and porosity for each of the reservoir flow units for the composite example well of Figure 29 are given in Figure 72.

For single well numerical simulation of recovery processes, the scaling up methods described in this report and used to derive the values presented in Figure 72 are probably sufficient to assign characteristic permeability and porosity values to the reservoir simulator grid blocks. If a recovery process is to be simulated for a specific area of the reservoir, i.e., a multiwell simulation, then the entire scaling up procedure for both the sandy and heterogeneous flow units has to be applied to every well in that portion of the reservoir. Interwell variability prediction techniques (Haldorsen and Damsleth, 1990) should be used to assign values to the non-well simulator grid blocks. The subject of interwell variability of reservoir properties is a separate area of research and was not addressed in this study. For regional, or basin scale modeling, the reservoir effective values of transmissivity and porosity can be used directly.

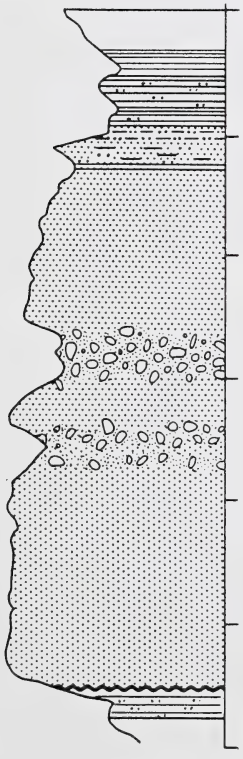

Flow Unit	Characteristic Values		
	k_v (md)	k_h (md)	ϕ
Channel Margin sands		366	0.24
Transition Zone sands	1376	1785	0.28
Shale Clast layer	1331	1922	0.24
Oil saturated Blocky Channel sands	3328	3843	0.33
Shale Clast layer	2108	2828	0.27
Oil saturated Blocky Channel sands	3328	3843	0.33
Water saturated Blocky Channel sands	1905	2200	0.30

Figure 72. *Effective values for permeability and porosity for all reservoir flow units in the composite example well.*

SUMMARY AND CONCLUSIONS

A comprehensive approach to reservoir characterization was developed using an integrated, interdisciplinary study involving geology, pore system analysis, and parameter modelling. The Provost Upper Mannville B Pool was used as a case study. The approach is a sequential one, starting with a detailed understanding of the reservoir geology and pore systems, and scaling up conventional core analysis permeability and porosity data to the flow unit or reservoir grid block scale. Different methodologies were adopted for each flow unit, depending on its internal characteristics.

For the "relatively uniform" sandy flow units, conventional statistical scaling up techniques were adopted. For those units where there is no trend in reservoir properties, the geometric average was used to scale up horizontal permeability values to the flow unit scale. For interbedded sands and shales, the arithmetic average of core plug values was used to characterize horizontal permeability. For those flow units that have a depth trend in the variation of permeability values, the average of the trend was used to define the characteristic horizontal permeability value. Vertical permeability values were assessed by examining the k_v/k_h anisotropy relation for each flow unit. Porosity was scaled up using a weighted average of individual interval measurements for each sandy flow unit.

For the heterogeneous shale clast flow unit, the scaling up of permeability values was carried out by means of numerical flow simulations. General curves were developed that relate shale clast content and aspect ratio of the clasts to effective permeability, expressed relative to the permeability of the sand matrix. These curves can be used to derive characteristic values for shale clast layers or zones based on an estimate of the shale clast content and aspect ratio, as seen in core. Because this relation does not appear to be dependent on clast size or shape when the permeability contrast between the sand matrix and the shale body is greater than 100, these results can be extended to other sand/shale systems, such as shale lenses or beds in a sandstone reservoir.

The combination of these approaches has provided a comprehensive methodology for a quantitative characterization of siliciclastic reservoir flow units at every well in the reservoir. The resulting parameter values can be used as input for numerical simulation of recovery processes. For multiwell simulations, interwell variability prediction techniques should also be used to assign values to the non-well simulator grid blocks.

For the Provost Upper Mannville B Pool reservoir, the following specific conclusions were reached:

1. The Upper Mannville McLaren Formation, which forms the reservoir, can be divided into six lithofacies: a blocky channel sands lithofacies; a transition zone sand lithofacies; a shale clast lithofacies; a channel margin sand lithofacies; an overbank lithofacies; and an abandonment lithofacies. Reservoir sediments were deposited in sandy fluvial systems aggrading a pre-existing valley system, as a result of a relative rise in sea level.

2. The framework grain mineralogy of the reservoir is dominated by quartz (85%), with only small amounts of K-feldspar, chert, and rock fragments. Kaolinite is the dominant clay mineral (80%), with minor amounts of illite and traces of smectite and chlorite.

3. Petrographic image analysis was used to characterize the reservoir pore systems. Four end member pore systems were identified and are used to relate pore system properties to reservoir lithofacies. Pore size and pore connectivity can be used to quantify permeability where no measurements are available. Pore characteristics can be qualitatively related to capillary pressure and residual saturation.

4. The sandy portions of the reservoir were subdivided into four flow units based on lithology, fluid composition, permeability, porosity, and pore system characteristics. In ascending order these are: the water-saturated blocky channel sands, the oil-saturated blocky channel sands, the transition zone sands, and the channel margin sands. Effective horizontal permeability and porosity values were calculated for each flow

unit on a well basis in Sections 17 and 20, Township 37, Range 1, west of the Fourth Meridian. Reservoir scale characteristic values for porosity and transmissivity were also calculated for this area of the reservoir. A relation was developed to relate vertical and horizontal permeability for the blocky channel sands.

5. For the heterogeneous shale clast zone flow unit, a combination of methodologies (2D and 3D numerical flow modelling, electrical analogue, and physical flow simulations) were used to develop effective values for horizontal and vertical permeability at the core scale. The resulting curves relating shale clast content and aspect ratio with effective permeability can be used for reliable, practical estimates, based on examination of slabbed cores. A methodology is presented to derive effective permeability using these curves and estimates of average layer clast content, for reservoir grid blocks containing a single shale clast layer or interbedded layers of shale clasts and sand. The effective values for permeability and compressibility during transient flow are time dependent and at any moment depend on the flow type and direction.

New computer code is included for: (1) a generalized size analysis algorithm for pore system analysis; (2) stereology and numerical clast generation; and (3) 3D finite difference, single phase fluid flow simulation.

ACKNOWLEDGEMENTS

The authors would like to thank the Alberta Research Council (ARC), the Alberta Oil Sands Technology and Research Authority (AOSTRA), and the Alberta Department of Energy for financially sponsoring this research program. We would also like to thank Mike Prentice, Ed Hasiuk, and Bonnie Morris for helping with parts of this study, during temporary assignments to the project team. Kathy Hamilton and Joe Olic provided the technical support to the project team. In addition, we would like to thank Andre Lytviak, Desmond Wynne, and Michel Brulotte for computing support; Chaitanya Singh and Bruno Untergasser for palynological consultation; Max Baaske, Campbell Kidston, and Dianne Goulet for laboratory support; Gerald Kissel from the Oil Sands and Hydrocarbon Recovery Department for his help with the design of the physical experiments; the staff of the ARC Graphic Services Department for drafting of figures; and Margaret Booth for typing of this report. Diane Teppan from AOSTRA did a first class job of the publication of this report. Special thanks are extended to Dr. David Redford and Dr. Chu Hsi from AOSTRA for their strong support of the oil sands geology research program at ARC.

REFERENCES

Aziz, K. and Settari, A., 1979, Petroleum Reservoir Simulation: Applied Science Publishers Ltd., London, 476 p.

Bachu, S. and Cuthiell, D.L., 1990, Effect of Core Scale Heterogeneity on Steady State and Transient Fluid Flow in Porous Media: Numerical Analysis; Water Resources Research, v. 26 (5), p. 863–874.

Begg, S.H., Carter, R.R. and Dranfield, P., 1987, Assigning Effective Values to Simulator Grid-Block Parameters in Heterogeneous Reservoirs: SPE 16754.

Begg, S.H., Chang, D.M. and Haldorsen, H.H., 1985, A Simple Statistical Method for Calculating the Effective Permeability of a Reservoir Containing Discontinuous Shales: SPE 14271.

Begg, S.H. and King, P.R., 1985, Modelling the Effects of Shales on Reservoir Performance; Calculation of Effective Vertical Permeability: SPE 13529.

Berryman, J.G. and Blair, S.C., 1987, Kozeny-Carman Relations and Image Processing Methods for Estimating Darcy's Constant: Journal of Applied Physics, v. 62 (6), p. 2221–2228.

Burchfield, T.E. and Harnapour, M.M., 1989, Special Reservoir Characterization Needs for Application of Enhanced Oil Recovery, Tutorial: Second International Reservoir Characterization Technical Conference, Dallas, Texas, June 25–28, 1989.

Cant, D.J. and Walker, R.G., 1978, Fluvial Processes and Facies Sequences in the Sandy Braided South Saskatchewan River, Canada: Sedimentology, v. 25, p. 625–648.

Collins. H. N., 1977, Properties of Unconsolidated Sands, Log-Core Study of Bodo Upper Mannville 'B' Pool: Petroleum Recovery Institute Interim Report IR–4, 49 p.

Collins, H.N. and Pilles, D., 1981, Reconciliation of Porosity Interpretations in McLaren Sands using Functional Analysis: Petroleum Recovery Institute Report 1981–11, 33 p.

Crabtree, S.J., Yuan, L. and Ehrlich, R., 1991, A Fast and Accurate Erosion-Dilation Method Suitable for Microcomputers: Computer Vision, Graphics, and Image Processing, v. 53, no. 3, p. 283–290.

Cushman, J.H., 1984, On Unifying the Concepts of Scale, Instrumentation and Stochastics in the Development of Multiphase Transport Theory: Water Resources Research, v. 20, p. 1668–1676.

Cuthiell, D.L., Bachu, S., Kramers, J.W. and Yuan, L-P., 1991, Characterizing Shale Clast Heterogeneities and their Effect on Fluid Flow: Second International Reservoir Characterization Technical Conference Proceedings, Dallas, Texas, June 25–28, 1989, Academic Press, p. 226–250.

Dagan, G., 1989, Flow and Transport in Porous Formations: Springer Verlag, Heidelberg, 465 p.

Dagan, G., 1986, Statistical Theory of Groundwater Flow and Transport: Pore to Laboratory, Laboratory to Formation, and Formation to Regional Scale: Water Resources Research, v. 22 (9), p. 1205–1345.

Dagan, G., 1982, Analysis of Flow through Heterogeneous Random Aquifers, 2; Unsteady Flow in Confined Formations: Water Resources Research, v. 18 (5), p. 1571–1585.

Delfiner, P., 1972, A Generalization of the Concept of Size: Journal of Microscopy, v. 95, p. 203–216.

Desbarats, A.J., 1987a, Stochastic Modeling of Flow in Sand-Shale Sequences: PhD Thesis, Stanford University.

Desbarats, A.J., 1987b, Numerical Estimation of Effective Permeability in Sand-Shale Formations: Water Resources Research, v. 23, p. 273–286.

Deutsch, C., 1989, Calculating Effective Absolute Permeability in Sandstone/Shale Sequences: SPE 17264.

Dilks, A, and Graham, S.C., 1985, Quantitative Mineralogical Characterization of Sandstone by Back-Scattered Electron Image Analysis, Journal of Sedimentary Petrology: v. 55 (3), p. 347–355.

Doyen, P.M., 1988. Permeability, Conductivity, and Pore Geometry of Sandstone: Journal of Geophysical Research, v. 93 (B7), p. 7729–7740.

Dupuy, M. and Lefebre du Prey, E., 1968, L'Anisotropie d'Ecoulment en Milieu Poreux Presentant des Intercalations Horizontales Discontinues: presented at 3rd Colloqium, Assoc. de Res. sur les Tech de Forage et de Prod. Pau, France, p. 23–26.

Ehrlich, R. and Davies, D.K., 1989, Image Analysis of Pore Geometry: Relationship to Reservoir Engineering and Modeling, SPE 19054.

Ehrlich, R., Kennedy, S.K., Crabtree, S.J. and Cannon, R.L., 1984, Petrographic Image Analysis, 1, Analysis of Reservoir Pore Complexes: Journal of Sedimentary Petrology, v. 54, p. 1365–1378.

Fabbri, A.G., 1984, Image Processing of Geological Data: Van Nostrand Reinhold Company Inc., New York, 244 p.

Feret, L.R., 1931, La Grosseur des Grains des Matieres Pulverulentes: Association Internationale pour l'Essai des Materiaus, v. 2D, p. 428.

Freeze, R.A., 1975, A Stochastic-Conceptual Analysis of One-Dimensional Groundwater Flow in Non-Uniform Homogeneous Media: Water Resources Research, v. 11 (5), p. 725–741.

Full, W.E., Ehrlich, R. and Kennedy, S.K., 1984, Optimal Configuration and Information Content of Sets of Frequency Distributions: Journal of Sedimentary Petrology, v. 54, p. 117–126.

Full, W.E., Ehrlich, R. and Klovan, J.E., 1981, EXTENDED QMODEL — Objective Definition of External End Members in the Analysis of Mixtures: Mathematical Geology, v. 13, p. 331–344.

Gelhar, L.W. and Axness, C.L., 1983, Three-Dimensional Stochastic Analysis of Microdispersion in Aquifers: Water Resources Research, v. 19 (1), p. 161–180.

Gelhar, L.W., Gutjahr, A.L. and Naff, R.L., 1979, Stochastic Analysis of Macrodispersion in a Stratified Aquifer: Water Resources Research, v. 15 (6), p. 1387–1397.

Gies, R.M., 1987, An Improved Method for Viewing Micropore Systems in Rocks With the Polarizing Microscope: SPE Formation Evaluation, v. 2, p. 209–214.

Gross, A.A., 1981a, Some Aspects of Geological Contribution to EOR — Comparison of the Geometry of Three Mannville Sand Reservoirs: CIM 81–32–15.

Gross. A.A., 1981b, A Geological Study of Three Mannville Sand Reservoirs — Chauvin South (Sparky A and B), Provost (Upper Mannville B) = Bodo, David (Lloydminster A): Petroleum Recovery Institute Report 1981–5, 96 p.

Gross. A.A., 1980, Mannville Channels in East-Central Alberta: ***in***, L.S. Beck, J.E. Christopher, and D.M. Kent (eds.), Lloydminster and Beyond, Geology of Mannville Hydrocarbon Reservoirs, Saskatchewan Geological Society Special Publication Number 5, p. 33–63.

Gupta, S.K., Cole, C.R. and Pinder, G.F., 1984, A Finite-Element Three-dimensional Groundwater (FE3DGW) Model for a Multiaquifer System: Water Resources Research, v. 20, p. 553–563.

Gutjahr, A.L., Gelhar, L.W., Bakr, A.A. and McMillan, J.R., 1978, Stochastic Analysis of Spatial Variability in Subsurface Flows, 2. Evaluation and Application: Water Resources Research, v. 14, p. 953–959.

Haq, B.U., Hardenbol, J. and Vail, P.R., 1987, Chronology of Fluctuating Sea Levels since the Triassic: Science, v. 235, p. 1156–1167.

Hayashitani, M. and Davis, W., 1981, Provost Upper Mannville B Pool: Petroleum Recovery Institute Report 1981–7, 110 p.

Haldorsen, H.H., 1989, On the Modeling of Vertical Permeability Barriers in Single Well Simulation Models: SPE Formation Evaluation, v. 4, p. 349–358.

Haldorsen, H.H. and Damsleth, E., 1990, Stochastic Modeling: Journal of Petroleum Technology, v. 42 (4), p. 404–412.

Haldorsen, H.H. and Lake, L.W., 1984, A New Approach to Shale Management in Field Scale Simulation Models: Society Petroleum Engineers Journal, v. 24, p. 447–457.

Jackson, P.C., 1984, Paleogeography of the Lower Cretaceous Mannville Group of Western Canada: ***in***, J.A. Masters (ed.), Elmworth — Case Study of a Deep Basin Gas Field, American Association of Petroleum Geologists Memoir 38, p. 49–77.

Journel, A.G., Deutsch, C. and Desbarats, A.J., 1986, Power Averaging for Block Effective Permeability: SPE 15128.

Journel, A.G. and Huijbregts, C., 1978, Mining Geostatistics: Academic Press, Orlando, Florida, 600 p.

Kirkpatrick, S., 1973, Percolation and Conduction, Reviews of Modern Physics, v. 45, p. 574–588.

Korvin, G., 1982, Axiomatic Characterization of the General Mixture Rule: Geoexploration, v. 19, p. 267–276.

Kramers, J.W., Bachu, S., Cuthiell, D.L., Prentice, M.E. and Yuan, L.P., 1989, A Multidisciplinary Approach to Reservoir Characterization; the Provost Upper Mannville B Pool: Journal of Canadian Petroleum Technology, v. 28, no. 3, p. 48–58.

Lasseter, T.J., Waggoner, J.R. and Lake, L.W., 1986, Reservoir Heterogeneities and Their Influence on Ultimate Recovery: ***in***, L.W. Lake and H.B. Carroll Jr. (eds.), Reservoir Characterization, Academic Press, p. 545–559.

Li, Y. and Wardlaw, N.C., 1986a, The Influence of Wettability and Critical Pore-Throat Size Ratio on Snap-off, Journal of Colloid and Interface Science, v. 109, p. 461–472.

Li, Y. and Wardlaw, N.C., 1986b, Mechanisms of Nonwetting Phase Trapping during Imbibition at Slow Rate, Journal of Colloid and Interface Science, v. 109, p. 473–486.

MacCallum, G.T. and McCrossan, R.G., 1979, The Lloydminster Oil Play in Alberta (abs.): Canadian Society of Petroleum Geologists Reservoir, v. 6, p. 1–2.

Macmullin, R.B., and Muccini, G.A., 1956, Characteristics of Porous Beds and Structures, AIChE Journal, v. 2, p. 393–403.

Matheron, G.F., 1975, Random Sets and Integral Geometry, Wiley, New Nork.

Matheron. G., 1967, Elements pour une Theorie des Milieux Poreux: Paris, Masson, 168 p.

Nazarko, T.W., 1983, Review of Bodo Fireflood Pilot Project: Advanced Petroleum Recovery Conference, AOSTRA/Can. Pet., Calgary, 15 p.

Orr, R.D., Johnston, J.R. and Manko, E.M., 1977, Lower Cretaceous Geology and Heavy Oil Potential of the Lloydminster Area: Bulletin of Canadian Petroleum Geology, v. 25, p. 1187–1221.

Outtrim, C.P. and Evans, R.G., 1978, Alberta's Oil Sands Reserves and their Evaluation: ***in***, D.A. Redford and A.G. Winestock (eds.), The Oil Sands of Canada–Venezuela, CIM Special Volume 17, p. 36–66.

Parker, J.R., 1988, A Faster Method for Erosion and Dilation of Reservoir Pore-Complex Images: Canadian Journal of Earth Sciences, v. 25 (7), p. 1128–1131.

Peaceman, D.W., 1977, Fundamentals of Numerical Reservoir Simulation: Elsevier, 176 p.

Prentice, M.E. and Kramers, J.W., 1987, Petrology and Diagenesis of the McLaren Formation in the Bodo Area of East Central Alberta, ARC/AOSTRA/AE Joint Oil Sands Geology Research Program, Project Technical Report, 141 p.

Quintard, M. and Whitaker, S., 1987, Ecoulement Monophasique en Milieu Poreux; Effet des Heterogeneites Locales: Journal de Mecanique Theorique et Applique, v. 6 (5), p. 691–726.

Reservoir Analysis Project, 1990, Reservoir Analysis of the Provost Upper Mannville B Pool (1989/90 Progress Report): Project Technical Report to AOSTRA and Alberta Department of Energy, 92 p.

Reservoir Analysis Project, 1989, Reservoir Analysis of the Provost Upper Mannville B Pool (1988/89 Progress Report): Project Technical Report to AOSTRA and Alberta Department of Energy, 57 p.

Richardson, S. and Vigrass, L.W., 1984, Geology of Neilburg McLaren Pool West-Central Saskatchewan: ***in***, J.A. Lorsong and M.A. Wilson (eds.), Oil and Gas in Saskatchewan — 1984, Saskatchewan Geological Society Special Publication Number 7, p. 201–209.

Rink, M., 1976, A Computerized Quantitative Image Analysis Procedure for Investigating Features and an Adapted Image Process: Journal of Microscopy, v. 107, p. 267–286.

Rink, M. and Schopper, J.R., 1978, On the Application of Image Analysis to Formation Evaluation: The Log Analyst, v. 19, p. 12–22.

Rosenfeld, A. and J.L. Pfaltz, 1968, Distance Functions on Digital Pictures: Pattern Recognition, v. 1, p. 33–61.

Rosenfeld, A. and A.C. Kak, 1982, Digital Picture Processing, Vol. II, p. 211–219, Academic Press, Orlando.

Ruzyla, K., 1986, Characterization of Pore Space by Quantitative Image Analysis, SPE Formation Evaluation, v. 1, p. 389–398.

Ruzyla, K. and Jezek, D.I., 1987, Staining Method for Recognition of Pore Space in Thin and Polished Sections, Journal of Sedimentary Petrology: v. 57, no. 4, p. 777–778.

Salahub, D.W. and Mudie, D.W., 1989, Bodo: Steaming into the Nineties: Oil Sands 2000, Energy–Environment–Enterprise, AOSTRA Annual Meeting, Edmonton, Alberta, March 26–28, 1990.

Scheidegger, A.E., 1960, The Physics of Flow through Porous Media, Rev. edition, University of Toronto Press, 313 pp.

Serra, J., 1982, Image Analysis and Mathematical Morphology: New York, Academic Press, 610 p.

Tough, J.G. and Miles, R.G., 1984, A Method for Characterizing Polygons in Terms of the Principal Axes: Computers and Geosciences, v. 10, p. 347–350.

van Wagoner, J.C., Mitchum, R.M., Campion, K.M. and Rahmanian, V.D., 1990, Siliclastic Sequence Stratigraphy in Well Logs, Cores, and Outcrops: American Association of Petroleum Geologists Methods in Exploration Series No. 7, 55 p.

Vigrass, L.W., 1977, Trapping of Oil at Intra-Mannville (Lower Cretaceous) Disconformity in Lloydminster Area, Alberta and Saskatchewan: American Association of Petroleum Geologists Bulletin, v. 61, p. 1010–1028.

Vigrass, L.W., Richardson, S. and Pappas, E.S., 1987, Reservoir Geology of the Neilburg McLaren Pool, Lloydminster Region of Saskatchewan: Journal of Canadian Petroleum Technology, v. 26, p. 43–52.

Wadell, H., 1932, Volume, Shape and Roundness of Rock Particles: Journal of Geology, v. 40, p. 443.

Walsh, J.B. and Brace, W.F., 1984, The Effect of Pressure on Porosity and the Transport Properties of Rock: Journal of Geophysical Research, v. 89, p. 9425–9431.

Warren, J.E. and Price, H.S., 1961, Flow in Heterogeneous Porous Media: Society of Petroleum Engineers Journal, v. 1, p. 153–169.

Weber, K.J. and van Geuns, L.C., 1989, Framework for Constructing Clastic Reservoir Simulation Models: SPE 19582.

Weibel, R.R., 1980, Stereological Methods, Vol. 2: Academic Press, London, 340 p.

Wightman, D.M., Pemberton, S.G. and Singh, C., 1987, Depositional Modelling of the Upper Mannville (Lower Cretaceous), East Central Alberta; Implications for the Recognition of Brackish Water Deposits: ***in***, R.W. Tillman and K.J. Weber (eds.), Reservoir Sedimentology, Society of Economic Paleontologists and Mineralogists Special Publication 40, p. 189–220.

Wilgus, C.K., Posamentier, H., Ross, C.A. and Kendall, C.G.St.C. (eds.), 1988, Sea Level Changes — an Integrated Approach: Society of Economic Paleontologists and Mineralogists Special Publication 42, 407 p.

Wilson, M.A. and Bennett, R.W., 1985, Evaluation of Saskatchewan's Heavy Oil Reserves: Saskatchewan Energy and Mines, Saskatchewan Geological Survey Open File Report, 25 p.

Young, D.M., 1971, Iterative Solutions of Large Linear Systems, Academic Press, New York.

APPENDIX A

Generalized Size Analysis Algorithms For Pore System Analysis

The generalized size analysis procedure (Delfiner, 1972), a special form of "granulometry" (Matheron, 1967, 1975), is a powerful concept for analyzing the size of highly irregular binary images, such as pore images. For circular shaped objects, this analysis also conforms with conventional size measurement. Various algorithms can be implemented for this type of analysis with significantly different accuracy and efficiency. Delfiner (1972) used a series of "opening" image processing operations to perform this analysis. Several "erosion-dilation" based algorithms have subsequently been developed to be more efficient (Rink, 1976; Ehrlich, et al., 1984; Parker, 1988; Crabtree, et al., 1991). In this Appendix, existing algorithms will be briefly reviewed, discrete distance functions for more accurate measurement will be discussed, and an efficient "direct approach" algorithm will be presented.

Opening. Size analysis by performing conventional opening processes on a digital computer is very slow, especially for large pore features which require many opening steps and large structuring elements at later steps. The CPU time for one opening is proportional to the number of pixels of the structuring element. For example, a disk with radius one is usually represented by a 3×3 matrix; i.e., nine pixels. A disk with a radius of five is represented by a 11×11 matrix which has 121 pixels. Therefore, the CPU cost for an 11×11 structuring element opening is more than 13 times that for the opening with a 3×3 structuring element. It is proportional to the square of the disk radius. Moreover, the number of opening processes for a complete size analysis is in proportion to the largest feature on the image. As a result, the total CPU time is proportional to the cube of the size of the largest feature on an image. For a typical pore image, this algorithm is too slow to be practical.

Unit erosion and dilation. A significant improvement in computing time can be made by replacing the conventional opening operation by a series of one unit erosions (with a 3×3 structuring element) followed by the same number of one unit dilations. The opening with a disk of radius n (n is a positive integer) is an erosion with the structuring element, followed by a dilation with the same structuring element (Figure 19 in main text). The erosion with a disk of radius n, which removes a layer of porosity with a width of n along the boundary, can be approximated by n erosions with a disk of unit radius, which remove n layers of porosity along the boundary with a unit width in each layer. Similarly, the dilation with a structuring element of radius n can be approximated by n one unit dilations.

Since the CPU time for one erosion with a unit disk is constant, the total CPU time for n one unit erosions is proportional to n, while the CPU time of one erosion with a disk of radius n is proportional to the square of n. Thus, for a large n, substantial CPU time can be saved. Even for a small n, such as 5, the saving is significant as shown in the following argument. The structuring element with a radius of five has 121 pixels, i.e., 121 pixel operations are needed at each point to erode a five pixel wide layer. The structuring element of a unit disk has 9 pixels and repeating the unit erosion five times results in $9 \times 5 = 45$ pixel operations to erode five one-pixel layers. Therefore about two thirds of the CPU time is saved by five erosions with a thin layer in each erosion. The same improvement can also be made on the dilation part of the opening process. As a result, the CPU time for one opening is reduced to being proportional to n. For an image with the largest feature size n_{max}, a complete size analysis requires n_{max} openings and therefore the total CPU time is proportional to the square of n_{max}.

In actual practice, it is not necessary to start eroding from the original image in each opening step. Each eroded image can be saved in the computer memory. At the beginning of the next opening, the previously eroded image can be retrieved and eroded with a unit disk to complete the erosion half of the opening process (Parker, 1988). As a result, the total number of one unit erosions is equal to the number of openings and the CPU time for the total erosions is

further reduced to being proportional to n_{max}. However, the one pixel dilation has to be repeated n times for the n^{th} opening process and no similar saving can be made. This improvement means that erosion processes are negligible compared to the dilation processes in terms of the CPU time requirement. This further reduces the total CPU time by almost half. A simplified flow chart with example images is shown in Figure A1.

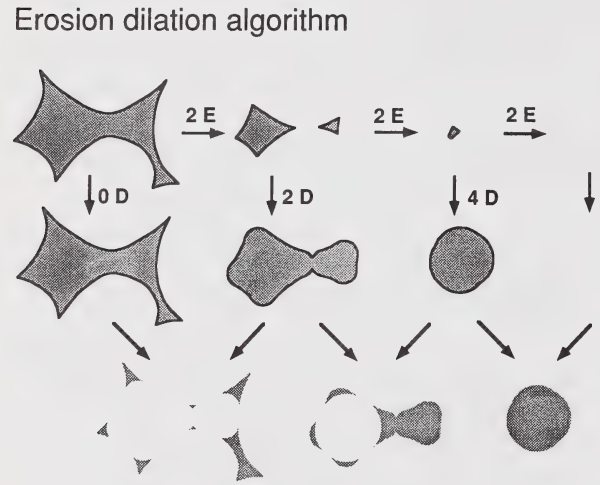

Figure A1. *Erosion-dilation image processing algorithm. Pore areas are shown in black. The difference between two sequentially dilated images indicates a successive loss of pore pixels and results in a size distribution.*

Discrete distance functions. The previous section has shown that an erosion (or dilation) with a large structuring element can be replaced by repeated erosions (or dilations) with a unit disk structuring element in order to improve the efficiency. However, one compromise has to be made for this efficiency. The problem is how to measure distance in order to approximate a circular structuring element on a grid pattern.

On a discrete grid pattern, the distances between pixels are also discrete and are usually defined by a discrete distance function. Two basic discrete functions are the four-neighbor and eight-neighbor functions, which result in two different "circular" disks (Figure A2). The four-neighbor distance function forms a disk with a diamond shape and the eight-neighbor function forms a square shaped disk. These disks can be viewed as results of repeated one unit dilations from a single pixel. By repeating unit erosions and dilations with either one of the small structuring elements, the equivalent large structuring element in the opening process is also a diamond or a square shape. This is not satisfactory because the error in a diagonal direction is 30% – 40% compared to an ideal circular shape.

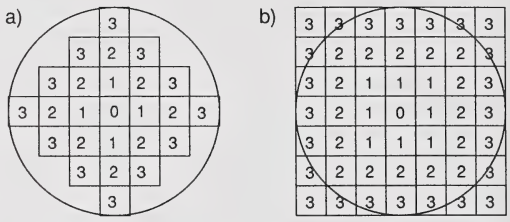

Figure A2. *Disks of radius three for (a) four-neighbor and (b) eight-neighbor distance functions.*

Rink (1976) has demonstrated that by using a mixture of the two basic structuring elements in the successive unit erosions and dilations, a better shaped large structuring element can be achieved for the opening process. He also showed that the sequence of applying these two basic structuring elements does not affect the final shape as a large structuring element for the opening process. However, in a series of opening operations for a complete size analysis, the sequence must be consistent in order to save most of the erosion CPU time as discussed in the previous section. The mixing of four-neighbor and eight-neighbor rules actually performs a family of "octagonal" discrete distance functions (Rosenfeld and Pfaltz, 1968). In this study, one four-neighbor rule is alternated with one eight-neighbor rule for the successive one unit erosions (and dilations). This results in an equivalent octagonal structuring element (Figure A3a). The shape of the octagon is much closer to a circle than the shape of a diamond or square. This four-eight alternating distance function was used for Figure 22 (main text) in which several octagonal edges can be observed.

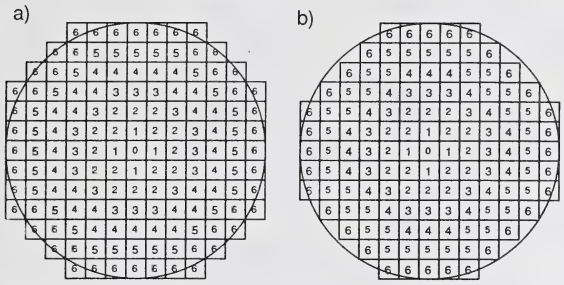

Figure A3. *Disks of radius six for (a) one (four-neighbor) to one (eight-neighbor) mixing distance function and (b) two (four-neighbor) to one (eight-neighbor) mixing distance functions.*

Hexagonal grid patterns have been extensively used in the field of mathematical morphology (Serra, 1982). The discrete distance function of a hexagonal grid produces a six sided regular polygon which can also approximate a circle better than a diamond or a square. However, most digital images are on rectangular grids and the conversion to a hexagonal grid results in loss of spatial resolution.

The mixing ratio of four-neighbor and eight-neighbor rules is not necessarily one to one. Fabbri (1984) has compared four different structuring elements, which are equivalent to four distance functions. He found that a mixing of two four-neighbor rules with one eight-neighbor rule (Figure A3b) provides a better approximation to a circle than does a simple eight-neighbor rule, hexagonal distance function, or one to one mixing of four-neighbor and eight-neighbor rules. In fact, the best mixing ratio is the square root of two to one, which theoretically results a regular eight sided polygon (Rosenfeld and Pfaltz, 1968).

Direct approach algorithm. The direct approach algorithm presented here avoids the iterations in the opening or erosion-dilation based algorithms and obtains the final size distribution in three direct steps. First, a distance map is generated in which each pixel in the pore area has a value equal to the distance between the pixel and the closest non-pore pixel. The distance map can be constructed in two passes, one forward and one backward, over the image as a standard image processing procedure for a serial computer (Rosenfeld and Kak, 1982). This procedure was also used by Parker (1988) as a globally eroded image. In this study, the octagonal distance function is used to achieve a better result. Figure A4b shows the distance map of a binary pore image (Figure A4a) as a gray level image.

Next, a skeleton map (Figure A4c) is produced by selecting these pixels with a local maximum value on the distance map. A local maximum is the value of a pixel being greater or equal to the values of its neighbor pixels. These skeleton pixels and their values still contain all the information of the original image (Rosenfeld and Kak, 1982) and the original image can be reconstructed from the skeleton points. As mentioned in the main text, the mathematical meaning of this generalized size analysis is that the size measure of each point (pixel) is equal to the radius of the largest inscribed circle that contains the point. There are many such "largest inscribed circles" for various points on a given pore image. In fact, all the skeleton pixels are the centers of these circles and the values of skeleton pixels are the radii of corresponding circles.

In the final step, a circular area is scanned around each skeleton pixel with a radius n, which is the value of the pixel on the distance map. All pixels in this circle are assigned the same value n. However, it is possible that two or more circles overlap each other in some areas where the pixels are assigned with more than one value. In such cases, the largest value among assigned values is chosen. The result is a gray level image (Figure A4d) and its intensity histogram (Figure A4e) represents the generalized size distribution of the pore areas. The average pore size can be calculated as the mean of this size distribution.

Discussion. A significant feature of this size distribution is that the even size categories usually have higher pixel counts than the odd size categories (Figure A4e). This is the result of using a one to one mixing distance function. The even size categories are associated with the eight-neighbor rule which operates not only in orthogonal directions but also in diagonal directions; therefore, it affects more pixels than does the four-neighbor rule.

Figures A5a, A5b, and A5c show three pore images with different pore sizes. Note that the difference in pore connectedness does not affect the size

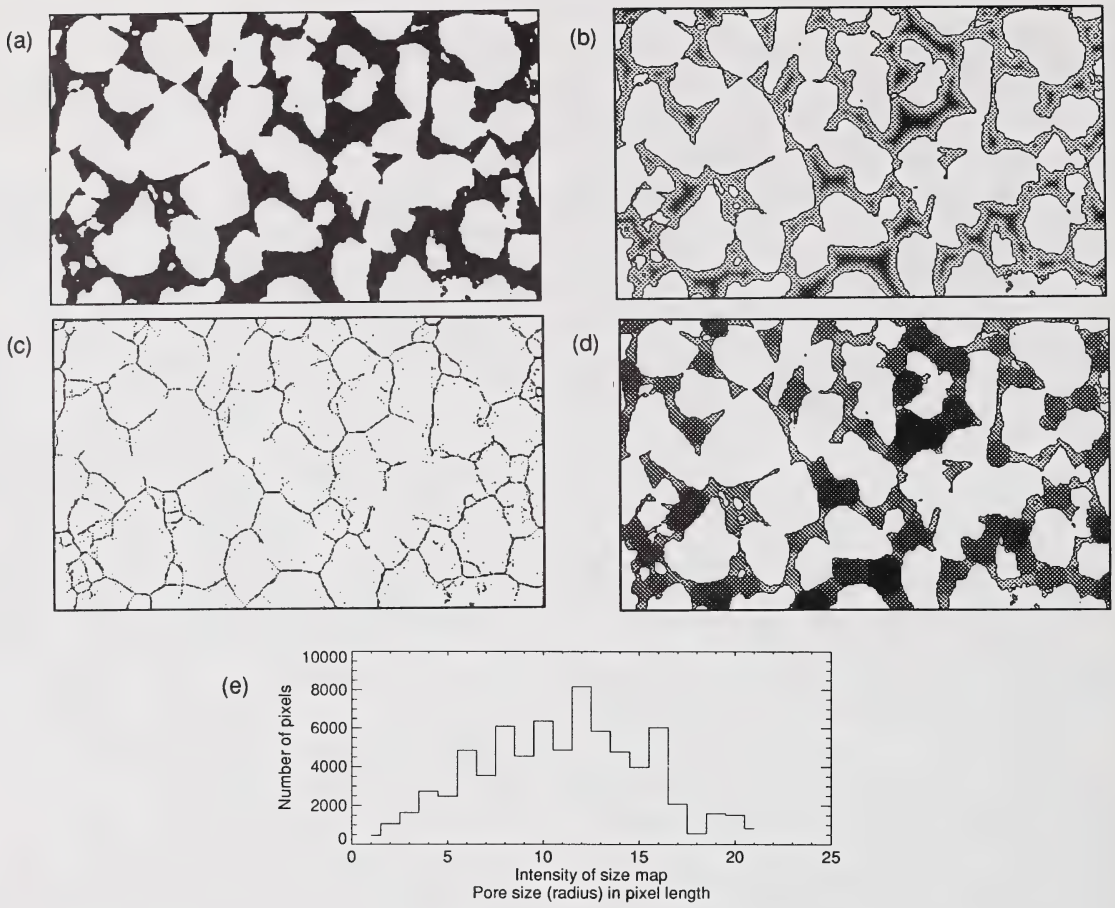

Figure A4. *Example of a binary pore image (a), its gray level distance map image (b), binary skeleton map image (c), gray level size map image (d), and the intensity histogram (e) of the size map, i.e., the pore size distribution. The average pore size is 10.9 and the average grain size is 22.2 in pixel units. All images are 580 by 378 pixels. Darker areas in gray level images indicate greater pixel values.*

measurement. Figure A5d is an image of fractured coal where pore areas are elongate fractures and the generalized size analysis provides a measure of the width of these fractures. This can also be observed in Figure A4d where elongated pore and pore throat areas have size values equal to their widths. In general, the generalized size analysis provides the linear dimension of an equi-dimensional object or the smaller dimension of an unequi-dimensional object.

The complement of pore space, the solid grains, can also be analyzed by the same technique. The result is a generalized grain or particle size distribution and may also be viewed as a possible measure of spacing of pores or fractures (Figure A5). With the help of the new algorithm, this generalized size analysis can easily be applied not only to pore images but also as a general image analysis technique to other binary images in fields such as composite material's and biomedical studies.

Program outline. The Fortran code for the generalized size analysis and smooth rough area decomposition is listed at the end of this Appendix. It

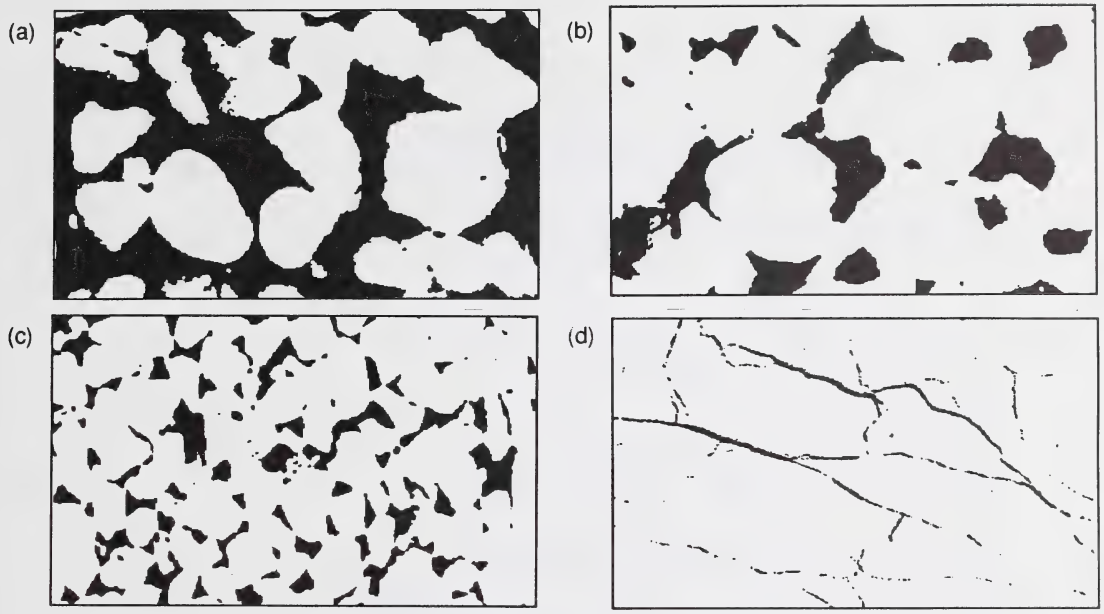

Figure A5. *Examples of pore images with different pore sizes and grain sizes. Average pore sizes are (a) 22.5 (b) 15.5 (c) 6.7 (d) 2.1 and average grain sizes are (a) 32.1 (b) 49.1 (c) 24.0 (d) 44.5 in pixel units.*

includes a main program and subroutines DISTMAP, SKEL, LABELING, EXPAND, and HISTO. The main program reads in a binary image and stores it at the centre of an array which is two columns and two rows larger than the image. These additional rows and columns are used to set boundary conditions for various operations. The main program subsequently calls subroutines DISTMAP to compute the distance map of the pore area, SKEL to find local maxima and to store these skeleton points on a different array, and LABELING to label each pixel with its porel number on a third array. For each porel, the largest distance map value (i.e., one of the skeleton pixels) is found and kept in an one-dimensional array MAXSIZE. The LABELING subroutine and the building of MAXSIZE array are needed to distinguish smooth versus rough areas at a later stage; however, they are not necessary if only the generalized size analysis is required. For each skeleton pixel, subroutine EXPAND scans a circular area with a radius equal to the distance map value of the pixel and this value is also assigned to all pixels within the circle to form a size map.

The subroutine HISTO outputs four histograms. The first is the histogram of the distance map. The second and the third are smooth and rough histograms and they are derived from the size map. If the size map values of pixels in a porel are equal to the largest size value of the porel, which is stored in the array MAXSIZE, these pixels belong to the smooth histogram. Otherwise, the pixels are added to the rough histogram. The smooth histogram plus the rough histogram is the histogram of the size map and is also the generalized size distribution. The connectivity indicator, the fraction of rough component to the total pore area, and the mean of the size distribution are computed and written to the output file.

PROGRAM LISTING

```
C       GENERALIZED SIZE AND CONNECTIVITY ANALYSIS PROGRAM
C
C       Written by Li-Ping Yuan, Alberta Geological Survey
C                                Alberta Research Council, 1990
C
        integer*2 image1(700,600),image2(700,600),image3(700,600),
     *        maxsize(2000),icol,irow
        character*1 temp(700,600)
        character*8 name
        data maxsize/2000*0/
        common irow,icol,temp
C
C       IMAGE1: EROSION (DISTANCE) MAP
C       IMAGE2: SIZE MAP
C       IMAGE3: COMPONENT LABEL MAP
C       MAXSIZE: MAXIMUM SIZE OF EACH PORE ELEMENT
C
C       READ INFORMATION
C
        read (10,'(2i4,1x,a8)')irow,icol,name
        irow=irow+1
        icol=icol+1
        do 200 j=2,irow
200     read (10,'(700a1)') (temp(i,j),i=2,icol)
C
C       INITIALIZE IMAGE1 AND IMAGE3
C
        do 300 j=2,irow
           do 300 i=2,icol
              if (temp(i,j).eq.'X') then
              image1(i,j)=1
              image3(i,j)=1
           else
              image1(i,j)=0
              image3(i,j)=0
           end if
300     continue
C
        call distmap(image1)
C
```

```
      call skel (image1,image2)
C
      call labeling(image3,nlabel)
C
C     COPY SKELETON MAP ONTO TEMP AND
C     FIND THE LARGEST SIZE OF EACH POREL
C
      do 400 j=2,irow
         do 400 i=2,icol
            if (image2(i,j).eq.0) then
            temp(i,j)=' '
         else
               temp(i,j)='X'
               l=image3(i,j)
               maxsize(l)=max(image2(i,j),maxsize(l))
            end if
400   continue
C
      call expand (image1,image2)
C
      call histo (name,image1,image2,image3,maxsize)
C
      stop
      end
C-----------------------------------------------------------------------------------------
      subroutine distmap (image)
C
C     CALCULATE DISTANCE MAP BY OCTAGONAL (1,1) DISTANCE FUNCTION
C
      integer*2 image(700,600),irow,icol,k
      character*1 temp(700,600)
      common irow,icol,temp
C
C     INITIALIZE BOUNDARY
C
      i p= icol + 1
      jp=irow+1
      do 100 i=1,ip
100   image(i,1)= 999
      do 200 j=2,irow
         image(1,j)= 999
200   image(ip,j)= 999
      do 300 i=1,ip
300   image(i,jp)= 999
C
C     FIRST (FORWARD) SCAN
```

```
C
      do 600 j=2,irow
         jm=j-1
         do 400 i=2.icol
            if (image(i,j).ne.0) then
            im=i-1
            k=(imin0(image(im,jm),image(i+1,jm))+2)/2*2
            image(i,j)=imin0(image(im,j)+1,image(i,jm)+1,k)
            end if
400   continue
         do 500 ii=2,icol
            i=icol-ii+2
500   if (image(i,j).ne.0)
     *      image(i,j)=imin0(image(i,j),image(i+1,j)+1)
600   continue
C     SECOND (BACKWARD) SCAN
C
      do 900 jj=2,irow
         j=irow-jj+2
         jp= j+l
         do 700 ii=2,icol
         i=icol-ii+2
            if (image(i,j).ne.0) then
            i p= i + 1
            k=(imin0(image(ip,jp),image(i-1,jp))+2) /2*2
            image(i,j)=imin0(image(i,j),image(ip,j)+1,
     *         image(i.jp)+1,k)
            end if
700   continue
         do 800 i=2,icol
800   if (image(i,j).ne.0)
     *      image(i,j)=imin0(image(i,j),image(i-1,j)+1)
900   continue
      return
      end
C-------------------------------------------------------------------------------
      subroutine skel (image1,image2)
C     SELECT LOCAL MAXIMUM (SKELETON) POINTS
C
      integer*2 image1(700,600),image2(700,600),irow,icol,k
      character*1 temp(700,600)
      common irow,icol,temp
C
C     INITIALIZE BOUNDARY
C
      ip=icol+1
      jp=irow+1
```

```
      do 100 i=1,ip
100   image1(i,1)= 0
      do 200 j=2,irow
         image1(1,j)= 0
200   image1(ip,j)= 0
      do 300 i=1,ip
300   image1(i,jp)= 0
C
C     FIND LOCAL MAXIMUM VALUES ON IMAGE1 AND ASSIGN THEM TO IMAGE2
C     ASSIGN 0 TO OTHER PIXELS ON IMAGE2
C
      do 400 j=2,irow
         do 400 i=2,icol
            if (image1(i,j).eq.0) then
               image2(i,j)=0
               else
                  m=imax0(image1(i+1,j),image1(i-1,j),image1(i,j+1),
     *                image1(i,j-1))
                  if (image1(i,j).lt.m) then
                  image2(i,j)=0
               else
                  k=image1(i,j)
                  if(k/2*2.ne.k) then
                     image2(i,j)=k
                  else
                     ip=i+1
                     im=i-1
                     jp=j+1
                     jm=j-1
                     m=imax0(image1(ip,jp),image1(ip,jm),
     *                   image1(im,jp),image1(im,jm))
                     if (k.lt.m) then
                        image2(i,j)=0
                     else
                        image2(i,j)=k
                     end if
                  end if
               end if
         end if
400   continue
      return
      end
C-------------------------------------------------------------------------------
      subroutine expand (image1,image2)
C
C     COMPUTE EXPENSION MAP
```

```
C
      integer*2 image1(700,600),image2(700,600),irow,icol,k
      character*1 temp(700,600)
      common irow,icol,temp
C
C     FIND SKELETON PIXELS ON TEMP AND
C     DRAW CIRCLES (OCTAGONS) AROUND THEM WITH RADIUS EQUAL TO THEIR
C           VALUES ON DISTANCE MAP AND
C     ASSIGN THE SAME VALUES TO ALL PIXELS WITHIN
C           THE CORESPONDING CIRCLES AND
C     IF CIRCLES OVERLAP EACH OTHER,
C           EACH PIXEL GETS THE LARGEST VALUE AMONG ASSIGNED VALUES.
C
      do 500 j=2,irow
         do 500 i=2,icol
            if (temp(i,j).eq.'X'.and.image1(i,j).ne.1) then
               k=image1(i,j)
               km=k-1
               jtop=max(2,j-km)
               jbot=min(irow,j+km)
               do 400 jj=jtop,jbot
                  iii=min(km,km*3/2-abs( jj-j) )
                  ileft=max(2,i-iii)
                  iright=min(icol,i+iii)
                  do 400 ii=ileft,iright
                     image2(ii,jj)=imax0(image2(ii,jj),k)
400         continue
         end if
500   continue
      return
      end
C-------------------------------------------------------------------------------
      subroutine labeling (image,n)
C
C     FIND EACH POREL AND LABEL THEM FROM 1 TO N
C     SEE ALGORITHM ON ROSENFELD AND KAK (1976) BOOK
C
      integer*2 image(700,600),label(2000),irow,icol,count
      character*1 temp(700,600)
      common irow,icol,temp
C
C           COMPONENT LABELING
C           N: NUMBER OF COMPONENTS
C
C           SET BOUNDARY CONDITION
C
      ip1=icol+1
```

```
      jp1=irow+1
      do 10 i=1,ip1
         image(i,1)=0
10       image(i,jp1)=0
      do 20 j=2,irow
         image(1,j)=0
20       image(ip1,j)=0
      do 30 i=1,2000
30       label(i)=i
C
C     FIRST SCAN
C
      count=1
      do 100 j=2,irow
         jm1=j-1
         do 100 i=2,icol
            if(image(i,j).eq.1) then
               li=image(i-1,j)
               lj=image(i,jm1)
               if(li.ne.0) then
                  image(i,j)=li
                  if (lj.ne.0.and.li.ne.lj) then
                     kmin=min(li,lj,label(li),label(lj))
                     label(li)=kmin
                     label(lj)=kmin
                     image(i,j)=kmin
                  end if
               else if(lj.ne.0) then
                  image(i,j)=lj
               else
                  image(i,j)=count
                  count=count+1
                  if (count.gt.2000)
     *               write(6,'(21h increase label count)')
            end if
         end if
100   continue
C
C     SORT LABELS
C
      count=count-1
      do 300 i=1.count
         if (label(i).ne.i) then
            do 200 j=i+1,count
200         if (label(j).eq.i) label(j)=label(i)
         end if
```

```
300       continue
          n=1
          do 500 i=1,count
             if(label(i).ge.n) then
                if(label(i).gt.n) then
                   k=label(i)
                   label(i)=n
                   do 400 j=i+1,count
400                if(label(j).eq.k) label(j)=n
                end if
                n=n+1
             end if
500       continue
C
C         SECOND SCAN
C
          do 600 j=2,irow
             do 600 i=2,icol
                if (image(i,j).ne.0) then
                   image(i,j)=label(image(i,j))
                   if (image(i,j).ne.image(i-1,j).or.
     *                image(i,j).ne.image(i,j-1)) then
                      if(image(i,j-1)*image(i-1,j).ne.0)
     *                   write(6,'(12h label wrong,2i4)') i,j
                   end if
                end if
600       continue
          return
          end
C-------------------------------------------------------------------------------
          subroutine histo (name,image1,image2,image3,maxsize)
C
C         CALCULATE AND OUTPUT SIZE DISTRIBUTIONS
C
          integer*2 image1(700,600),image2(700,600),image3(700,600)
     *         ,maxsize(2000),irow,icol,ke,ks,kr
          integer*4 histe(200),hists(200),histr(200)
          character*1 temp(700,600)
          character*8 name
          data histe,hists,histr/600*0/
          common irow,icol,temp
C
C         HISTE: EROSION (DISTANCE MAP) DISTRIBUTION
C         HISTS: SMOOTH DISTRIBUTION
C                (PIXELS WITH THE LARGEST SIZE IN A POREL)
C         HISTR: ROUGH DISTRIBUTION
C                (PIXELS OTHER THAN SMOOTH PIXELS)
```

```
C
      do 400 j=2,irow
         do 400 i=2,icol
            ke=imin0(image1(i,j),200)
            k=imin0(image2(i,j),200)
            if (ke+k.ne.0) then
               if (ke*k.eq.0) then
                  write (6,'(6h wrong,2i5)') i,j
               else
                  histe(ke)=histe(ke)+1
                  if(k.eq.maxsize(image3(i,j))) then
                     hists(k)=hists(k)+1
                  else
                     histr(k)=histr(k)+1
                  end if
               end if
            end if
400      continue
C
C        FIND THE LARGEST SIZE IN THE IMAGE
C
         do 500 ii=1,200
            i=201-ii
            if(histe(i).ne.0) go to 600
500      continue
C
C        CALCULATE MEAN SIZE AND CONNECTIVITY INDICATOR
C
600      sume=0.0
         sums=0.0
         sumr=0.0
         do 700 j=1,i
            sume=sume+histe(j)
            sums=sums+hists(j)
            sumr=sumr+histr(j)
700      continue
         con=sumr/sume
C
C        OUTPUT
C
         open (unit=13,status='new',file='size.out',recl=132)
C
         write (13,1000) i,name,sume,(histe(j),j=1,i)
1000     format(' EROSION (DISTANCE MAP) DISTRIBUTION,  MAX.',I4,
     *        5x,a8,f10.0,/,(1x,13i6))
C
         write (13,2000) sums,(hists(j),j=1,i)
```

```
2000     format(' SMOOTH AREA DISTRIBUTION',f10.0,/,(1x,13i6))
C
         write (13,3000) sumr,(histr(j),j=1,i)
3000     format(' ROUGH AREA DISTRIBUTION',f10.0,/,(1x,13i6))
C
C        CALCULATE GENERAL SIZE DISTRIBUTION AND OUTPUT
C
         sum=0.0
         do 800 j=1,i
            histr(j)=hists(j)+histr(j)
            sum=sum+histr(j)*j
800      continue
         width=sum/sume
         write (13,4000) width,con,(histr(j),j=1,i)
4000     format(   ' AVERAGE SIZE (WIDTH):',F6.2,5X,'CONNECTIVITY:',F6.3,/,
     *            ' GENERALIZED SIZE DISTRIBUTION',/,(1x,13i6))
         return
         end
```

APPENDIX B

Stereology and Clast Generation Software

This appendix provides greater details of the stereological procedure and simulation process used to construct three-dimensional distributions of synthetic clasts. As discussed in the text, the real, complex geometry of shale clasts is approximated as that of oblate ellipsoids. In this approximation, the size and aspect ratio distributions for shale clasts observed in core are taken to be the corresponding distributions of ellipse length and aspect ratio that would be found from sectioning the synthetic distribution of ellipsoids. Thus, the sectional properties of the ellipsoid distribution are assumed to be known, and the 3D statistical properties of the ellipsoid distribution must be determined. This is a basic problem in stereology (Weibel, 1980).

A useful simplification, and one usually made in stereological calculations is to consider a discrete set of size classes of the objects being described. In the case of the oblate ellipsoids, assume that they have only a discrete set of sizes $D_1, D_2, \ldots, D_m$ and that there are unknown number densities (i.e., numbers per unit volume) $N_1, N_2, \ldots, N_m$ of these size classes in the space of interest. The ellipsoids are assumed to be randomly distributed in space and oriented subhorizontally. Now suppose that a very large number of parallel, vertical sections are made through the region containing the ellipsoids, creating a certain distribution of ellipses.

Figure B1 illustrates a particular ellipsoid having maximum dimension D_i in plan view. AA' and BB' represent two sectioning planes in this view. Sectioning planes lying between AA' and BB' (in the shaded region in Figure B1) will create ellipses with major axis lengths between d and $d+\Delta$. The probability of a sectioning plane lying in this interval is simply proportional to the thickness of the interval, δ. By a straightforward geometrical calculation:

$$(B1)\quad \delta = \frac{1}{2}\left\{\left[D_i^2 - d^2\right]^{1/2} - \left[D_i^2 - \left(d^2+\Delta\right)^2\right]^{1/2}\right\}$$

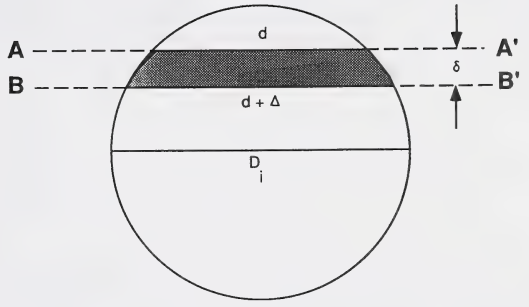

Figure B1. *Plan view of an ellipsoid with major axis length D intersected by two sectioning planes AA′ and BB′.*

Let n_i be the number of ellipses with major axis lengths between D_{i-1} and D_i (n_1 is the number with major axis lengths less than D_1). From the above argument, the contribution to n_i from ellipsoids of size D_i is proportional to:

$$(B2)\quad t_{ij} N_j$$

where:

$$t_{ij} = \left[\left(D_j - D_{i-1}\right)^{1/2} - \left(D_j - D_i\right)^{1/2}\right]$$

The total number n_i is made up of contributions from all ellipsoids with size $\geq 2\ D_i$ (smaller ellipsoids cannot produce ellipses this large when sectioned), that is:

$$(B3)\quad n_i = C \sum_{j=i}^{m} t_{ij} N_j$$

where C is a proportionality constant.

To this point, the argument has assumed an unbounded region containing the ellipsoids. However, in the case of the original clasts, the core intervals represent finite 2D sampling regions (Figure 41) and

only complete clast sections in those core samples were included in the frequency distributions shown in Figure 42. This introduces a geometrical correction factor to equation (B3) since only ellipsoids with centroids in a certain spatial region can contribute complete ellipses of a certain size in the sampling region. For example, if the sampling region is square and has size L, the correction factor for ellipses of major axis d and aspect ratio R_A can be shown to be:

$$(L-d)\frac{\left(L-R_A d\right)}{L^2}$$

This correction factor was taken into account approximately (given that clast data came for samples of different sizes, etc.) in the stereological calculation. Including the correction factor, equation (B3) may be written for all size classes i as

$$(B4)\quad n_i \sum_{j=i}^{m} M_{ij} N_j, \qquad i = 1, 2, \ldots, m$$

where

$$M_{ij} = CF_i\, t_{ij}$$

and F_i is the geometrical correction factor described above, for ellipses in class i. Therefore, the unknown number distribution of 3D ellipsoids $\{N_j\}$, must be found by solving a set of linear algebraic equations (B4). Since the coefficient matrix M is effectively of upper triangular form this set of equations is easily solved. First, N_m is given by:

$$N_m = \frac{n_m}{M_{mm}}$$

Then, N_{m-1}. N_{m-2}, . . . , N_1 are found by back-substitution into (B4). The set of N_j resulting from this calculation is very well fit by the lognormal distribution given in equation (11).

The Fortran program CLASTS.FOR (source listing below) creates distributions of oblate ellipsoids with this lognormal size distribution (see subprogram RANLEN). As a practical matter, the lognormal distribution is cut off for ellipsoid sizes greater than 40 or less than 4 pixel units, for reasons discussed in the text. In order to avoid boundary effects, the program utilizes a 20 grid unit buffer around the (128 × 128 × 128) simulation region, and ellipsoid distributions are created with their centroids randomly distributed in this larger region. No ellipsoids (with maximum size 40) outside this buffered region can contribute even partly to the interior of the simulation grid.

PROGRAM LISTING

```
** CLASTS.FOR **

*   Program to create a 3d image containing a random assembly of oblate
*   ellipsoids with a certain desired total fractional volume, and placing
*   the image in a file which can be used as input to the 3d fd
*   program FL03D.

*   The image is created in array SYSTEM that includes a 40 pixel buffer on all
*   sides. Centers of ellipsoids are uniformly distributed in a region
*   that is 20 pixels larger on all sides than the final region of interest.

*   The program calls subroutines:
*         CRELL   -  to create a single ellipsoid
*         RANLEN  -  to generate a random ellipsoid size
*         RANASP  -  to generate random aspect ratio for ellipsoid
*         INDEXX  -  to sort ellipsoid sizes before generating them (the
*                    biggest ones are generated first)

*   The program requires interactive input as well as an input file that
*   lists the volumes (nos. of grid cells) of ellipsoids with all possible
*   sizes of major and minor axes from 1 to 40 grid units. This data file
*   is easily created using the subroutine CRELL and a simple driver program.
*   The output is to the standard output (unit 6), to a file containing
*   the final "system" description, to a "log file" ,and to a file which
*   keeps track of the sizes and aspect ratios of all 2D e1lipses existing in
*   x-z planes of tht 3D "system".

*   The program uses VAX FORTRAN-77 extensions, that may need to be changed
*   if it is to be used on another system.

*   Written by D. Cuthiell, Alberta Research Council, 1990.

      real*8 dseed,d
      real*4 a(30000),b(30000),atmp(30000),btmp(30000),dvol(30000)
      integer*4 indx(30000)
      character*60 systemfile,logfile*12 /'clasts.log'/
      character*50 pixfile
      character*1 system(208,208,208) !REGION OF INTEREST IS FROM
                !PIXELS 41 TO 168 IN X, Y AND Z DIRECTIONS
      character*1 resp
      integer*4 is1/208/,is2/208/,is3/208/
      real*4 len(128,600),asp(128,600),pix(60,60)
      integer*4 num(128)
      logical*1 exist
```

```
      external ranlen,ranasp

*  parameter CRIT tells how much of an ellipsoid CANNOT overlap previously
*  generated ellipsoids

      parameter (crit = 0.95)  !less than 5% overlap

*  Initialization

      do k = 1,is3
         do j = 1.is2
            do i = 1,is1
               system(i,j,k) = ' '
            end do
         end do
      end do

*  Control choices

      write(6,610)
610   format(/' Choose a target heterogeneity fraction: ',$)
      read(5,*)tfract
      write(6,620)
620   format(/' Choose file name for output: ',$)
      read(5,500)systemfile
500   format(a)
      write(6,630)
630   format(/' Dimension in grid blocks for cubical image? ',$)
      read(5,*)nx
      ny = nx
      nz = nx
      write(6,650)
650   format(/' Do you want to specify real random number seed? ',$)
      read(5,500)resp
      if (resp.eq.'y' .or. resp.eq.'y') then
         write(6,652)
652      format(' Seed: ',$)
         read(5.*)dseed
      else !use system time
         dseed = secnds(0.)
      end if
      d = dseed
      write(6,660)
660   format(/' Name of file listing ellipse pixel sizes? ',$)
      read(5,500)pixfile
```

```
*  Maximum ellipsoid dimension = 40 grid units

         AMAX = 40.
         scale = amax/ranlen(1.) !factor by which to scale ellipsoids

*  Write all specifications to log file

         inquire (file=logfile,exist=exist)
         if (.not. exist) then
            open(8,file=logfile,status='new',carriagecontrol='list')
            write(8,800)
800         format(  '    FILE    DIMENSIONS  MAX.  LENGTH',
     &                 ' TARGET F RAN. SEED')
         else
            open(8,file=logfile,status='old',access='append')
         end if
         write(8,810)systemfile(1:18),nx,ny,nz,nint(amax),tfract,d
810      format(a18,2x,i3,'X',i3,'X',i3,5x,i3,8x,f6.4,2x,e23.16)
         close (8)

*  Get size (in grid blocks) of ellipsoids from existing file.
*  Array PIX(JJ,KK) gives the number of grid blocks in an ellipsoid with
*  major axis length JJ and minor axis length KK in grid units.

         open(21,file=pixfile,status='old',readonly)
         do i = 1,5000
            read(21,*,end=31)jj,kk,pix(jj,kk)
         end do
31       continue

*  Generate ellipsoid dimensions (length, thickness) in arrays atmp, btmp
*  until a target number of grid blocks, TVOL, are occupied.

         do i = 1,50
            dseed = dmod(16807.d0*dseed,2147483647.d0)
         end do
         tvol = tfract*float(ny)*float(nx)*float(nz)
         vol = 0.
         n = 0
         do while (vol .lt. tvol)
            n = n + 1
            r = dseed/2147483647.d0
            atmp(n) = scale*ranlen(r)
            dseed = dmod(16807.d0*dseed,2147483647.d0)
            do ii = 1,15
               dseed = dmod(16807.d0*dseed,2147483647.d0)
            end do
```

```
            r = dseed/Z147483647.d0
            btmp(n) = atmp(n)*ranasp(r)
            dseed = dmod(16807.d0*dseed,2147483647.d0)
            ind = int(atmp(n)-0.5) + 1
            ind2 = int(btmp(n)-0.5) + 1
            if (ind.gt.0 .and. ind2.gt.0) then
               dvol(n) = pix(ind,ind2)
            else
               dvol(n) = 0.
            end if
            vol = vol + dvol(n)
         end do

*  Sort the arrays atmp and btmp into new arrays a and b such that
*  ellipses are in decreasing order of volume

         call indexx(n,dvol,indx)
         do i = 1,n
            ii = n - i + 1
            a(i) = atmp(indx(ii))
            b(i) = btmp(indx(ii))
         end do

*  Generate the ellipses represented in arrays a and b at random locations

*  on the grid

         imin = 21
         irge = nx + 39
         jmin = 21
         jrge = ny + 39
         kmin = 21
         krge = nz + 39
         npixtot = 0
         do i = 1,n
*           *create test ellipse at location (ic,jc,kc) to see if it overlaps
            fnew = 0. !fraction of desired ellipse which does not overlap
                      !any existing ellipse
            do while (fnew.lt.crit) !keep trying till it fits!!
               r = dseed/2147483647.d0
               dseed = dmod(16807.d0*dseed,2147483647.d0)
               ic = imin + nint(r*float(irge))
               r = dseed/2147483647.d0
               dseed = dmod(16807.d0*dseed,2147483647.d0)
               jc = jmin + nint(r*float(jrge))
               r = dseed/2147483647.d0
               dseed = dmod(16807.d0*dseed,2147483647.d0)
```

```
                kc = kmin + nint(r*float(krge))
                call crell(system,isl,is2,is3,ic,jc,kc,a(i),b(i),
     &              0,npix,nnpix,nin,iclip,41,168,41,168,41,168,1en,asp,num)
                if (npix .gt. 0) then
                      fnew = float(nnpix)/float(npix)
                else
                      fnew = 1.
                end if
             end do
*         *  Now it fits so create it for real
             call crell(system,isl,is2,is3,ic,jc,kc,a(i),b(i),
     &            1,npix,nnpix,nin,iclip,41,168,41,168,41,168,len,asp,num)
300       format(2g13.5)
             npixtot = npixtot + nin
73           continue
          end do
          fract = float(npixtot)/float(nx)/float(ny)/float(nz)
          write(6,665)n,fract
665       format(/  ' Number of heterogeneities: ',i5,/
     1            ' Heterogeneity fraction: ',f7.4)

*   Write the system description to file

          open(2,file=systemfile,status='new',recl=nx)
          write(2,*)nx,ny,nz
          write(2,210)(((system(i,j,k),i=41,168),j=41,168),k=41,168)
210       format(<nx>a1)
          close (2)

          do j = 1,ny
             do i = 1,num(j)
             write(4,400)j,len(j,i),asp(j,i)
             end do
          end do
400       format(i3.3,1x,2g13.5)

          stop
          end

*********************************

          subroutine crell(system,is1,is2,is3,ic,jc,kc,a,b,
     &   iopt,n,nn,nin,iclip,imn,imx,jmn,jmx,kmn,kmx,len,asp,num)

*   Routine which creates a discretized oblate ellipsoid on a 3D grid. The
*   ellipsoid dimensions are A in the x and y directions and B in the z direction
*   The ellipse consists of all blocks having centres (x,y,z)
```

```
*  satisfying

*       (x-ic)**2/(a/2)**2 + (y-jc)**2/(a/2)**2 + (z-kc)**2/(b/2)**2 < 1

*  INPUTS:
*          SYSTEM  - a 3-dimensional char*1 array containing a binary
*                    ("black and white") image upon which the ellipsoid
*                    is to be superimposed (contains blanks outside
*                    ellipsoids, 'X's inside.)
*          IS1,IS2 - i*4 first two declared dimensions of SYSTEM
*          IS3     - i*4 3rd declared dimension of SYSTEM
*          IC,JC,KC - i*4 indices defining the center of ellipsoid on grid
*          A       - r*4 ellipsoid dimensions in x,y directions in grid
*                    units
*          B       - r*4 ellipsoid dimension in z direction
*          IOPT    - i*4 option switch. If = 0, no changes are made
*                    to array SYSTEM, if not= 0, changes are made
*          IMN,IMX - minimum and maximum i values in REGION OF INTEREST
*          JMN,JMX - minimum and max j values in region of interest
*          KMN,KMN- same for K

*  OUTPUTS:
*          SYSTEM  - updated array containing 'X's in the interior
*                    of the new ellipsoid (if IOPT not= 0)
*          N       - i*4 number of grid blocks inside ellipsoid and on grid
*          NN      - number of NEW grid blocks (not previously 'X') inside
*                    ellipsoid AND INSIDE THE LIMITS OF GRID
*          NIN     - number of pixels inside ROI
*          ICLIP   - i*4 flag. If ICLIP=0, ellipsoid is not clipped by
*                    edges of the r.o.i; if ICLIP not= 0 it IS CLIPPED
*          LEN     - 2d r*4 array giving lengths of slices of the
*                    ellipsoid parallel to x-z plane (ie. constant y).
*                    LEN(I,J) is the length of the jth ellipse resulting
*                    in the plane. Only ellipses lying completely
*                    within the region of interest are counted
*          ASP     - 2d r*4 array giving aspect ratios of slices of the
*                    ellipsoid parallel to x-z plane. like LEN. MUST
*                    BE ENTIRELY IN REGION OF INTEREST
*          NUM     - i*4 vector giving number of ellipses resulting in
*                    each y = constant plane

      character*1 system(is1,is2,is3)
      real*4 len(128,600),asp(128,600)
      integer*4 num(1)
      logical*1 iin,jin,kin
```

```
*  Fill in the ellipsoid by (constant y) "layers"

      IF (IOPT .EQ. 0) THEN
         jmax = jc + int(0.5*a)
         jmin = jc - int(0.5*a)
         if (jmax .gt. is2) then
            jmax = is2
         end if
         if (jmin .lt. 1) then
            jmin = 1
         end if
         n = 0
         nn = 0

         if (a .lt. 0.5) RETURN !no pixels in ellipse

         do j = jmin,jmax
            sqr = 1. - 4.*float(j-jc)*float(j-jc)/a/a
            if (sqr .gt. 0.) then
               xmax = sqrt(sqr)*0.5*a
            else
               xmax = 0.
            end if
            if (xmax .lt. 0.25) go to 15
            imax = ic + int(xmax)
            imin = ic - int(xmax)
            if (imax .gt. is1) then
               imax = is1
            end if
            if (imin .lt. 1) then
               imin = 1
            end if

            do i = imin,imax
               sqr1 = sqr - 4.*float(i-ic)*float(i-ic)/a/a
               if (sqr1 .gt. 0.) then
                  zmax = sqrt(sqr1)*0.5*b
               else
                  zmax = 0.
               end if
               if (zmax .lt. 0.25) go to 13
               kmax = kc+int(zmax)
               kmin = kc-int(zmax)
               if (kmax .gt. is3) then
                  kmax = is3
               end if
               if (kmin .lt. 1) then
```

```
                  kmin = 1
               end if
               do k = kmin,kmax
                  if (system(i,j,k) .ne. 'X')nn = nn + 1
                  n = n + 1
               end do
13             continue
            end do
15          continue
         end do
      ELSE
         icl ip = 0
            jmax = jc + int(0.5*a)
            jmin = jc - int(0.5*a)
            if (jmax .gt. is2) then
               jmax = is2
            end if
            if (jmin .lt. 1) then
               jmin = 1
            end if
         if (jmax.gt.jmx .or. jmin.lt.jmn)iclip = 1

         n = 0
         nn = 0
         nin = 0
         if (a .lt. 0.5) RETURN

         do j = jmin,jmax
            jin = (j.ge.jmn .and. j.le.jmx)
            sqr = 1. - 4.*float(j-jc)*float(j-jc)/a/a
            if (sqr .gt. 0.) then
               xmax = sqrt(sqr)*0.5*a
               h = 0.5*sqrt(sqr)*b ! 1/2 the height of ellipse
            else
               xmax = 0.
               h = 0.
            end if
            iclip1 = 0
            imax = ic + int(xmax)
            imin = ic - int(xmax)
            if (imax .gt. is1) then
               imax = is1
            end if
            if (imin .lt. 1) then
               imin = 1
            end if
            if (imax.gt.imx .or. imin.lt.imn) then
```

```
                iclip = 1
                iclip1 = 1
            end if
            if (xmax .lt. 0.25) go to 19
            kh = 0
            do i = imin,imax
                iin = (i.ge.imn .and. i.le.imx)
            sqr1 = sqr - 4.*float(i-ic)*float(i-ic)/a/a
            if (sqrl .gt. 0.) then
                zmax = sqrt(sqrl)*0.5*b
            else
                zmax = 0.
            end if
            if (zmax .lt. 0.25) go to 17
            kmax = kc+int(zmax)
            if (kmax .gt. is3) then
                kmax = is3
            end if
            kmin = kc-int(zmax)
            if (kmin .lt. 1) then
                kmin = 1
            end if
            if (kmin.lt.kmn .or. kmax.gt.kmx) then
                iclip = 1
                iclipl = 1
            end if
            if (kmax-kmin .gt. kh) kh = kmax - kmin
            do k = kmin,kmax
                kin = (k.ge.kmn .and. k.le.kmx)
                if (system(i,j,k) .ne. 'X')then
                    nn = nn + 1
                    if (iin .and. jin .and. kin)nin = nin + 1
                end if
                n = n + 1
                system(i,j,k) = 'X'
            end do
17          continue
        end do
        if (iclipl.eq.0 .and. iclip.eq.0)then !ellipsoid
                    !complete in this j-plane
            jj = j - jmn + 1
            num(jj) = num(jj) + 1
            len(jj,num(jj)) = 1.+float(imax-imin)
            asp(jj,num(jj)) = (1.+ float(kh))/
     &          len(jj,num(jj))
        end if
19      continue
```

```
            end do

         END IF
         return
         end

*********************************

         subroutine indexx(n,arr,indx)

*  Routine that indexes an input array ARR such that ARR(indx(j)) is
*  in ascending order for j = 1,2,...,n. Input quantities N and ARR are
*  not changed.
*  This routine is taken from W.H. Press et al, "Numerical Recipes",
*  Cambridge Press, 1986, p. 233.

         dimension arr(n),indx(n)
         do 11 j = 1,n
            indx(j) = j
11       continue
         l = n/2 + 1
         ir = n
10       continue
         if (l.gt.1) then
            l = l - 1
            indxt = indx(l)
            q = arr(indxt)
         else
            indxt = indx(ir)
            q = arr(indxt)
            indx(ir) = indx(1)
            ir = ir - 1
            if (ir.eq.1) then
               indx(1) = indxt
               return
            end if
         end if
         i = l
         j = l + l
20       if (j.le.ir) then
            if (j.lt.ir) then
               if(arr(indx(j)).lt.arr(indx(j+1)))j = j + 1
            end if
            if (q.lt.arr(indx(j)))then
               indx(i) = indx(j)
               i = j
               j = j + j
```

```
            else
               j = ir+1
            end if
         go to 20
         end if
         indx(i) = indxt
         go to 10
         end

*********************************

         function ranlen(r)

*  Subprogram which produces a "length" distributed according to the
*  cumulative distribution given in array C(9), given an input random
*  number from a uniform distribution on [0,1].

*  INPUT:

*        R      - r*4 uniform random number on [0,1]

*  NOTES:
*  The cumulative distribution is for log10(length) of all clasts in
*  4 real intervals from well B. This version is based
*  on a 3d size distribution of lognormal form

*        0.171*exp(-8.01*(log10(L)+0.347)**2)

*  that has been truncated and re-normalized between

*        -0.4 < log10(L) < 0.4

*  D. Cuthiell. 1990

         real*4 r,ranlen
         real*4 loglen(9)/-0.4,-0.3,-0.2,-0.1,
     &                    0.,0.1,0.2,0.3,0.4/
         real*4 c(9)/0.,0.272,0.525,0.725,0.861,
     &              0.9391,0.9778,0.9941,1./

         i = 1
         do while (r .gt. c(i))
            i = i + 1
         end do

         fract = (r - c(i-1))/(c(i) - c(i-1))
         ranlen = fract*loglen(i) + (1.-fract)*loglen(i-1)
```

```
        ranlen = 10.**ranlen

        return
        end

*********************************

        function ranasp(r)

*  Subprogram which produces an "aspect ratio" distributed according to the
*  cumulative distribution given in array C(6), given an input random
*  number from a uniform distribution on [0,1].

*  INPUT:

*       R     - r*4 uniform random number on [0,1]

*  NOTES:
*  The cumulative distribution is for aspect ratio of all clasts in
*  4 real clast intervals from well B.

*  D. Cuthiell. 1990.

        real*4 r,ranasp
        real*4 aspect(10)/0.1,0.2,0.3,0.4,0.5,0.6,0.7,0.8,0.9,1./
        real*4 c(10)/0.,0.0056,0.0777,0.2510,0.4813,0.6505,
     &              0.8003,0.9043,0.9709,1./

        i = 1
        do while (r .gt. c(i))
        i = i + 1
        end do

        fract = (r - c(i-1))/(c(i) - c(i-1))
        ranasp = fract*aspect(i) + (1.-fract)*aspect(i-1)

        return
        end
```

APPENDIX C

Finite Difference Flow Simulation Method

The numerical solution of the flow equation (16) has been carried out using a method known as the point successive over-relaxation (SOR) method. The basic steps of the method are described in this appendix (see Aziz and Settari, 1979 for further details).

Equation (16) incorporates both fluid conservation and Darcy's law. To obtain a discrete version of this equation suitable for numerical solution, it is simplest to apply these physical principles directly on a finite difference grid. The following argument is given in two dimensions but is readily extended to three; the Fortran program FL03D included in this appendix performs the 3D calculation.

Figure C1 illustrates a portion of a two-dimensional grid made up of square grid blocks and assumed to fill the flow region of interest. The method of discretization used in this study was "point-centred" rather than the "block-centred" formulation used in most reservoir simulators (Aziz and Settari, 1979). In the point-centred method, pressure values are solved for at the nodes, or intersections, of the grid. For the binary clast simulations, each interior block (e.g., blocks 1, 2, 3 and 4 in Figure C1) is defined uniquely as either "sand" or "shale" and has the corresponding permeability.

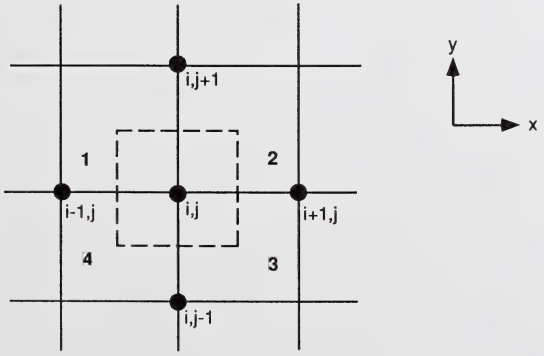

Figure C1. *Portion of a 2D finite difference grid and the control volume (dashed box) used to derive the equation for pressure at node (i,j).*

To develop an equation for the pressure at node (i,j), one considers the flow of fluid through the edges of the control volume shown as a dashed box in Figure C1. At steady state, the total flow leaving this volume must equal zero. Consider the fluid leaving the top side of the control volume, located midway between nodes (i,j) and $(i,j+1)$. The flow rate is given by Darcy's law, equation (14). If the grid blocks 1 and 2 have vertical permeability values k_{1y} and k_{2y}, the equivalent permeability for flow through this edge is the arithmetic mean of these two values, since the flow is in parallel. In the lowest order finite difference representation of the differential equation, the derivative of pressure is replaced by the difference expression:

$$\frac{\partial P}{\partial y} \rightarrow \frac{\left(P_{i,j+1} - P_{i,j}\right)}{\Delta}$$

where Δ is the grid spacing. Thus, the flow Q_{j+} through the face is given by:

$$\text{(C1)}\quad Q_{j+} = -C_{j+}\left(P_{i,j+1} - P_{i,j}\right)$$

where:

$$C_{j+} = \frac{1}{2}\left(k_{1y} + k_{2y}\right)\left(\frac{T\Delta}{\mu}\right)$$

and μ is the viscosity of the fluid and T is the thickness of the control volume. The total outward flow through all four sides of the control volume must equal zero, and thus:

$$\text{(C2)}\quad C_{j+}\left(P_{i,j+1} - P_{i,j}\right) + C_{j-}\left(P_{i,j-1} - P_{i,j}\right) + C_{i+}\left(P_{i+1,j} - P_{i,j}\right) + C_{i-}\left(P_{i-1,j} - P_{i,j}\right) = 0$$

where the coefficients C_{j-}, C_{j+} and C_{i-} are defined

similarly to C_{j+}. Equation (C2) can be re-written in the form:

$$(C3)\ P_{i,j} = a_{i,j} P_{i,j+1} + b_{i,j} P_{i,j-1} + c_{i,j} P_{i+1,j} + d_{i,j} P_{i-1,j}$$

where:

$$a_{i,j} = \frac{C_{j+}}{\left(C_{j+} + C_{j-} + C_{i+} + C_{i-}\right)}$$

and the other coefficients on the right hand side of (C3) are defined similarly. Equation (C3) may be solved for pressure iteratively at each node of the grid. If $P_{i,j}^{(m)}$ denotes the value of pressure $P_{i,j}$ at iteration step m, then a new value $P_{i,j}^{(m+1)*}$ can be computed by substituting the values of pressure at step m on the right side of (C3):

$$(C4)\ P_{i,j}^{(m+1)*} = a_{i,j} P_{i,j+1}^{(m)} + b_{i,j} P_{i,j-1}^{(m)} + c_{i,j} P_{i+1,j}^{(m)} + d_{i,j} P_{i-1,j}^{(m)}$$

This form of iteration defines the classical Gauss-Seidel method. The SOR method used here, which is much more efficient, computes the updated value of $P_{i,j}^{(m+1)}$ as a weighted average of $P_{i,j}^{(m+1)*}$ defined in (C4) and the old value $P_{i,j}^{(m)}$:

$$(C5)\ P_{i,j}^{(m+1)} = \omega P_{i,j}^{(m+1)*} + (1-\omega) P_{i,j}^{(m)}$$

It is important to select an appropriate weighting factor, or "relaxation parameter," ω, in equation (C5) and many methods for doing so have been proposed in the literature (e.g., see Young, 1971). The method used here is to select a starting value for ω at the outset of the simulation (usually the starting value is chosen to be between 1.5 and 2; it must not be greater than 2), then update it by the following procedure (Aziz and Settari, 1979) as the simulation progresses. At a particular iteration step m, define:

$$\delta_m \equiv \underset{i,j}{Max} \left| P_{i,j}^{(m+1)} - P_{i,j}^{(m)} \right|$$

Then compute:

$$\Theta = \frac{\delta_{m+1}}{\delta_m}$$

and:

$$\rho = \frac{\Theta + \omega - 1}{\omega \Theta^{1/2}}$$

where ω is the current relaxation parameter. An updated relaxation parameter, ω*, is obtained using the equation

$$\omega^* + \frac{2}{\left[1 + \left(1 - \rho^2\right)^{1/2}\right]}$$

The program FL03D (source code given below) implements the SOR algorithm in 3D. The iterative calculations of pressure at each node, and the updates of ω occupy relatively little of the code. Much of the program has been designed to minimize memory requirements. Thus, rather than storing the real coefficients ($a_{i,j}$, etc.) for the iterative calculation for each node, a 2 byte code is assigned to each node telling the type (sand or shale) of each of the surrounding 8 grid blocks. The coefficients required for the iteration are then recalculated at each iteration step. This sacrifices CPU time for the sake of reduced memory and may not be necessary if larger memory resources are available or the desired grid size is not as large. Boundary conditions are handled in the program by fixing the pressures at the inflow and outflow ends of the grid and using a layer of zero permeability blocks on the sides of the flow region to enforce the no-flow boundary condition. The convergence of the simulations is tested by computing the total flow through grid planes at the inlet end, the middle and the outlet end of the grid. When these three flows agree to some pre-defined tolerance, the calculation is terminated and the average of the three flow values is used to compute the effective permeability.

PROGRAM LISTING

```
** FL03D.FOR **

*  A 3D version of the SOR flow simulation program. The grid blocks can have
*  only 3 possible permeabilities: zero, or permeability of shale, or
*  permeability of sand (zero is for boundary blocks).

*  Much of the coding is done to be able to find nearest neighbor couplings at
*  the time of computation of the SOR scheme. This is to save memory.
*  Each block is coded as 1, 2 or 3 corresponding to the possible permeabilities.
*  The environment of a grid point is described by a "code" consisting of
*  8 digits, each being 1,2 or 3, and corresponding to the code of one of the
*  8 neighbor blocks of the grid point in question. The 8 blocks surrounding
*  the grid point are numbered clockwise from the +x+y quadrant in the plane
*  of blocks below the grid point (ie in the -z direction) then similarly in
*  the plane of blocks above the grid point.
*  The sequence is like an 8-digit trinary number
*  except the possible digits are 1,2,3 rather than 0,1,2. The correspondence
*  with 8-digit numbers can be used to put each of the 3**8 environments in
*  a sequence from {11111111} to {33333333}.

*  This version of FL03D is single precision which works alright in practice.
*  Flow is assumed to be in the z direction. To model flow in one of the
*  other two directions the image file must be re-written to convert the desired
*  direction into the k direction.

*  The program calls subroutines:

*        UPDATE - to update the pressures (array u) on grid using SOR algorithm.
*        PERM3D - to calculate flow through a (x-y) plane of grid blocks.

*  For input, the program requires interactive responses and also a file
*  containing a description of the flow "system". Typically this is created
*  using program CLASTS.FOR and it must contain blanks to represent "sand"
*  and 'X's to represent heterogeneity. The program may optionally read
*  a pressure field from a save file FL03D.SAV created in an earlier run
*  of the program. An output file FL03D.OUT is created which gives results
*  at pre-selected numbers of iterations; a summary file FLOW3D.SUM gives a
*  final short summary of the results on completion; a save file FL03D.SAV
*  is created so that another simulation can run starting from the endpoint
*  of the present one, and a log file FL03D.LOG records number of iterations
*  and 3 estimates of permeability, based on the top, middle and bottom of
*  grid and can be read as the simulation is in progress.

*  Written by D. Cuthiell, Alberta Research Council, 1990
```

```
      character*60 sumfile/'flow3d.sum'/
*     *U is the array containing pressures at nodes
      dimension u(131,131,131)
      integer*2 ineigh(131,131,131)
      character*1 slice(131,131)
      integer*2 layer1(131,131),layer2(131,131)
      dimension permx(3),permy(3),permz(3)
      dimension permx1(6561),permx2(6561),permy1(6561),permy2(6561),
     1      permz1(6561),permz2(6561)
      dimension perme1(131,131),perme2(131,131),perme3(131,131)
      character*50 savefile,imagefile,resp*1
      character*600 buf,buf1,buf2,buf3
      logical*1 save,vertical,norm
      parameter (maxx=131,maxy=131,maxz=131)

*  Choose some parameters describing the heterogeneity
*  (Note: the grid will always be chosen so flow is in z direction)

      write(6,600)
600   format(' Matrix perms in x, y and z directions, resp.? ',$)
      read(5,*)permx(2),permy(2),permz(2)
      write(6,605)
605   format(' Heterogeneity perms in x,y and z directions? ',$)
      read(5,*)permx(3),permy(3),permz(3)

*  Control decisions

      write(6,*)' Initial choice of iteration parameter omega?'
      read(5,*)omega
      write(6,*)' Convergence parameter epsilon?'
      read(5,*)eps
      write(6,*)' Interval at which to update omega (no. of iters)?'
      read(5,*)nupdate
      write(6,*)' Choose no. of iterations to do'
      read(5,*)niter
      iter0 = 0
      write(6,*)' Is there a save file (Y/N)?'
      read(5,500)resp
      save = (resp .eq. 'y' .or. resp.eq.'Y')
      if (save) then
         write(6,*)' Name of save file?'
         read(5,500)savefile
         open(11,file=savefile,status='old',form='unformatted')
         read(11)iter0,omega,ixmax,iymax,izmax
         read(11)(((u(i,j,k),i=1,ixmax),j=1,iymax),k=1,izmax)
```

```
            close (11)
         end if
         write(6,*)' Printout interval (in iterations)? '
         read(5,*)nprint

*  Note: a given node has eight neighboring blocks, each of which can
*  have 3 different (vertical and horizontal) permeabilities. Therefore
*  the total number of configurations is 3**8 = 6561. The arrays
*  permxl,permx2,permyl,permy2,permzl,permz2 give the permeabilities in
*  the -x,+x,-y,+y,-z,+z directions respectively for each possible configur-
*  ation of neighbors.

         icode = 1
         do i1 = 1,3
            do i2=1,3
               do i3 = 1,3
                  do i4 = 1,3
                     do i5 = 1,3
                        do i6 = 1,3
                           do i7 = 1,3
                              do i8 = 1,3
                                 permx1(icode)  =  0.25*(permx(i3)+permx(i4)
     1                                             +permx(i7)+permx(i8))
                                 permx2(icode)  =  0.25*(permx(i1)+permx(i2)
     1                                             +permx(i5)+permx(i6))
                                 permyl(icode)  =  0.25*(permy(i2)+permy(i3)
     1                                             +permy(i6)+permy(i7))
                                 permy2(icode)  =  0.25*(permy(i1)+permy(i4)
     1                                             +permy(i5)+permy(i8))
                                 permz1(icode)  =  0.25*(permz(i1)+permz(i2)
     1                                             +permz(i3)+permz(i4))
                                 permz2(icode)  =  0.25*(permz(i5)+permz(i6)
     1                                             +permz(i7)+permz(i8))
                                 icode =  icode + 1
                              end do
                           end do
                        end do
                     end do
                  end do
               end do
            end do
         end do

*  Collect raster data describing the binary system. Typically this
*  "system image" is in a file created by the program CLASTS.FOR or
*  variations thereof. Each grid block in the image is either a blank
*  character ' ' if it is sand, or the character 'X' if it is shale
```

```
*  (heterogeneity).

         write(6,610)
610      format(/' File containing system image? ',$)
         read(5,500)imagefile
         inquire(file=imagefile,recl=irecl)
         open(1,file=imagefile,status='old',recl=irecl)
500      format(a)
         read(1,*)nx,ny,nz
         nk = nz
         ni = nx
         nj = ny

*  Construct "couplings" based on the image. Grid coordinates that get
*  updated range from i=2 to i=ni+2; from j=2 to j=nj+2; and from
*  k=2 to k=nk. Note that the layers of grid points having i=1,i=ni+3,
*  j=1 and j=nj+3 are buffer points outside the actual flow region and
*  represent no-flow boundaries on the sides of the flow region. Note that
*  all blocks outside the active flow region are coded as 1 (meaning
*  zero permeability).

         imin = 2
         imax = ni + 2
         jmin = 2
         jmax = nj + 2
         kmin = 2
         kmax = nk
         ixmax = imax+1
         iymax = jmax+1
         izmax = kmax + 1

         read(1,100)((slice(i,j),i=1,ni),j=1,nj)
100      format(<ni>a1)
         do j = 1,nj
            do i = 1,ni
               layer2(i,j) = 2
               if (slice(i,j) .eq. 'X')layer2(i,j) = 3
            end do
         end do
         do k = kmin,kmax
            do j = 1,nj
               do i = 1,ni
                  layer1(i,j) = layer2(i,j)
               end do
            end do
            read(1,100)((slice(i,j),i=1,ni),j=1,nj)
            do j = 1,nj
```

```
            do i = 1,ni
               layer2(i,j) = 2
               if (slice(i,j) .eq. 'X')layer2(i,j) = 3
            end do
         end do

*        *  i = imin boundary
         i = imin

         j = jmin
         ineigh(i,j,k) = 2187*1layer1(i-1,j-1)
     4                   +27*1layer2(i-1,j-1)
     8                      -2213
         do j = jmin+1,jmax-1
            ineigh(i,j,k) = 2187*1layer1(i-1,j-1)
     1                   +729*1layer1(i-1,j-2)
     4                   +27*1layer2(i-1,j-1)
     5                   +9*layer2(i-1,j-2)
     8                        -2951
         end do
         j = jmax
         ineigh(i,j,k) = 729*1layer1(i-1,j-2)
     5                   +9*layer2(i-1,j-2)
     8                      -737
*        *  i = imax boundary
         i = imax

         j = jmin
            ineigh(i,j,k) = 81*1layer1( i-2, j-1)
     7                   +1*layer2(i-2,j-1)
     8                      -81
         do j = jmin+1,jmax-1
            ineigh(i,j,k) = 243*1layer1(i-2,j-2)
     3                           +81*1layer1(i-2,j-1)
     6                   +3*1layer2(i-2,j-2)
     7                   +1*layer2(i-2,j-1)
     8                      -327
         end do
         j = jmax
         ineigh(i,j,k) =  243*layer1(i-2,j-2)
     6                   +3*1layer2(i-2,j-2)
     8                      -245
*        *j=jmin boundary
         j = jmin

         do i = imin+1,imax-1
            ineigh(i,j,k) = 2187*1layer1(i-1,j-1)
```

```
     3                    +81*1layer1(i-2,j-1)
     4                    +27*layer2(i-1,j-1)
     7                    +1*layer2(i-2,j-1)
     8                       -2295
          end do

*         *j=jmax boundary
          j = jmax

          do i = imin+1,imax-1
             ineigh(i,j,k) = 729*1layer1(i-1,j-2)
     2                    +243*layer1(i-2,j-2)
     5                    +9*layer2(i-1,j-2)
     6                    +3*layer2(i-2,j-2)
     8                       -983
          end do

*         *Interior of the grid
          do j = jmin+1,jmax-1
             do i = imin+1,imax-1
                ineigh(i,j,k) = 2187*1layer1(i-1,j-1)
     1                    +729*1layer1(i-1,j-2)
     2                    +243*layer1(i-2,j-2)
     3                    +81*1layer1(i-2,j-1)
     4                    +27~1layer2(i-1,j-1)
     5                    +9*layer2(i-1,j-2)
     6                    +3*layer2(i-2,j-2)
     7                    +1*layer2(i-2,j-1)
     8                       -3279
             end do
          end do

       end do

       CLOSE (1)

*  Compute permeabilities for 3 layers of nodes at bottom, middle
*  and top of the grid. Permeability is downward from the chosen
*  grid point row

       kmid = (kmin + kmax)/2
       do i = imin,imax
          do j = jmin,jmax
             perme1(i,j) = permz1(ineigh(i,j,kmin))
             perme2(i,j) = permz1(ineigh(i,j,kmid))
             perme3(i,j) = permz1(ineigh(i,j,kmax))
```

```
            end do
         end do

*  If there is no save file then choose a
*  starting distribution for the potential u(i,j,k)
*  by assuming a linear profile going from a value u = 1 at k = 1
*  to u = kmax+1 at k = kmax=1. In the absence of heterogeneity,
*  this is the final solution.

         if (.not. save) then
            do k = 1,kmax+1
               do i = 1,imax+1
                  do j = 1,jmax+1
                     u(i,j,k) = float(k)
                  end do
               end do
            end do
         end if

*  Open files and write headers to them

         open(2,file='flo3d.out',status='new',
     1        carriagecontrol='list')
         open(4,file=sumfile,status='new',carriagecontrol='list')
         if (.not. save)
     1   open(3,file='flo3d.sav',status='new',
     1        form='unformatted')
         write(2,2002)
         write(4,2002)
2002     format(' Flow in the z direction')
         write(2,2003)imagefile
         write(4,2003)imagefile
2003     format(' Image from file: ',a)
         write(2,2005)nx,ny,nz
         write(4,2005)nx.ny,nz
2005     format(' Image size: ',i4,'(x) by ',i4,'(y) by ',i4,'(z)')

         write(2,2010)permx(2),permy(2),permz(2)
         write(2,2020)permx(3),permy(3),permz(3)
2010     format(  ' Matrix permeabilities:'/
     1           '      kx: ',g12.5,/
     2           '      ky: ',g12.5,/
     3           '      kz: ',g12.5)
2020     format(  ' Heterogeneity permeabilities:'/
     1           '      kx: ',g12.5,/
     2           '      ky: ',g12.5,/
     3           '      kz: ',g12.5)
```

```
      write(2,2030)omega
2030  format(' Relaxation parameter (omega): ',g15.7,/)

      write(2,2040)eps
      write(4,2040)eps
2040  format(  ' Stopping parameter, epsilon: ',g15.7,/)
      close (4)
      write(2,200)
200   format(  ' Iters.    Perm1    Perm2    Perm3',
     1         '      Perm    Omega    Theta')
      write(6,200)
210   format(1x,i5,1x,4g12.5,2g13.6)

***PERFORM THE ITERATIONS ***
*  (note count only current iterations)
      close (2)
      open(8,file='flo3d.log',status='new')
      close(8)
      do iter = 1,niter
         if (mod(iter+1,nupdate) .eq. 0) then
            norm = .true.
            call update3d(u,maxx,ineigh,maxx,imin,imax,jmin,
     1           jmax,kmin,kmax,permx1,permx2,permy1,permy2,permz1,
     2           permz2,omega,norm,delta_old)
         else if (mod(iter,nupdate) .eq. 0) then
            norm = .true.
            call update3d(u,maxx,ineigh,maxx,imin,imax,jmin,
     1           jmax,kmin,kmax,permx1,permx2,permy1,permy2,permz1,
     2           permz2,omega,norm,delta_new)
            theta = delta_new/delta_old
            rho = (theta + omega - 1.)/(omega*sqrt(theta))
            if (rho .lt. 1.) then
               omegal = 2./(1. + sqrt(1.-rho*rho))
               if (omegal .lt. 2. .and. omegal .gt. 1.)
     1                          omega=omegal
            end if
         else
            norm = .false.
            call update3d(u,maxx,ineigh,maxx,imin,imax,jmin,
     1           jmax,kmin,kmax,permx1,permx2,permy1,permy2,permz1,
     2           permz2,omega,norm,delta_new)
         end if
         if (mod(iter,nprint) .eq. 0) then
*  Note that with the choice of pressure field, the flows calculated by
*  FLOAVE (perm1, perm2, perm3 below) are actually equivalent to dimensionless
*  permeabilities (relative to sand).
            call floave(u,maxx,kmin,imin,imax,
```

```
     1                    jmin,jmax,perme1,maxx,perm1)
                       call floave(u,maxx,kmid,imin,imax,
     1                    jmin,jmax,perme2,maxx,perm2)
                       call floave(u,maxx,kmax,imin,imax,
     1                    jmin,jmax,perme3,maxx,perm3)
                       perm = 0.3333333333*(perm1+perm2+perm3)
                       open(2,file='flo3d.out',status='old',
     1                    access='append')
                       write(2,210)iter+iter0,perm1,perm2,perm3,perm,omega,
     1                          theta
                       close (2)
                       write(6,210)iter+iter0,perm1,perm2,perm3,perm,omega,
     1                          theta
                       open(8,file='flo3d.log',status='old')
                       close (8,dispose='delete')
                       open(8,file='flo3d.log',status='new')
                       write(8,800)iter,perm1,perm2,perm3,omega
800                 format(  ' No. of iterations = ',i6,/
     1                        ' Permeability estimates ',3g15.6,/
     2                        ' Omega = ',g14.6)
                       close (8)
                       if (perm2.ne.0.)then
                          dperm1 = abs((perm1-perm2)/perm2)
                          dperm3 = abs((perm3-perm2)/perm2)
                          if (dperm1.lt.eps .and. dperm3.1t.eps)then
                             write(6,*)'met stopping criterion'
                             niter = iter
                             GO TO 77
                          end if
                       end if
                 end if
              end do

*  Save the final potential

77            conv = 0.5*(dperm1 +dperm3) !convergence measure
              write(3)iter0+niter,omega,ixmax,iymax,izmax
              write(3)(((u(i,j,k),i=1,ixmax),j=1,iymax),k=1,izmax)
              open(4,file=sumfile,status='old',access='append')
              write(4,460)perm,conv,iter0+niter
460           format(/ ' Effective permeability = ',g15.7/
     1                 ' Convergence measure = ',g15.7,/
     2                 ' Total iteration steps = ',i6)
              close (4)

              stop
              end
```

```
*********************************

      subroutine update3d(u,iu,ineigh,in,imin,imax,jmin,
     1          jmax,kmin,kmax,permx1,permx2,permy1,permy2,permz1,
     2          permz2,omega,norm,delta)

*  This subroutine updates the 3D potential field, u, by one SOR iteration
*  It is intended for a case of binary heterogeneity in which either
*  x,y or z permeability can have only two possible values (0 for boundary
*  blocks). In a practical situation these are "matrix" permeability, or
*  "heterogeneity" permeablility. However, they are represented simply by
*  indices 2 or 3, resp. (1 for boundary blocks).

**********************

** NOTE: THIS VERSION UPDATES THE GRID FROM MAXIMUM TO MINIMUM K INDEX
** OTHER POSSIBILITIES CAN BE TRIED AND MAY BE MORE EFFICIENT.
**********************

*  D. Cuthiell. 1990.

*  INPUTS:
*       U       - real*4 array containing the potential field
*       IU      - I*4 row dimension of U
*       INEIGH  - I*2 array coding the "environment" of each grid point
*                 in the potential field as follows: each of the neighbors
*                 of the grid point is labelled with a value 1, 2 or 3
*                 corresponding to 0 permeability, "matrix" or "heterogeneity"
*                 respectively. The coding used in INEIGH is

*                 INEIGH(I,J) = CODE(I-,J+,K+) + 3*CODE(I-,J-,K+)
*                               +9*CODE(I+,J-,K+) +27*CODE(I+,J+,K+)
*                               +81CODE(I-,J+,K-) +243*CODE(I-,J-,K-)
*                               +729*CODE(I+,J-,K-) +2187*CODE(I+,J+,K+)
*                               - 3279

*                               where (CODE(I-,J+,K+) is the value (1,2, or 3)
*                               for the neighbor in the -ve I, +ve J
*                               and +ve K direction
*                               from the grid point and similarly for the other
*                               terms in the right hand side of the equation.
*                               INEIGH has values from 1 to 6561 for the
*                               various possible values on the rhs of equation.

*       IN      - I*4 row dimension of array INEIGH
*       IMIN    - I*4 minimum I index of U to be updated
```

```
*       IMAX    -  I*4 maximum I index of U to be updated
*       JMIN    -  I*4 minimum J index of U to be updated
*       JMAX    -  I*4 maximum J index of U to be updated
*       KMIN    -  I*4 minimum K index of U to be updated
*       KMAX    -  I*4 maximum K index of U to be updated
*       PERMX1  -  R*4 array giving permeability in the -VE x direction,
*                  for each of the 6561 possible environments
*                  of a grid point (corresponding to 3 possible permeabilities
*                  for each of 8 neighboring blocks
*       PERMX2  -  R*4 array like PERMX1 but for the +ve x direction
*       PERMY1  -  R*4 array like PERMX1 but for the -ve y direction
*       PERMY2  -  R*4 array like PERMX1 but for the +ve y direction
*       PERM71  -  R*4 array like PERMX1 but for the -ve z direction
*       PERMZ2  -  R*4 array like PERMX1 but for the +ve z direction
*       OMEGA   -  R*4 relaxation parameter used in SOR method
*       NORM    -  LOGICAL*1 variable. If =true, routine calculates a value
*                  for DELTA (see "OUTPUTS" below)

*  OUTPUTS:
*       U       -  R*4 updated potential array
*       DELTA   -  R*4 metric which measures the amount of change induced
*                  in the potential by this iteration, defined as
*
*                     DELTA = max(abs(u(i,j,k)-uold(i,j,k))) for all i,j,k within
*                                 range of update

*                     where u is updated potential, uold is initial potential
*                     (as input to the subroutine)
*                     DELTA is only calculated if NORM = .TRUE.

      real*4 u(131,131,131),permx1(6561),permx2(6561),permy1(6561),
     1           permy2(6561),permz1(6561),permz2(6561),omega,delta
      integer*4 iu,in,imin,imax,jmin,jmax
      integer*2 ineigh(131,131,131)
      logical*1 norm

      omega1 = 1. - omega
      IF (.NOT. NORM) THEN
         do k = kmax,kmin,-1
            do j = jmin,jmax
               do i = imin,imax
                  icode = ineigh(i,j,k)
                  a = permx1(icode)
                  b = permx2(icode)
                  c = permy1(icode)
                  d = permy2(icode)
                  e = permz1(icode)
```

```
                  f = permz2(icode)
                  g = a + b + c + d + e + f
                  if (g .ne. 0.) then
                     ustar = (a*u(i-1,j,k) + b*u(i+1,j,k)
     1                     + c*u(i,j-1,k) + d*u(i,j+1,k)
     2                     + e*u(i,j,k-1) + f*u(i,j,k+1))/g
                     u(i,j,k) = omegal*u(i,j,k) + omega*ustar
                  end if
               end do
            end do
         end do
      ELSE
         delta = -1.d38
         do k = kmax,kmin,-1
            do j = jmin,jmax
               do i = imin,imax
                  icode = ineigh(i,j,k)
                  a = permx1(icode)
                  b = permx2(icode)
                  c = permy1(icode)
                  d = permy2(icode)
                  e = permz1(icode)
                  f = permz2(icode)
                  g = a + b + c + d + e + f
                  if (g .ne. 0.) then
                     uold = u(i,j.k)
                     ustar = (a*u(i-1,j,k) + b*u(i+1,j,k)
     1                     + c*u(i,j-1,k) + d*u(i,j+1,k)
     2                     + e*u(i,j,k-1) + f*u(i,j,k+1))/g
                     u(i,j,k) = (1.-omega)*uold + omega*ustar
                     delta = max(delta,abs(u(i,j,k)-uold))
                  end if
               end do
            end do
         end do
      END IF
      return
      end

*********************************

      subroutine floave(u,iu,k,imin,imax,jmin,jmax,perm,ip,
     1                  flow)

*  Routine which computes an average "flow" across a particular xy plane
*  fixed k) based on a 3D potential. Basically just uses Darcy's law for
*  each grid block in the layer.
```

```
*  D. Cuthiell. 1990.

*  INPUTS:
*        U       -   R*4 array representing the potential on a grid.
*        IU      -   I*4 row dimension of U.
*        K       -   fixed value of k for which the average is to be taken
*        IMIN    -   I*4 minimum i index over which to average
*        IMAX    -   I*4 maximum i index over which to average
*        JMIN    -   I*4 minimum j index over which to average
*        JMAX    -   I*4 maximum j index over which to average
*        PERM    -   R*4 array giving weights for the average. That is,
*                    for a row index i and column index j, the weighting
*                    is PERM(I,J). See code.
*        IP      -   I*4 row dimension of PERM

*  OUTPUT:
*        FLOW    -   R*4 value of average flow

*  NOTE: THE FLOW IS COMPUTED IN THE -VE K DIRECTION.

      real*4 u(131,131,131),perm(131,131),flow
      integer*4 iu,j,imin.imax,jmin,jmax

      sum = 0.d0
      do i = imin,imax
         do j = jmin,jmax
            sum = sum + ((u(i,j,k)-u(i,j,k-1))*perm(i,j))
         end do
      end do
      flow = sum/float(imax-imin)/float(jmax-jmin)
      return
      end
```

N.L.C./B.N.C.
3 3286 50150 4472

PRINTED IN CANADA